The Development of Unique Focal Planes for High-Resolution Suborbital and Ground-Based Exploration

by

Alexander Duke Miller

A Dissertation Presented in Partial Fulfillment
of the Requirements for the Degree
Doctor of Philosophy

Approved April 2019 by the
Graduate Supervisory Committee:

Paul Scowen, Chair
Chris Groppi
Daniel Jacobs
Nathaniel Butler
Philip Mauskopf

ARIZONA STATE UNIVERSITY

May 2019

ABSTRACT

The development of new Ultra-Violet/Visible/IR range (UV/Vis/IR) astronomical instrumentation that use novel approaches for imaging and increase the accessibility of observing time for more research groups is essential for rapid innovation within the community. Unique focal planes that are rapid-prototyped, low cost, and provide high resolution are key.

In this dissertation the emergent designs of three unique focal planes are discussed. These focal planes were each designed for a different astronomical platform: suborbital balloon, suborbital rocket, and ground-based observatory. The balloon-based payload is a hexapod-actuated focal plane that uses tip-tilt motion to increase angular resolution through the removal of jitter – known as the HExapod Resolution-Enhancement SYstem (HERESY), the suborbital rocket imaging payload is a Jet Propulsion Laboratory (JPL) delta-doped charge-coupled device (CCD) packaged to survive the rigors of launch and image far-ultra-violet (FUV) spectra, and the ground-based observatory payload is a star centroid tracking modification to the balloon version of HERESY for the tip-tilt correction of atmospheric turbulence.

The design, construction, verification, and validation of each focal plane payload is discussed in detail. For HERESY's balloon implementation, pointing error data from the Stratospheric Terahertz Observatory (STO) Antarctic balloon mission was used to form an experimental lab test setup to demonstrate the hexapod can eliminate jitter in flight-like conditions. For the suborbital rocket focal plane, a harsh set of unit-level tests to ensure the payload could survive launch and space conditions, as well as the characterization and optimization of the JPL detector, are detailed. Finally, a modification of co-mounting a fast-read detector to the HERESY focal plane, for use on ground-based observatories, intended to reduce atmospherically induced tip-tilt error through the centroid tracking of bright natural guidestars, is described.

DEDICATION

For my mom, dad, and sisters – without your love, support, and encouragement to pursue my dreams I would have given up on space exploration long ago. This paper is dedicated to you.

Mom, you are a loving and kind force in my life. Thank you for all your faith in me and having such confidence in my decisions. Taking me to visit the Smithsonian's Air & Space Museum when I was little is responsible for my lifetime of space obsession (thank you!).

Dad, I have always been in awe of your talent, work-ethic, and all your accomplishments. You taught me to always 'do what I love, and it will never feel like work.' I hope my accomplishments will make you as proud of me as I am of you.

ACKNOWLEDGEMENTS

Every Padawan needs a Jedi Master to learn from, and through my career that has been Paul Scowen, a truly wise and seasoned Obi-Wan Kenobi who has always kept me from straying to the dark side and taught me to 'trust my feelings' (as long as there is literature and data to back it up). To Paul I owe great gratitude for taking so much of his time and effort to guide me and hold me to a high standard. I truly appreciate all your patience, kindness, and your lessons on the art of systems engineering through the years, and I've always known you've had my back through thick-and-thin, which is all a grad student could ever ask for.

A HUGE thanks to Robert Leach of Astronomical Research Cameras. He is my Yoda. A true master of CCD/CMOS readout electronics technology and an expert in detector characterization. Not only did he promptly answer dozens of challenging questions I've had over the years via email, but he allowed me to pack up a ton of lab equipment, drive to San Diego, and work alongside him in his company's lab for several days to help me optimize my equipment. A truly great person who provided me with a lot of guidance and a wealth of first-hand experience working with science-grade detector technology.

I'd like to thank Professor Chris Groppi for being such an approachable and extremely helpful mentor. He was always willing to lend me lab equipment or meet one-on-one in his office for an impromptu discussion. His SESE instrumentation class was one of the most useful courses I've ever taken, and I owe much of my knowledge of CAD modeling, cryogenic systems, and circuit design to him as a result.

Thank you to Todd Veach, my grad school predecessor, who established the Lab for Astronomical and Space Instrumentation where I conducted my research. He

also helped to dream up a lot of the ideas that became the basis for my research projects. LASI is one of cooler labs in ISTB4–in my humble opinion!

A big thanks to Shouleh Nikzad's Advanced Visible/UV Detector and Imaging Systems Group at JPL who hosted me for a Graduate Fellowship over couple of summers as well as on the CHESS payload development. Sam Cheng, Tim Goodsall, April Jewell, Alex Carver, and several others, are not only exceedingly bright leaders in their field but were extremely accommodating toward me and helped me gain a wealth of hands-on experience.

It wasn't always me alone toiling away in the lab with the lights off, so a very big thanks to all the undergrad and grad students who worked alongside me at various times in LASI. Special thanks to Priya Challa who helped me setup and conduct preliminary tests on the HERESY instrumentation, Hamdi Mani, who is unbelievably skilled at designing and building cryogenic systems and helped me often, Rhonda Holton, who spent some long nights with me in the lab writing code and hanging out with the hexapod, and Ravi Prathipati who was my right-hand man for a long while and helped a ton with the daunting tasks of disassembling, wiring, cleaning, and reassembling cryogenic systems. Also thank you to Gena Pilyavsky, Jake Trahan, Ronnie Ramirez, and Rocky Camarena for your collaboration and camaraderie.

Thanks to Steward Observatory in Tucson for allowing me engineering observing time on the Kuiper 61" telescope. Especially to Joe Hoscheidt who was endlessly accommodating with whatever crazy equipment we threw at him to attach to the back of the telescope. Getting to work and take on-sky measurements at a professional observatory is an experience I will never forget.

TABLE OF CONTENTS

Page

CHAPTER

CHAPTER Page

CHAPTER Page

CHAPTER Page

LIST OF FIGURES

Figure Page

Figure Page

Figure Page

LIST OF TABLES

Table Page

1 INTRODUCTION

Rapid scientific innovation by the astronomical community requires the development of new Ultra-Violet/Visible/Infra-Red range (UV/Vis/IR) astronomical instrumentation that use novel approaches to improve imaging and increase the accessibility to observing time for research groups. This dissertation discusses a multi-faceted approach to building and testing unique astronomical instrumentation that required rapid-prototyping, cost-effectiveness, and the use of ground and space-based platforms for payload validation and the increase of Technology Readiness Level (TRL). In addition to cost effectiveness, emphasis was placed on design flexibility so that, for instance, different types of sensors could be used with the same payload with only slight modifications, and in another example, that the instrument design would have little to no impact on the hosting optical system, so that the imaging payload could be used in a 'plug-and-play' mode.

Balloon, suborbital rocket, and ground-based instrument developments were explored in this thesis. Balloons and suborbital rockets serve as affordable platforms for collecting data with minimal interference from Earth's atmosphere and operate close enough to the space environment that they serve as a proxy for space-rating instrumentation. Balloon platforms such as the Wallops Arc Second Pointer (WASP) (Stuchlik, 2017) and the Stratospheric Terahertz Observatory (STO) (Walker et al. 2010) have provided sustained arcsecond pointing, but their imaging systems are still susceptible to micron-level jitter in the payload that is caused by a variety of environmental factors. Similarly, suborbital rocket platforms provide the ability to collect data at Low-Earth Orbit (LEO) altitudes, including unrestricted access to the

UV, but their instrumentation must be designed to survive the additional rigors of ballistic launch and be able to operate in the harsh space environment.

In contrast, ground-based observatories have the advantage of providing a stable environment and physical ease-of-access while in use but must remove refractive atmospheric effects when attempting to deliver high-resolution imaging. Most large observatories have addressed this issue with the use of advanced adaptive optics that can deliver near-diffraction-limited observing from the ground. However, there are hundreds of smaller-class ground-based observatories across the world that cannot do this, and that would benefit from a plug-and-play instrument that could increase imaging resolution without the introduction of any additional optics to the telescope beam path.

1.1 Science Drivers

The need for UV/Vis/NIR imaging systems that are compact, low-cost, constructed from commercially off-the-shelf (COTS) instrumentation, and provide high-angular resolution are in high demand in the astronomy community. Ground, balloon, and sounding rocket-based astronomy represent the 'big three' in low-cost, high science return imaging platforms, and this dissertation details the development of an imaging solution for each. Key areas of scientific areas of interest are 1) (balloon-based) UV/Vis/NIR gas giant time-domain individual storm tracking, zonal wind velocity characterization, and chromophore characterization, 2) (sounding rocket based) Far-UV spectral characterization of translucent cloud dynamics in the Local Interstellar Medium, and 3) (ground based) observatory resolution enhancement to improve image quality and increase observing efficiency (by SNR increase) of Vis-NIR imaging campaigns.

Payloads optimized for suborbital observing (balloons and sounding rockets) can provide cost-effective access to the UV. For a planetary balloon observing campaign, Near-Ultra-Violet (NUV) wavelengths (~200-350nm) allow for the potential of diffraction-limited ~0.1" imaging for tracking of individual gas giant storm dynamics over time. A multi-month NASA long-duration balloon mission would potentially enable time-domain storm tracking on all the gas giants over the length of the flight. A sounding rocket mission allows for short term imaging (~900seconds) to be collected from LEO-equivalent altitudes, at altitudes an order of magnitude larger than attainable by balloons. While not having the duration capabilities of balloons, this increased altitude allows true separation from the Earth's atmosphere and provides access to the Far-UV (FUV: 100-200nm) spectral regime, which is already incredibly challenging to detect due to its opaqueness to many types of optical materials and highly susceptible to atmospheric absorption.

As for ground-based observatories, dozens of highly advanced Adaptive Optics (AO) systems already exist that employ combinations of high speed wavefront sensing, deformable mirrors, and tip-tilt adaptive-optics to provide near-diffraction-limited imaging. However, there are still several dozen meter-class telescopes around the world that do not have advanced AO that could benefit from a 'plug-and-play' system that can be mounted at the focal point of any telescope and make an improvement to image quality. Nebulae structure, protostellar systems, and objects in our own solar system becomes finer and brighter as atmospherically scattered photons are 'caught' by the actively tracking focal plane to minimize light being smeared across pixels and increasing the signal recorded per pixel. The active correction improves not only the data quality, but also increases the efficiency of the overall observing campaign by lowering required exposure times.

1.2 Engineering Drivers

This dissertation describes the construction, verification, and implementation of three imaging systems that each demonstrate a unique optomechanical approach to UV/Vis/NIR imaging. The trend across astronomy grant funding organizations is toward an increasingly competitive proposal process combined with reduced proposal funding that makes the low-cost and Commercial-Off-The-Shelf (COTS) instrument selection and fast-prototyping aspects of new imaging systems very attractive. With this in mind, an actuated focal plane prototype known as the HExapod Resolution-Enhancement SYstem (HERESY) was designed, implemented, and tested and is presented here.

HERESY is a cryostat-based instrument that simultaneously allows a COTS non-cryogenic hexapod to operate in the 0-50 °C range while at the same time having a cryogenically-cooled Charge-Coupled Device (CCD) mounted to its face. This is done through a creative combination of a liquid nitrogen tank that couples with a flexible copper cooling structure clamped to the science detector, the use of low-thermally conductive materials for the interface between the hexapod and focal plane, and heaters to prevent a thermal gradient from forming across the hexapod.

For imaging, a pointing error signal is established for which the hexapod actively corrects. The imager on the hexapod plane then takes exposures through the cryostat window. In this way, HERESY performs tip-tilt correction, but without the introduction of any additional reflections into the system.

The true benefits of HERESY are its low-cost focal plane customizability, and ease of integration into almost any existing optical system. Two unique focal planes were tested on the HERESY platform, the first optimized for suborbital balloon telescope use to provide high-resolution imaging through balloon gondola jitter reduction, and the second being a guidestar tracker setup that measures the atmospheric turbulence of a bright star at a fast rate and produces an error signal for which the hexapod can then correct.

In addition to HERESY, I describe a multi-year engineering effort to design, fabricate, and characterize a Far-UV optimized detector payload for the CHESS sounding rocket mission. The project was a collaboration between JPL, ASU, and CU – Boulder, where JPL provided a custom CCD, ASU (myself) was responsible for integrating and testing the detector in a rocket-viable payload, and Boulder was responsible for accepting the payload for a final integration into the rocket. This effort involved extensive testing to both mechanically ensure the payload could withstand the rigors of a rocket launch and to ensure the detector met the stringent noise and efficiency requirements of the mission through optoelectrical characterization. The main engineering goal for this project was the implementation of a platform by which the TRL of JPL's UV-optimized CCD could be increased to 'space-rated' by successfully flying it in the relevant environment.

1.2.1 State-of-The-Art Image Stabilization Technology

The HERESY instrument is an image stabilization instrument originally developed for use aboard a balloon and later modified for use to correct for image blurring due to atmospheric turbulence in ground-based observatories. HERESY actuates the focal plane itself to correct for the pointing error of the target image. However, two similar advanced techniques currently used in astronomy that must be noted are fast-steering mirrors and orthogonal transfer CCD (OTCCD) instrumentation.

Astronomical fast-steering mirrors are placed in the optical beam path and fed an error signal. These mirrors then make high speed tip-tilt corrections to the beam to stabilize the incoming light and decrease blurring before it illuminates a detector. These systems can make tip-tilt corrections to the incoming light at speeds upwards of ~800 Hz, but for dim observations, introduce an additional reflection leading to light loss and increased integration times (Tian et al., 2016).

OTCCDs are a specific type of CCD architecture designed to shift charge in any XY direction during image exposure to eliminate blurring across pixels due to the motion of the target itself, shaking of the telescope, or image motion caused by lensing of the target image by atmospheric turbulence. However, the corrective abilities of OTCCDs are limited by the detector readout speed of the CCD array which cannot be clocked much faster than 1 MHz to manage read noise. A large-scale OTCCD system was developed for the WIYN telescope (Wisconsin, Indiana, Yale, NOAO Telescope) at Kitt Peak and is limited to ~30 Hz of imaging correction (Burke et al., 2004).

While the iteration of the HERESY instrument described in this paper cannot correct for pointing error with the high frequencies of fast-steering mirrors, it has the advantage of not introducing any additional reflections to the optical system maximizing throughput. In addition, by actuating the focal plane itself for error correction, HERESY can accomplish exactly what OTCCDs set out to do except at a higher frequency and with the flexibility to mount nearly any detector of choice onto the focal plane.

1.3 Balloon-based Astronomy

The real advantages of balloon-based astronomy are the low-cost, space-like observing conditions (little to no atmosphere interference) they provide, while launch and flight loads are incredibly forgiving – when compared to rockets. The downside to ballooning is that balloon vehicles fly directionally at the will of local stratospheric wind patterns and are subject to solar effects. This means that many balloon flights are terminated after less than 24 hours.

To enable longer missions, Arctic and Antarctic launches use a ballast system that regulates the payload altitude and leverages the polar vortex circular wind patterns to enable missions for as long as 100-plus days. In recent times, companies such as Google Loon and World View Enterprises have demonstrated multi-day flights within the 60°N and 60°S latitudes showing promise for the higher accessibility of astronomical balloon flights in the near future (Miller, 2018).

The other challenge for observational astronomy aboard a balloon is pointing or attitude control. Balloon payloads are typically suspended by soft-goods tethers that tend to sway in the wind or twist. Structure is added for increased torsional stability and complex gondolas are available now that can gyroscopically correct for balloon movements to enable telescope pointing down to the arcsecond level. Despite this incredible amount of stability, the maximum imaging angular resolution of balloon telescopes is still limited by the pointing error due to a jitter error signal propagated to the focal plane from the operation of onboard mechanisms and various other environmental factors.

1.4 Sounding Rocket Astronomy

Sounding rockets are an affordable platform for space-based data collection and an excellent proving ground for instrumentation slated to fly on future Earth orbit or deep-space missions. Instruments that can survive launch and successfully operate in a vacuum above at >100km altitudes can rapidly increase their TRL to level 7, which states that a "system prototype demonstration in a space environment" has occurred (Dunbar, 2012) – typically a key NASA requirement before proposal for flight aboard a major mission.

Sounding rockets operate well above Earth's atmosphere (using the Karman definition of 100km). The benefit of this for astronomy is full spectral access without any detrimental atmospheric effects (despite operating higher than 90% of Earth's atmosphere, balloons still deal with atmospheric full absorption and scattering of sunlight during daytime operations) (Dankanich, 2016). The parabolic peak of the rocket trajectory sends the vehicle into the vacuum of space where it experiences a period of 'zero-G.' In these conditions, unlike balloon vehicles that must develop complicated platforms and mechanisms to sustain arcsecond pointing while dealing with stratospheric weather, rockets are not susceptible to wind and can use reaction wheels to establish 1 arcsecond sustained pointing like an orbital satellite. However, as a result of this parabolic trajectory, science data collection is limited to ~15 minutes before the vehicle arcs through the peak of its curve and falls back to Earth (NSROC, 2001).

Instrumentation that fly on sounding rockets must be rigorously tested to ensure they can survive the harsh launch conditions and space environment. The most intense of these tests involve vibration testing at the component and integrated level to ensure launch survival and vacuum chamber testing to ensure that electronic systems do not overheat, and equipment does not display detrimental outgassing, which can coat sensitive optics equipment.

1.5 Adaptive Optics in Astronomy

The angular resolution of ground-based observatories is limited by image blurring due to local atmospheric turbulence. This effect, known as 'seeing-limited angular resolution,' is defined as:

$$\theta \approx \frac{\lambda}{r_0}$$

where θ is the angular resolution achievable, λ is the wavelength of the observation, and r_0 is the atmospheric coherence length (Wizinowich, 2009). To remove this effect and achieve an angular resolution closer to the diffraction limit of the telescope, adaptive optics (AO) technology is commonly used on ground-based systems that uses a series of complex instruments and optical techniques to remove image distortion from the incoming wavefront. The approach involves rapidly characterizing the incoming deformed wavefront shape, correcting the wavefront through the use of dynamic optics, and then passing the corrected collimated wavefront on to the science detector for data collection. To accomplish this a fraction of the incoming light from an area of the sky near the science target of interest is diverted to a wavefront sensor.

Often Shack-Hartmann wavefront sensors are used that separately sample the incoming wave plane via a series of small lenslets. A natural guidestar can be used as the wavefront sensor for imaging applications, but such stars must be very bright since their signal is sampled at frequencies as high as ~500Hz – 1kHz. Such targets might include bright stars, planets, or galactic nuclei. However, natural guidestars that are bright enough to be used with fast-sampling wavefront sensors make up only about 1% of the sky on a given night. To solve this problem, observatories typically also use powerful sodium lasers as part of their AO system that, when beamed into the sky near the astronomical science target, interact with the mesosphere and provide an artificial bright fiducial on the sky. This allows for wavefront sampling in whichever part of the sky that the telescope is pointing (Wizinowich, 2009).

After a guidestar (natural or laser produced) is acquired by the wavefront sensor, each lenslet then projects an image of that section of the wavefront onto a detector and the deformation of that part of the wavefront moves the image away from where it should be – producing a delta in position for each wavefront segment that can be measured. The tip and tilt of these delta positions are then used to calculate the complex deformed shape of the incoming wavefront. The wavefront sensor data is then used as part of a control loop that drives the operation of high-speed dynamic optics that perform the wavefront correction. A deformable mirror is used to correct for delta positions recorded by the wavefront sensor. While the tip-tilt corrects for macroscopic errors from the centroid of star's PSF, a deformable mirror warps to correct for the actual 3D shape of the incoming wavefront (if a deformable mirror has enough stroke, sometimes AO systems do not need a tip-tilt mirror). The turbulent wavefront ‘flattens’ and enables close to diffraction-limited observing at the science detector.

2 HEXAPOD RESOLUTION ENHANCEMENT SYSTEM (HERESY) – BALLOON CONFIGURATION

2.1 Background

Within the last decade there has been a ramp up in suborbital balloon-based astronomy since the platform is arguably the 'best of all worlds' for UV/Vis/NIR observations. What makes balloons so desirable are: (1) at altitudes >30km there is little to no spectral absorption by the atmosphere, (2) they are more cost effective and less risky than launching an orbital telescope, and (3) they can focus on taking repeated data on select targets to measure change over time whereas orbital and ground-based telescopes are often overbooked. Suborbital sounding rockets share many of the advantages of balloons, achieve higher altitudes, and guaranteed sub-arcsecond pointing (Kremic et al. 2013). However, such rocket instrumentation must be designed to survive the high-G launch environment and the platform typically allows a total observation time of less than 10 minutes per launch (Kane et al. 2011). Therefore, aside from achieving full orbit, balloons are the only platform that can provide long time-domain observations over the entire UV/Vis/NIR bandpass.

The main challenge balloon gondolas face is that they are often subject to high-speed stratospheric winds while being tasked with providing sustained arcsecond pointing. Balloon gondola stabilizing technology can eliminate pendulation and large non-periodic motion of payloads, by using combinations of torsion bar assemblies, gyroscopes, and reaction wheels. These systems work together to enable an amazing 1-2 arcsecond pointing (Kraut et al. 2008). However, balloon gondolas still cannot achieve the sub-arcsecond pointing level since microscopic jitter terms remain, which cannot be removed by the gondola's systems alone. These jitter movements arise from such things as wind rushing by payload or balloon surfaces, cryocooler operation, reaction wheel vibrations, and thermal variations. For dim targets this means images requiring long integrations will become blurred by the jitter movements during data collection, effectively limiting the resolution of the system. To remove this final jitter term and allow for sub-arcsecond balloon pointing ability, additional corrective instrumentation must be used (Hibbitts et al. 2013). This is conceptually demonstrated in Figure 1.

Currently, Fast Steering Mirror (FSM) systems are being used for this purpose. Within the last five years the Balloon Observation Platform for Planetary Science (BOPPS) (Diller et al. 2015), the High-Altitude Lensing Observatory (HALO) (Rhodes et al. 2012), and the Sunrise Mission (Barthol et al. 2010) have all employed FSMs. However, FSMs introduce signal loss due to additional reflections and require extra optical design to function, which in turn increases camera integration times. In contrast, the instrument detailed in this chapter corrects for pointing error by actuating the focal plane using a hexapod rather than the incoming beam. This instrument is known as the HExapod Resolution-Enhancement SYstem, or HERESY. The advantage of HERESY is that the hexapod system can be placed at the focal point of any existing instrument and function with no additional optical design.

The long-duration balloon Stratospheric Terahertz Observatory (STO) mission (Walker et al. 2010) flown over Antarctica serves as an excellent analog for the platform that HERESY was designed to fly on. It is worth mentioning that other gondolas, such as the ones used for WASP and FIREBALL (Stucklik 2015 and Milliard et al. 2010), are also capable of sustained arcsecond pointing, but the STO team kindly provided a 100 Hz sampled error signal to be used for the development of this project. The STO gondola used a sophisticated pointing system comprised of gyroscopic mounts and reaction wheels to correct for swaying motions caused by high altitude weather. An azimuth-elevation servo system that corrects for azimuth using a reaction wheel and Momentum Transfer Unit (MTU) and elevation by direct-drive motor mounted to the telescope. Smaller corrections are made by using a star tracker in conjunction with gyroscopes and tilt sensors to stabilize telescope pointing down to an impressive 1 arcsecond (Bernasconi 2011). Nevertheless, 1 arcsecond remains a pointing limitation of their approach due to a persistent jitter term that would require an additional stabilization step like the hexapod to remove.

2.2 Science Objectives

The 2011 Planetary Decadal Survey ("Vision and Voyages for Planetary Science in the Decade 2013-2022." 2011) identified the need for increased time-domain planetary observations across the UV/Vis/NIR. Ground-based observatories cannot observe in atmospherically opaque wavelengths, notably in the UV, and space telescopes are too overbooked to provide constant planetary observations. Therefore, suborbital balloon platforms have been identified as a cost-effective solution for long-duration planetary observations.

Flying on an Antarctic Long-Duration Balloon (LDB) mission (~100 days), HERESY can track and characterize individual storms for all the giant planets with Hubble-like angular resolution, stable photometry, and a high exposure cadence. Several narrow-band filters will be leveraged to peer through upper cloud decks and obtain three-dimensional views of storm activity to give new insights on giant planet vertical and horizontal cloud structure, how internal and external heat sources affect circulation, and a characterization of zonal cloud velocities. Observations will be collected daily from the stratosphere for months producing a clearer picture for how the gas giant storm systems and global processes dynamically evolve over time. A Science Traceability Matrix detailing what HERESY could accomplish on an LDB mission can be found in Table 1.

2.2.1 Discrete Storm Tracking

Individual storm systems are ever-present on all the gas giants and are in many ways structurally similar to large thunderstorm systems on Earth although larger by a factor of ~10 vertically and ~100 horizontally (Gierasch et al. 2000). UV/Vis/NIR observations will allow imaging of different layers of gas giant cloud systems allowing production of three-dimensional video representations of cloud systems as they evolve in real time. This multi-layer 3D analysis will help constrain storm rotational speeds and energy content.

The multi-month continuous observations of these storm systems on an LDB flight will allow HERESY to constrain both the duration of these storms, their spatial distribution, and their frequency of occurrence. Figure 2 shows examples of discrete storms on Jupiter and Saturn from ground-based observatories and the Cassini spacecraft. Figure 3 shows the evolution of a series of discrete storms on Neptune taken over a period of 2.5 hours from a ground-based observatory. It is important to note that since the water layer is deeper in all of the gas giants beyond Jupiter, distinct storm features of Saturn, Uranus, and Neptune are much more challenging to detect (Scowen, 2014). Therefore, while discrete storms on all gas giants will be observed, Jupiter will be the primary focus. Table 2 gives the angular size of storm features for all the gas giants at opposition.

2.2.2 Gas Giant Wind Tracking

Gas giant wind vectors are determined by repeatedly resolving cloud tracers for periods of hours to days. With enough time-domain observation, entire global zonal velocity maps can be produced displaying wind speed versus latitude. Figure 4, from Asay-Davis et al. 2011, shows a zonal velocity plot for Jupiter with data taken from different platforms over several decades of observations, which highlights large variations in Jupiter's zonal velocities over the years.

In-depth velocity fields for areas of nterest are also produced. A great example would be the tracking of persistent anti-cyclonic activity such as the Great Red Spot of Jupiter. The development of long-lived vortices requires mechanisms for convective turbulence and sometimes mergers with other smaller vortices. These persistent vortices are also responsible for transporting large amounts of energy from gas giant interiors toward their upper atmospheres (Legarreta et al. 2008). Therefore, the ability to track zonal winds surrounding the formation and dissipation of these vortices could go a long way toward better understanding giant planet vortex dynamics.

2.2.3 Filter Set and Expected Integration Times

Table 4 is a list of filters to fly with HERESY to maximize the quality of the imaging data and accomplish its science objectives. The filters span the near-UV to near-IR and feature filters strategically chosen to target certain aspects of gas giant cloud layers. The vertical structure of discrete storms can be determined by using a series of methane absorption narrow-band filters (Gierasch et al. 2000). This same technique was used by the Galileo and Cassini spacecrafts to image both Jupiter and Saturn's cloud features.

In contrast to Jupiter and Saturn, methane levels on Uranus and Neptune are too prevalent to look for specific CH_4 absorption features in the clouds by themselves. As a result, an additional hydrogen absorption feature is used to first determine the concentration of methane above clouds decks. Then the methane filter images can be calibrated and analyzed to bring out more structure in the clouds (Scowen 2014). Several continuum filters will be used as a baseline for interpreting cloud reflectivity and to remove any false interpretations caused by cloud chromophore effects.

Since the gas giants rotate quickly, imaging targets can smear during an exposure lasting too long (thereby defeating the purpose of correcting for jitter in the first place). Therefore, Table 3 shows expected maximum exposure times for HERESY imaging per gas giant. The storm feature sizes in Table 2 were coupled with planetary rotation rates with the requirement that no tracked object shall be smeared by planetary motion by more than one quarter of an images PSF. This yields approximately 25 second max exposures for Jupiter and up to 200 second for Neptune.

2.3 Engineering Drivers

The instrumentation requirements for HERESY's balloon design flow directly from the Science Traceability Matrix in Table 1. A description of high-level engineering requirements can be found in Table 5. To prove that the prototype of the hexapod instrument works in the lab, the motion characteristics of the hexapod were exhaustively tested, integrated into a vacuum cryostat, and then operated with a cryogenically cooled CCD on top of it while precisely controlling the thermal environment of the instrumentation. As a proof of concept, pointing-error jitter data from the long-duration balloon STO mission that was flown over Antarctica was utilized. The jitter data was provided at 100 Hz by a guide camera mounted on the balloon telescope and shows that the average jitter to correct for is a maximum 20 micron amplitude term that propagates around 25 Hz. This instrument was engineered using the STO data as a baseline for focal plane jitter corrections.

In addition to the components selected to makes up the HERESY assembly, a verification and validation strategy was formulated, and a test bench was setup with carefully selected instrumentation to ensure all requirements were met. However, before any instrumentation was selected or any testing conducted, a thorough analysis of balloon jitter from the STO mission was performed.

2.3.1 Jitter Analysis

The STO data was acquired using a guidestar system that monitored on-sky targets, therefore the data is provided in units of arcseconds for target pointing error as a function of time. For this pointing error data to be useable to drive the hexapod and XY stages, it had to be converted from an angular displacement across the sky to a linear displacement of the image across STO's focal plane. To convert the data, the plate scale formula was used to transfer arcsecond pointing error into millimeter displacement (Howell, 2006). With this conversion, the XY stages and the hexapod could be driven by an error signal that represents the displacement of the STO imaging target across the focal plane surface, which is what the hexapod must counteract on a mission for image stability. Plots of the STO jitter can be found in Figure 5.

A Fourier analysis of the image displacement amplitude at the STO focal plane was conducted using a Fast-Fourier Transform in MATLAB to pull out the frequency content of the STO jitter signal, seen in Figure 6. There is a marked spike in the distribution at 25 Hz that is a factor of 3 stronger than any other component in the spatial frequency spectrum. By Nyquist Theory, the frequency content of the STO signal could technically be detected up to 50 Hz (sampling frequency/2), however, spectral analysis of signals close to the Nyquist Limit tend to be less accurate and can be susceptible to reflections from outside the boundaries of the analyzed data. Therefore, to prevent confusion and inaccuracies in the spectral analysis, frequencies above 30 Hz were thrown out so that each plot point represented at least three or more times the sampling rate of the data. Furthermore, in exchanges with the STO team members, it was reassured that they had obtained jitter data at a much higher sampling rate and cross-confirmed the validity of the 25 Hz primary frequency for the jitter signal (Groppi 2013).

Analyzing the data, the ramp-up of low frequency error in the 0-5 Hz range comes from a slow swaying motion that was unable to be corrected by the STO gondola and has amplitudes of up to +/- 1 mm in the focal plane. Such low frequency motion can easily be corrected for by other mechanical systems in the gondola design such as a yoke mount between the balloon tether and the gondola mounting strut, or by the introduction of gyroscopic stabilization in the gondola itself, and so these frequency components were not a major design driver for the hexapod system. However, there is a significant peak close to 25 Hz that is known in part to be caused by thermal variations, cryo-coolers, the movement of reaction wheels, etc. These higher frequency terms are impossible to correct using gondola technology alone, therefore the ability to correct these terms are one of the main engineering drivers behind the development of the hexapod instrument.

2.4 Instrumentation

After the hexapod design passed CDR, instruments and other necessary laboratory tools had to be procured, operated, and interfaced together. To reduce cost almost all components were purchased off-the-shelf (OTS). Aside from lower cost, another advantage of this approach is that OTS products almost always are provided with good documentation and operating manuals. The disadvantage of the low-cost OTS approach is that it was often challenging to mesh the existing electrical, mechanical, and software interfaces between the differing vendors. As a result, numerous programs in Python, C/C++, LabView, and IDL were written to make different instruments work in together and several mechanical interfaces were fabricated for the mounting of components.

2.4.1 Hexapod

The hexapod is a Physik Instrumente (PI) H-811DV vacuum-compatible 'microbot' that was chosen for its positional accuracy, agility, and robustness as an OTS product. After a thorough trade, this instrument was chosen to satisfy high-level requirement #1 (Table 5). It is specified for a top speed of 10mm/s and a positional accuracy of 40nm. Images of the hexapod in the lab are found in Figure 7 and manufacturer specifications can be seen in

Table 6 (*H-811 Vacuum-Compatible Miniature Hexapod 6-Axis Positioner.* 2013).

It was known that there would inevitably be a lag-time between the hexapod sampling the jitter error and completing a corrective motion, therefore it was important to choose a device that could move much faster than the jitter. The hexapod is also a compact device that mounts well in typical cylinder-shaped cryostats. Aside from all the benefits of selecting an OTS hexapod, the challenge is that it was not intended for cryogenic operation. Managing both overheating and freeze-out were concerns that were designed for, since the hexapod produces a lot of heat from its circuitry and motors as well as the fact that the CCD attached to the top of it was cryogenically cooled. It was ensured that the hexapod was heat sunk to the outside of the vacuum chamber to simultaneously prevent overheating or excessive cooling, while at the same time providing heaters to prevent harsh temperature gradients.

2.4.2 CCD and Leach Controller

The CCD for the prototype is a broadband-coated e2v 47-10 AIMO 1k×1k back-illuminated device (Figure 8). Like the hexapod, this CCD was chosen for its heritage as a proven OTS product. The 47-10 also displays many of the same characteristics that one would expect of a science-grade detector (low read-noise, low dark current, high broadband QE, etc.), therefore it is a good analog for the type of detector that would be selected for a proposed balloon mission. The 47-10 CCD also helps satisfy high-level requirement #3 (Table 5).

Operation and readout of the CCD are handled through an Astronomical Research Cameras (ARC) two-channel Leach Controller (Leach, 2012). The controller provides the DC voltages and AC timing signals to operate the device and reads out the CCD video with a 16-bit ADC. Input/output from the controller to the CPU is done over fiber optic cable. The controller is also capable of precisely operating a shutter by

TTL on/off signal. With the current setup, readout time for the 47-10 device through the Leach Controller is approximately half a second per image (easily satisfies high-level requirement #4 (Table 5)). Another benefit of this device is that it can take short exposures while operating at room temperature (longer exposures without cooling the detector are saturated by dark current), which was useful for testing the overall system before any cryogen was introduced.

2.4.3 Cryostat and Thermal Control

When cooled to cryogenic temperatures, the CCD must operate under vacuum to prevent condensation and ice from forming on the surfaces of sensitive electronics. As a result, the hexapod and CCD are mounted inside a custom-built cryostat that includes vacuum feed-through connectors for both the CCD and hexapod electronics as well as a large window through which light can be focused. The cryostat setup with the hexapod and CCD mounted inside satisfies high-level requirement #2 (Table 5). An image of the cryostat in the lab can be found in Figure 9 and a 'cutaway' with all components labeled can be found in Figure 10.

A turbo pump system brings the large interior volume of the chamber down to 10^{-7} Torr. The cryostat's liquid nitrogen tank can be filled in any orientation, and a cryogenic hold time of approximately thirteen hours in the lab was measured. Included in the cryostat is also a large charcoal getter that helps maintain a good vacuum by absorbing excess moisture and outgassing materials.

The complete cryostat thermal system was exhaustively verified to mitigate the risk of over-heating or over-cooling of any instrumentation. The hexapod was first placed into the cryostat under vacuum and continuously operated for several hours.

The hexapod produced heat from its operation, but since the base of the hexapod is heat-sunk to the cryostat shell it dissipated enough heat to equilibrate at ~37 °C. The hexapod is specified to function from 0-50 °C, so this temperature is well within its limits.

A Lakeshore 336 Temperature Controller is used to manage the thermal conditions of various components inside the cryostat. The 336 Lakeshore model includes four temperature inputs and two heater outputs. Four diode temperature sensors are placed at the CCD, hexapod top, hexapod base, and the cold plate (liquid nitrogen cooled interface). 25W cartridge heaters are placed at the CCD and at the hexapod top. The CCD heater holds the CCD at a preset operating temperature and the heater on the hexapod top prevents a temperature gradient from forming across the hexapod due to during CCD cool down. A plot of the heater duty cycle can be found in Figure 11.

Despite the CCD being conductively buffered from the hexapod by G10 fiberglass, there is enough thermal conduction to begin to cool the hexapod top dangerously toward the hexapod's 0 °C operating limit. Since the hexapod base is heat-sunk to the shell of the cryostat, in the lab environment, the hexapod base remains within +/- 5 °C of room temperature (25 °C). Therefore, to both prevent the hexapod from cooling out of specification or a large temperature gradient from forming across the hexapod chassis, which could cause undue thermal stressing during operation, a thermal requirement was imposed that no part of hexapod chassis should exceed 15 °C from any other part of the hexapod chassis during operation. For example, if the hexapod's base temperature is measured at 32 °C, then the temperature controller is set to hold the hexapod top at 17 °C.

The 336 controller has an auto-tuning feature that can determine the ideal PID values for a preset heater and temperature sensor setup. After auto-tuning, the 336 can operate the 25W heater to hold the hexapod top to +/- 1 ºC of a setpoint temperature. An overall thermal profile of HERESY taken during its standard operation can be found in Figure 12.

2.5 Verification and Validation Equipment

After acceptance and initial functional checkout, the instrumentation needed to be validated per the requirements. To accomplish this, a test bed had to be designed and implemented to closely mimic what the instrument would experience during flight. Due to the precise nature of the positioning requirements (micron-level), XY stages were procured to imitate the on-sky error signal, infrastructure to remove laboratory vibrations was implemented, and a laser positioning system was used to cross-confirm stage positioning.

2.5.1 XY Stages

As part of the experimental lab setup, XY stages are employed to recreate a close approximation of the STO jitter as well as having the capability to synthesize a random jitter when needed. Like the hexapod, these stages were also obtained from PI. The XY stages have a slightly higher top speed than the hexapod at 13mm/s, and at first glance one might ask if they could accomplish the same job as the hexapod (since they are about ten times cheaper in cost). However, the stages do not have near the positional accuracy of the hexapod, are much bulkier (approximately twice the footprint when fully setup), and are not vacuum-rated.

The usefulness of these stages is that they can closely approximate the jitter error seen on a balloon mission, and by mounting a target on the stages, the CCD can take exposures while the hexapod is actively stabilizing the image. The images can then be analyzed to see how accurate the image stabilization performed by the hexapod was.

2.5.2 Position Sensitive Module (PSM)

Position information for the movement of the hexapod and XY stages can be obtained from software or from taking images of a target with the CCD while the translational stage of choice is in motion. However, the most precise verification of the displacement and frequency of the movements come from using a laser/retroreflector/PSM setup that has both a high positional and sampling resolution.

For this project an On-Trak PSM that measures position by locating the center of intensity of any light source shone on it was chosen. An image of this position sensing equipment is found in Figure 13. The selected light source is a 5 mW focusable red laser, with a focused spot size of 0.5mm. To avoid oversaturating the PSM, a neutral density filter is placed in front of the diode's photo-sensitive area. A vendor-provided Printed Circuit Board (PCB) then amplifies and performs on-circuit calculations and turns the PSM output into voltages that reflect an XY position in mm. The final XY voltages are then read out using a fast-sampling National Instruments Data Acquisition (NI-DAQ) system.

The system has been measured in the lab to detect movements as small as 1 micron (measurement found in Figure 14). Additionally, the NI-DAQ can sample the laser's position from the PSM in the kHz range, but in the interest of reducing data load. The diode output was typically sampled at 300 Hz which kept the data quality well above the Nyquist limit by a factor of ten.

2.5.3 Vibration Isolation Bench

A key requirement for this project was the ability to accurately measure laser displacements to better than 6.5 microns (half the width of a pixel on the CCD), so it was important to ensure that the vibration environment of the laboratory would not interfere with the experiments. To isolate the optics from the lab building, the instruments were mounted on an isolation bench that 'floats' the mounting surface on four pneumatic gimbal-pistons. For the isolation bench to work, a constant stream of compressed air is supplied to the pistons, which in turn keep the mounting surface isolated on compressed air pockets.

To first measure laboratory vibration, the PSM was mounted to the isolation bench and the laser was mounted on a tripod. The PSM sampled vibrations at 400 Hz and measurements were conducted for 15 minutes per run to note any significant changes in the vibrations over time. Building vibrations were measured to have maximum amplitudes in the tens of microns. Factors such as elevators, air filtration systems, and machine shop equipment were suspected in contributing to this background vibration. A plot of this test setup can be seen in Figure 15. The measurement was then repeated, but this time after placing anti-vibration gel under the legs of the tripod. The idea was to isolate the laser to estimate the extent of vibrations that were affecting the optics bench.

The results from this second experiment showed the optics bench to be dampening the building vibrations down to a maximum of two microns. It is worth noting that there was experimental error introduced with the tripod/anti-vibration gel method of measurement, but nonetheless a two-micron 'background noise-factor' was well within the measurement requirement. A plot of the optics bench effect of dampening the lab vibrations is found in Figure 16.

2.6 C++ Jitter Tracking Code

The hexapod can identify and calibrate itself to its 6-axis zero points with sub-micron accuracy. After this calibration, the hexapod can then be commanded to move with respect to its zero points to high accuracy. One function of the PI software is to set the hexapod to always reach a commanded position before ever attempting to move to the next position. However, in this case one could imagine an outlier in otherwise 'smooth' jitter data that would cause the hexapod to take a long time to reach the outlier's location before starting its next movement. Therefore, a function was written that commands the hexapod to achieve each commanded position as fast as possible whether it had reached its previous position or not.

To simulate the STO jitter, the raw X and Y error signals were written into a two-column text file and then accessed by the C++ code line-by-line, with a delay representative of the sampling rate of the STO data, that then can be used to drive either the XY stages or hexapod. To simulate a flight-like condition, only the XY stages are driven with the STO signal and then the hexapod tracks the XY stages via an "error signal" generated by the laser and PSM setup. This is similar to how a star tracker would deliver an error signal to the hexapod on an actual balloon flight and will be discussed in more depth in later sections.

2.7 Phased Approach

This project's approach was structured around a three-phase procedure to first test the capabilities of the subsystems in the design and then to advance to controlled introduction of both vacuum and thermal conditions appropriate for each instrument. Phase I involved the acceptance testing of each instrument in ambient lab conditions and the first proof that the hexapod was capable of matching balloon jitter. Phase II introduced the hexapod and CCD into the cryostat environment and again proved the ability of the hexapod to correct for balloon jitter – this time while under vacuum. Finally, Phase III involved the cryogenic cooling of the CCD while the hexapod corrected for jitter and maintained its allowable operating temperatures. In conjunction with the hexapod jitter correction, the CCD was used to take exposures of an imaging target to test the corrective performance of the system.

2.7.1 Phase I Overview

Phase I involved the acquisition and acceptance testing of all the components in the prototype and the experimental lab setup. The hexapod and XY stages were first visually inspected to move in the expected way when commanded with larger offsets. The stages where then authentically confirmed to meet requirements using the laser / retroreflector / position sensitive diode (PSM). After the stages were proven to work, they were then separately driven with the STO jitter signal and once again measured using the PSM to confirm that they could at minimum match the speed and amplitude of the signal.

At this stage the hexapod was not actively tracking anything but was rather being driven with the jitter signal as fast as possible. The success requirement was defined to be that a match to motion had been achieved to within ½ pixel within one timestep in the jitter sequence. In parallel with the motion testing, the CCD was confirmed to operate with the Leach controller. However, to allow operation of the CCD, a custom PCB and wiring harness was fabricated to provide clocking signals and DC voltages to the pixel electronics. Confirmation of performance was achieved by taking focused images with the CCD while at room temperature. The CCD was also mounted in the cryostat (without the hexapod) and cooled down to test both that the cryostat functioned properly under vacuum, and that the CCD performed nominally at an operational setpoint as low as -123 °C.

2.7.2 Phase I Methods

Both the hexapod and the XY stages were manufactured by the German company Physik Instrumente (PI) and are both OTS products. Therefore, the actuated stages come with their own controllers, software, and detailed specification sheets. The hexapod has provided software called "PI MikroMove", which is a Graphical User Interface (GUI) that allows the user to input positional movements, input velocity, carry out motion profiles, etc. However, since any error beyond a couple microns could be disastrous to the development process, it was important to check the positional accuracy of PI's software and cross-verify the stage operation using a different method. This method involved using a Position-Sensitive Diode (PSM) and laser setup.

In Phase II, the hexapod is integrated into a cryostat behind a glass view port, so it was decided early on to prepare for this orientation by mounting a retroreflector cube on the hexapod that reflects any optical input beam 180 degrees. Since the electronics of the laser and the PSM are not rated for vacuum or cryogenic temperatures, the retroreflector enables all the position-sensing electronics to function on the exterior of the cryostat by shining the laser through the view port, off the retroreflector, and then back to the PSM.

Three main tests were performed to authenticate the performance of the PI stages. 1) Positional accuracy test, 2) Velocity and acceleration test, and 3) Frequency test. The test requirements were driven by the requirements for the hexapod instrument, which were in turn driven by the need to correct for the well-characterized STO jitter signal. For the 1) Positional accuracy test, the requirement was that the stages must be able to perform a minimum incremental movement of 6.5 microns (half the width of a pixel on the e2v 47-10 CCD) with no hysteresis, for the 2) Velocity and acceleration test, the requirement was that the stages are able to at least match the maximum speed and acceleration of the STO jitter profile, and for the 3) Frequency test, the requirement was that the stages were able to perform movements at a rate of 30 Hz (characteristic of the harshest STO jitter profile).

Before carrying the verification tests out, it was important to both understand the vibrational environment of the laboratory, to understand any potential false readings, as well as characterizing the ability of the PSM itself. With the laboratory overhead lights on (harshest light pollution conditions), the PSM showed consistent accuracy of 1 micron (measured by plotting the noise level of an unmoving beam). After extensive testing the vibration isolation optics bench never showed a positional disturbance over 2 microns (well within the 6.5 micron limit). To aid with the optical setup for these tests, especially for the initial aligning of the laser / retroreflector / PSM system, a LabView GUI that charts the location of the laser beam across the surface of the PSM was written. The LabView GUI also records the position of the laser on the PSM at 300 Hz (ten times greater than the highest frequency sampled) to enable data analysis after testing. A view of this LabView interface is found in Figure 17.

During this time the operation of the e2v CCD was also verified. While the e2v 47-10 CCD is a mass-produced OTS product most advanced science-grade detectors cannot be considered ‘plug-and-play’ systems by any standard. Therefore, while the device itself was well-characterized by e2v before delivery, a method for readout and data collection had to be implemented. Therefore, a Leach Controller from ARC was used to control the CCD, command a shutter, and retrieve and record image data. However, to interface the Leach Controller electronics with the CCD, a custom wiring harness and interface PCB were designed and fabricated.

2.7.3 Phase I Results

After confirming that the CCD was successfully responding to light (Figure 18 shows the CCD attached to the hexapod in early testing), a shutter and fixed-focus lens were placed in front of the detector facing a lit imaging target and took successful focused images. The CCD was then mounted in the empty cryostat directly to the cold plate, using vacuum feedthrough wiring to provide CCD control and readout. A heater was also attached to the CCD mounting structure controlled by a Lakeshore 336 temperature controller. The cryostat chamber was then pumped down using a combination roughing / turbo pump setup and then the cold plate cooled down to -196 °C with liquid nitrogen while maintaining the CCD at -123 °C via the heater and temperature controller PID loop.

This test verified the operation of the CCD within the cryostat and at its lowest operating temperature. It also verified the ability of the Lakeshore 336 temperature controller for precise temperature control. Finally, it showed that the cryostat was capable of being pumped down to the correct pressure (~1 x 10^{-6} Torr) for cryogenic operations. Using the slope from the positional measurements of a 2mm displacement (as measured by the laser and PSM) the speed and acceleration of the stage can be calculated.

The laser and PSM were then used to confirm that the stages could achieve the manufacturer's velocity specification and move with a great enough acceleration to correct for the STO jitter signal. The following data was collected by commanding the hexapod to move 2mm (plots seen in Figure 19 Figure 20) while recording the movement of the laser beam across the PSM: Velocity = (0.6mm / 0.06sec) = 10mm/sec … Acceleration → (Vf-Vi)/t = a → (8.57mm/sec - 0)/0.07sec = 122 mm/sec^2. The same experiment was then conducted with the XY stages giving → 13 mm/s velocity and Velocity → 80 mm/s^2 acceleration. The manufacturer velocity measurements matched the provided specification sheets and since the required acceleration to account for typical STO jitter is approximately 11 mm/s^2, both the hexapod and XY stages were confirmed to be sufficiently agile.

As a final Phase I verification of the hexapod's ability, the hexapod was driven with a ten-second snippet of severe STO jitter with the goal of recreating it as accurately and as fast as possible. The hexapod was able to reproduce the exact shape of the signal in a period of 5 seconds, twice the speed of the originally recorded signal. This recreation of the signal by the hexapod was recorded by the laser and PSM and plotted on the same axes as the STO ten-second snippet in Figure 21. Note that the hexapod recreation of the signal was 'stretched' in the time domain to closely match the STO jitter snippet to demonstrate how well the hexapod was able to recreate the shape of the signal.

2.7.4 Phase II Overview

The first part of Phase II involved measuring the positional accuracy of the hexapod again, since it was now mounted inside the cryostat and wired with vacuum feed-through cabling. The CCD was also tested again since new wiring harnesses were introduced to feed it into the cryostat. Next, the hexapod and XY stages were setup to test the capabilities of the hexapod in a configuration similar to an actual balloon mission. On a mission, the hexapod will receive its pointing error data from a guide camera mounted to the telescope, either at the focal plane or co-mounted with the imaging system. Such a guide camera uses a bright star near the intended target to measure the pointing error of the gondola. The hexapod will then be commanded to move in the X and Y directions to counteract the pointing error measured.

The lab setup imitates the balloon guide camera system very closely, but instead of focusing on a bright star, the jitter data is simulated using the data from the STO mission to command and move the XY stages upon which a target is mounted. The position of the XY stage is sampled using the combination of laser, retroreflector, and PSM. The positional movements of the XY stages measured by the PSM are then sent to the hexapod (which is facing the XY stages), and the hexapod moves opposite of the signal to correct for it. For instance, if the XY stages moved 10 microns in their positive X-direction, the hexapod would correct by simultaneously moving 10 microns to its negative X-direction so that there is no apparent movement in the reference frame of the CCD.

Finally, there is also an imaging target mounted on the XY stage that the hexapod and CCD face, and while the XY stages and hexapod both move, the CCD is used to take rapid exposures of the target. The sequential CCD images of the target mounted on the XY stages were then compared to each other to make sure that the residual movement between frames met the requirement of being less than or equal to one pixel. It is worth noting that rapid sequential exposures were taken with the CCD since at room temperature (~25 °C), the CCD is saturated from thermal charge if an exposure is longer than approximately one second.

After all the separate components were proven to work as required, the project could move to Phase II. This meant mounting the hexapod and CCD inside the cryostat and recreating the position testing from Phase I.

2.7.5 Phase II Methods

The most significant part of Phase II was mounting and operating the PI Hexapod inside the cryostat. Originally the cryostat design called for the hexapod to be mounted directly to the cold plate with an insulative fiberglass buffer. In retrospect, while being a simple design, the hexapod and fiberglass mount would have over time transferred heat to the cold plate and reduced the hold time of the cryostat. Despite the fiberglass buffer the hexapod would also undoubtedly require a heating element at its base to stay above its 0 °C minimum operating temperature. However, in the end, the issue was forced, and the fiberglass mount that coupled the hexapod on top of the cold plate was thrown out.

Due to a CAD miscalculation, the bulk of the permanent connector and cabling coming out of the side of the hexapod was sticking out too far to be contained within the cryostat. To solve this issue, Tucson-based Universal Cryogenics was approached to design an adapter mount that was essentially a cylinder with a larger radius than the rest of the cryostat that would allow the hexapod cabling to fit in the chamber properly. Consequently, the thermal design was improved since the hexapod was moved from having a conductive path to the cold plate (held at -196 °C) to instead being heat-sunk to the exterior of the cryostat. The only disadvantage of this redesign is that since the hexapod was moved farther away from the cold plate, the thermal strapping that leads from the cold plate to the CCD mounting structure had to be lengthened by an approximate factor of two. The result of this lengthening caused the CCD to cool at a much slower rate than expected and not be able to achieve as low of a temperature as hoped (goal was <-70 °C, but only able to achieve -50 °C). However, not being able to cool the CCD as expected still fit within the requirements for the prototype, as the operating temp of -50 °C still brought the dark current down enough for sufficiently long exposures.

After successfully mounting the hexapod in the cryostat, the hexapod operation was verified once again with a 1) Positional accuracy test, 2) Velocity and acceleration test, and 3) Frequency test. The hexapod displayed no appreciable difference in performance from Phase I.

2.7.6 Phase II Results

The results from Phase II stemmed mostly from success of mounting and testing equipment inside of the cryostat. One concern was that the hexapod might be at risk of overheating inside of the cryostat after convection was removed during vacuum pump down. Therefore, to prove the robustness of the thermal scheme the hexapod was commanded through a continuous series of motions after the cryostat was held at

10^{-7} Torr. Figure 22 shows a plot of the temperature data from this test where the hexapod's hottest temperature leveled off at less than 40 °C which is ten degrees under the hexapod's highest specified operating temperature.

2.7.7 Phase III Overview

The final phase of prototype development was to perform a functional repeat of Phase II but with cryogenic cooling introduced. This was a challenge as there are many thermal variables at play inside of the cryostat. A one-liter tank at ambient pressure is filled with liquid nitrogen via an external pressurized dewar and latex fill hose. The liquid nitrogen tank in turn cools down the aluminum 'cold plate' inside of the cryostat to -196 °C. Several flexible copper straps mounted to the cold plate extend up and around four sides of the hexapod to touch and draw heat away from the CCD copper mounting structure. Therefore, during and after cooling the positional accuracy of the hexapod was verified yet again and the CCD was confirmed to be operating nominally.

The purpose of introducing cryogenic cooling into the system is to cool the science CCD to a level where thermally-generated charge (or dark current) is negligible, or at least can be managed. As mentioned in Phase II, when the CCD is operated at room temperature, the maximum exposure time is roughly one second due to saturation by thermally-generated charge. According to documentation the e2v 47-10 CCD cooled to -70 °C, an hour-long exposure theoretically yields ~300 thermally-generated electrons per pixel compared to $\sim 3 \times 10^7$ electrons per pixel at room temperature. Furthermore, when taking exposures of planetary targets, the expected exposure times are estimated to be in the 30-60 second range, which means that if the 47-10 CCD was held at -50 °C, the thermally-generated electrons per pixel would be negligible (<0.1).

The hexapod was then set up to receive XY positioning input from the PSM, where the XY stages move and the hexapod tracks based on the position of the laser on the PSM. The hexapod was measured to receive a position from the PSM and complete a corrective movement at a rate of ~100 Hz or once every 10 milliseconds. During motion testing, if the amplitude of consecutive signals was more than ~250 microns the hexapod would start the next motion before it was finished with the last, but there were no 10 millisecond departures in the jitter data larger than about ~5 microns. Images of the Phase III testing scheme can be found in Figure 23, and a functional block diagram of the laboratory test setup can be found in Figure 24.

2.7.8 Phase III Methods

As a final confirmation of the ability of the hexapod to correct jitter with a cryogenically-cooled detector in a flight-like configuration, the XY stages were setup to perform an STO jitter profile (taken from a snippet of the most severe jitter), and the hexapod was setup to track the XY stages. To accomplish this, the hexapod received XY positioning input from the PSM and laser, where the XY stages move and the hexapod tracks based on the position of the laser on the PSM. This is a comparable configuration to the hexapod receiving an error signal from a star tracker.

On the optics bench, an OTS focusable camera lens was placed in front of the cryostat window/shutter to focus light from the XY stage light sources onto the hexapod focal plane during exposures. The focal length of the system for these measurements was ~80cm. With these optical parameters, a 1 micron point-source Full-Width Half Max (FWHM) was sampled across three CCD pixels.

A 60 second integration time was chosen as a requirement since it is twice the expected ~30 second integration for imaging a bright planetary target from a suborbital balloon. As previously discussed, different image targets were mounted to the XY stages to test different aspects of the system, but for the purposes of the jitter correction experiment, a single dimly lit incandescent bulb was used. An adjustable camera lens was placed in front of the cryostat window and used to focus the image onto the focal plane. The advantage of using a light bulb filament as the imaging target, as opposed to a point source, is that image structure is readily apparent. For example, jitter during exposures might blur features such as a storm cloud tops on a gas giant, but with jitter removed, the structure of the clouds is resolved.

During data collection, first a 60 second exposure was taken while all of the stages were stationary to establish a baseline. Next, another 60 second exposure was taken while only the XY stages were moving, resulting in the image of the glowing filament being blurred by the motion. Finally, the experiment was repeated with the XY stages jittering while the hexapod corrected for the motion resulting in the structure from the stationary image being restored.

The hexapod was also stress tested to understand when the corrective abilities of the instrument start to fail. For this an illuminated point source was constructed from a laser, 1 micron pinhole, and a neutral density filter. This point source was then coupled to the XY stages for data collection. As mentioned, the illuminated 1 micron pinhole appeared as a PSF approximately 3 pixels FWHM across during imaging. 1D frequency testing was performed where the point source was moved back-and-forth 100 microns at 60 hz. Also, an amplified version of the STO jitter was produced (tripled the error signal) to see how to the hexapod would perform.

2.7.9 Phase III Results

To statistically verify that HERESY was correcting for jitter during the 60 second run, identical 1-D profiles were projected across the most point-like region of the illuminated filament structure. Figure 25 shows zoomed-in images of the filament during the three cases of operation of stationary, XY stages being driven with the jitter signal and the hexapod stationary, and finally with the hexapod actively correcting and clearly displays how HERESY's corrective motions were able to preserve the structure of the filament shape. The XY stages moving only case was a proof of concept to demonstrate how blurred a source becomes due to uncorrected jitter (Figure 26, Above), and then the stationary case and hexapod correcting case (Figure 26, Below) were comparatively used to characterize the ability of the instrument.

Figure 27 shows examples of data collected when the hexapod was stress tested and pushed to its corrective limits. (A) shows a case where a point source was attached to the XY stages and exercised in a 1D 100 micron back-and-forth pattern at 60 Hz. (B) shows a case where an amplified STO jitter signal was run (~25 Hz and up to 300 micron displacement).

The images in (A) and (B) were 30 sec exposures – 1) is stationary (Both A and B have identical stationary control images), 2) is XY stages only with the hexapod stationary, and 3) is the hexapod actively attempting to correct for the error signal.

In (A) 2) the image can clearly be seen to be bimodal in the profile graph, but the hexapod still manages to correct enough to reclaim the PSF gaussian in 3). However, in 3) there is still significant blurring leading to a vast decrease in peak signal from the stationary image 1) indicating a breakdown in hexapod abilities.

(B) shows a case of amplified STO jitter, where the signal was increased by a factor of two to achieve displacements of 50-300 microns at ~25 Hz. (B) 2) shows a significant blurring and a PSF peak intensity that is nearly cut in half from the original image. In 3) the hexapod attempted to correct and endured some blurring to its image but was able to restore the bulk of the original image as it encountered only ~15% reduction in peak intensity from the original PSF in 1).

2.8 Discussion

Figure 25 and Figure 26 demonstrate that HERESY was able to retain the structure of the object while the XY stages and hexapod were in motion. However, the peak pixel intensity was reduced indicating that some blur across pixels still occurred. It is also important to note that the above case was a snippet taken from a time of STO's most severe jitter, so it is reasonable to suggest that, while HERESY fulfilled its requirements, it could produce even higher quality images during calmer times of flight.

By the end of this project HERESY could be considered a 'working prototype' that could be much improved upon if funded for a balloon flight. In a professional flight configuration HERESY would have a dedicated computer with short cable lengths to maximize software command speed, a cryocooler system rather than expendable cryogen, and better thermal strapping design to get the science detector as cold as possible. The cryostat housing HERESY could also be far more compact since it would no longer have a need for a large liquid nitrogen holding tank. Figure 27 shows promise that even with a Windows OS (affordable, but not known for speed) and operating beyond its design limits, the hexapod still is able to make improvements to image quality.

2.9 Conclusion

The HERESY laboratory prototype was able to meet the high-level instrument requirements as proven by the verification and validation test bench setup in LASI. However, in hindsight, several tweaks to the engineering approach may have yielded better results.

If budget and time allowed, it would have been beneficial to have the copper thermal straps that move heat away from the CCD hexapod focal plane to the LN2 cold reservoir professionally manufactured. The CCD was only ever able to be cooled to -73 °C, but the target setpoint was -123 °C. This ended up not being a major issue for purposes of proving the overall functionality of HERESY, as it was more than enough cooling to accommodate long exposures with the science-grade CCD, but it was apparent that the copper straps and the method that was used to thermally link them to thermal conductive surfaces could be vastly improved.

Also, if more budget and time allowed, it would have been ideal to build a test bench with an actual telescope and star tracker to test HERESY in a configuration as close to a balloon mission as possible. This setup would help refine the hexapod motion code and how the code most efficiently interfaces with start tracker code. While the point source in the lab, XY stage (to simulate error signal), and laser/PSM (to simulate star tracker) were good validation tools, it seems clear that this would be a required demonstration before delivery of a payload for an actual balloon mission.

As a final thought, the true benefits of the ‘actuate the focal plane not the beam’ HERESY approach are apparent in that it is a very compact system that does not require additional optics to correct for pointing error. However, at least with the current state of the hexapod motion code, FSMs are still able to correct pointing error with a much higher frequency. Therefore, the HERESY design has a requirement that the balloon telescope gondola that it is mounted to must have a highly accurate pointing ability (<1”), which is a constraint that would allow HERESY to only be effectively flown on some of the best systems currently available. Future iterations of this instrument will utilize FPGA to ensure the stages are driven as quickly as possible.

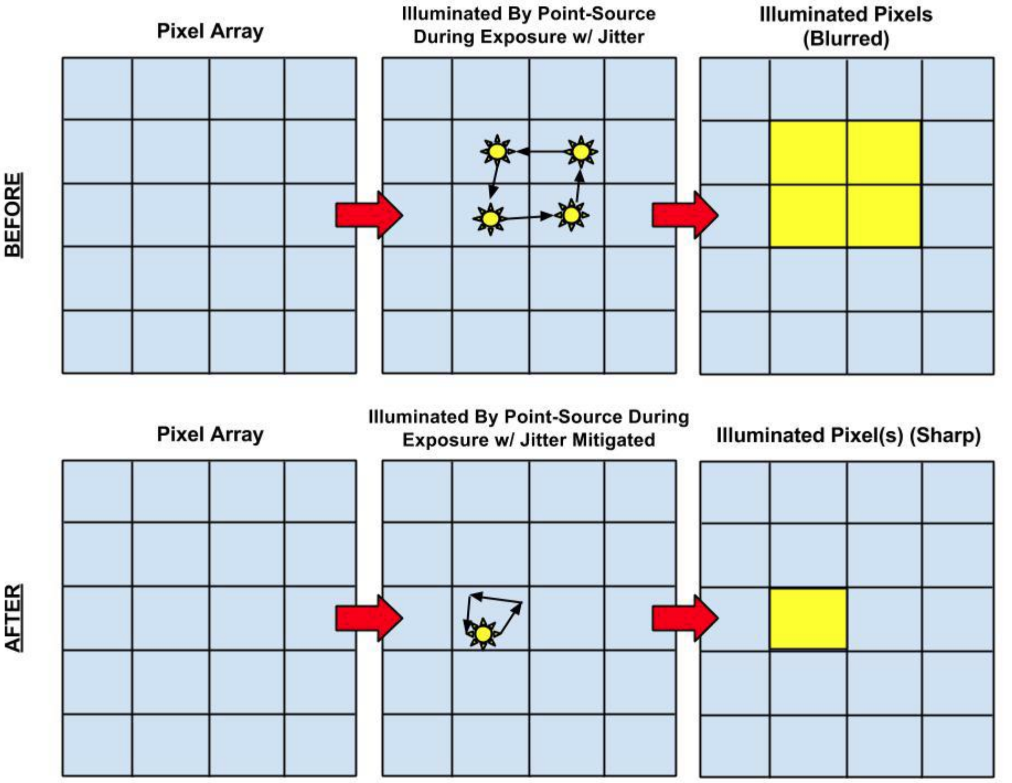

Figure 1. Jitter Elimination Concept

This graphic illustrates the need for technology that eliminates balloon jitter. The top array demonstrates how light is blurred across pixels during an exposure due to uncorrected jitter. In this example, a point source that should have only illuminated one pixel shows up spread out over four instead. The bottom array demonstrates an ideal situation where the hexapod corrected the jitter enough to contain the point source within a single pixel during the same exposure.

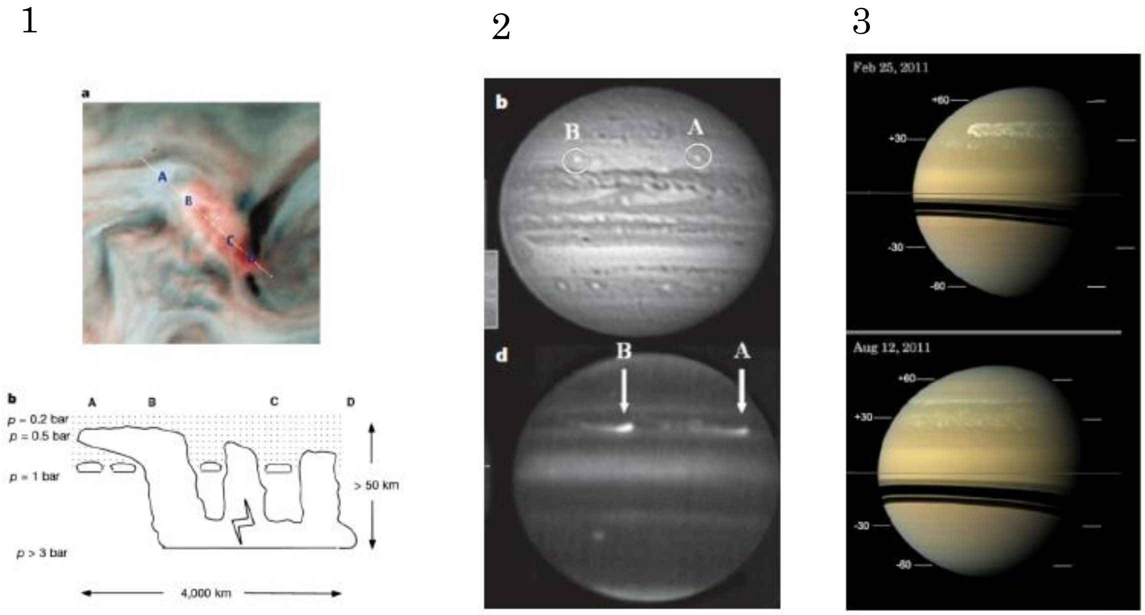

Figure 2. Giant Planet Cloud Structure and Heat Sources

1) Taken from (Gierasch et al., 2000), this shows a cross-sectional diagram of a storm system on Jupiter. 2) Taken from (Lagarreta et al., 2008) is an example of a superstorm eruption on Jupiter – a rare occurrence, but if captured by HERESY, could help better characterize giant planet heat transport. 3) Taken from (Sayanagi et al., 2013) shows a superstorm on Saturn captured by the Cassini spacecraft. Superstorms of this size have a comparable total power to the entire planet's full internal heat source.

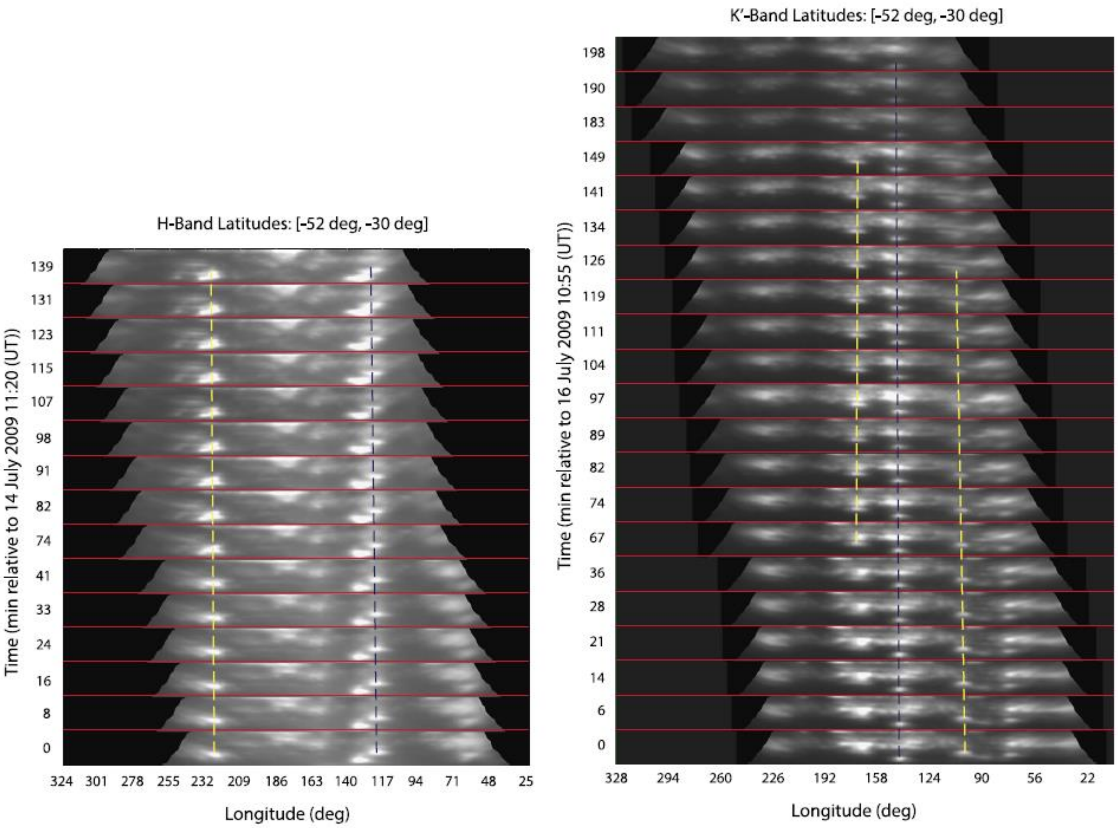

Figure 3. Time-Domain Discrete Storm Tracking

This figure is taken from (Fitzpatrick et al., 2014) and displays a series of time domain observations of discrete storm systems on Neptune taken from the Keck II telescope. Over a period of approximately 2.5 hours, Neptunian storm evolution and dissipation was captured. HERESY aboard an LDB would be able to collect similar data but at longer timescales.

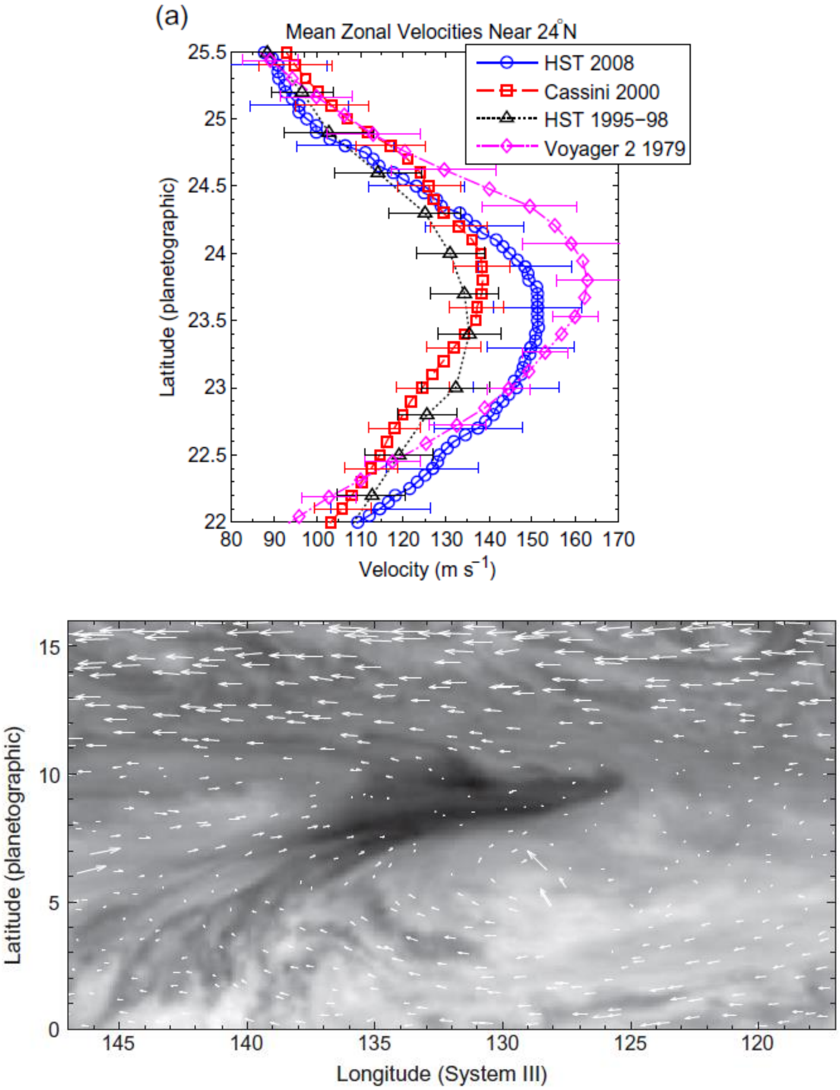

Figure 4. Jupiter Zonal Velocities

These figures are taken from (Asay-Davis et al., 2011) and show an analysis of zonal velocities for certain areas of Jupiter. The above plot shows how zonal velocities at particular spatial coordinates have changed over time. The below image shows a storm feature on Jupiter known as a ‘dark projection’ with overlaid wind vectors to graphically display circulation directions and speed.

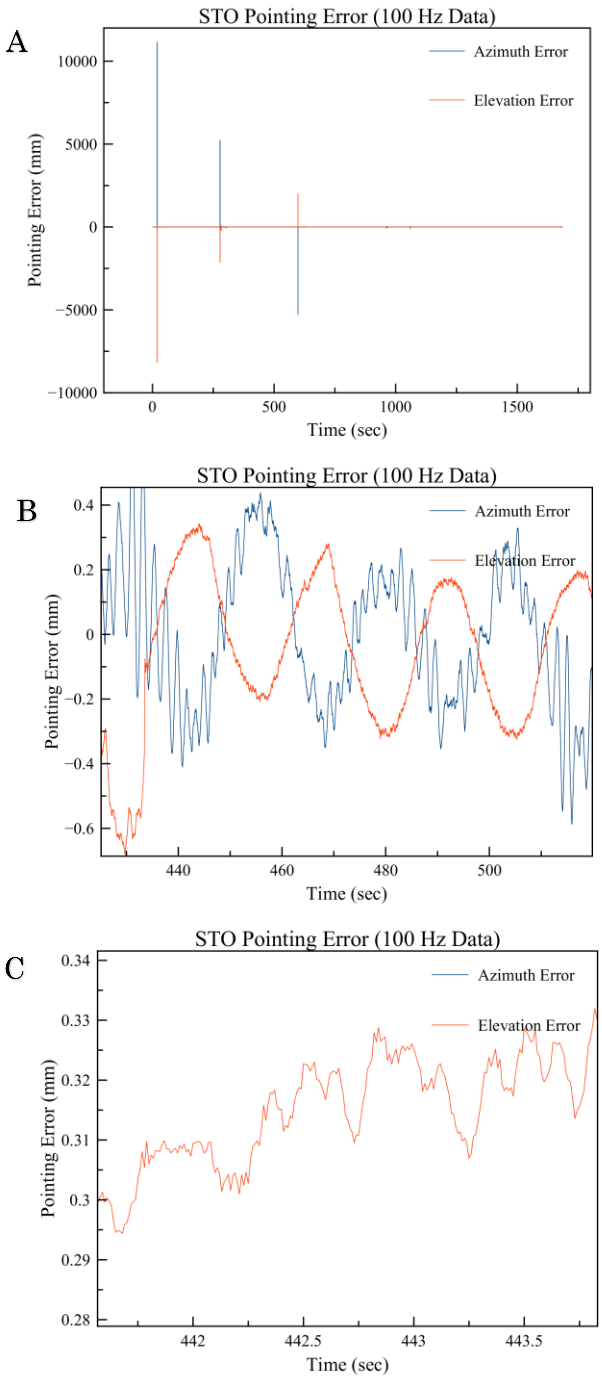

Figure 5. STO Mission Jitter

This series of plots shows the pointing error due to jitter recorded during the STO balloon mission. A) is the entire STO data set (the large jumps in error are due to the telescope repositioning to different targets), B) is a zoom-in to demonstrate what the typical STO error profile typically looks like, C) is an extreme zoom-in to show a period of particularly adverse jitter, which was used to define the requirements for the balloon-based version of HERESY.

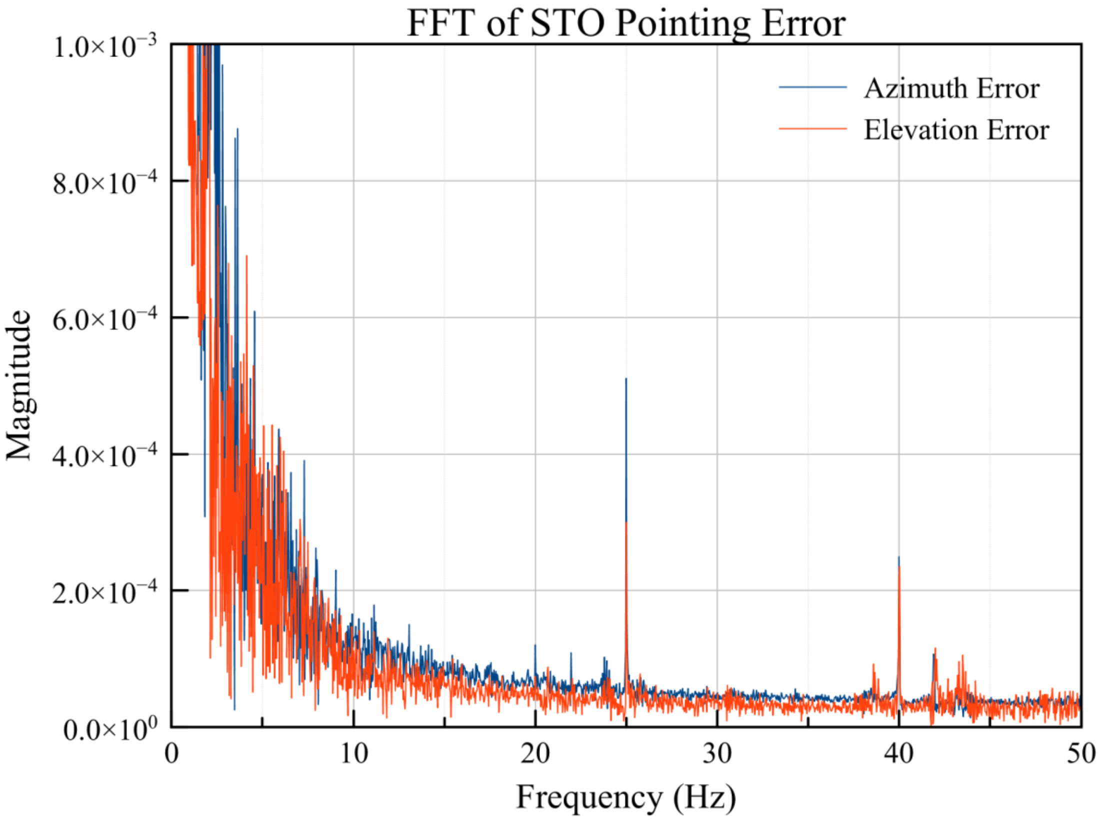

Figure 6. STO Pointing Error Power Spectrum

This plot displays the power density spectrum of pointing error introduced by jitter during the STO mission. There is a significant peak around 25 Hz.

Table 1. HERESY Science Traceability for a Planetary Balloon Mission

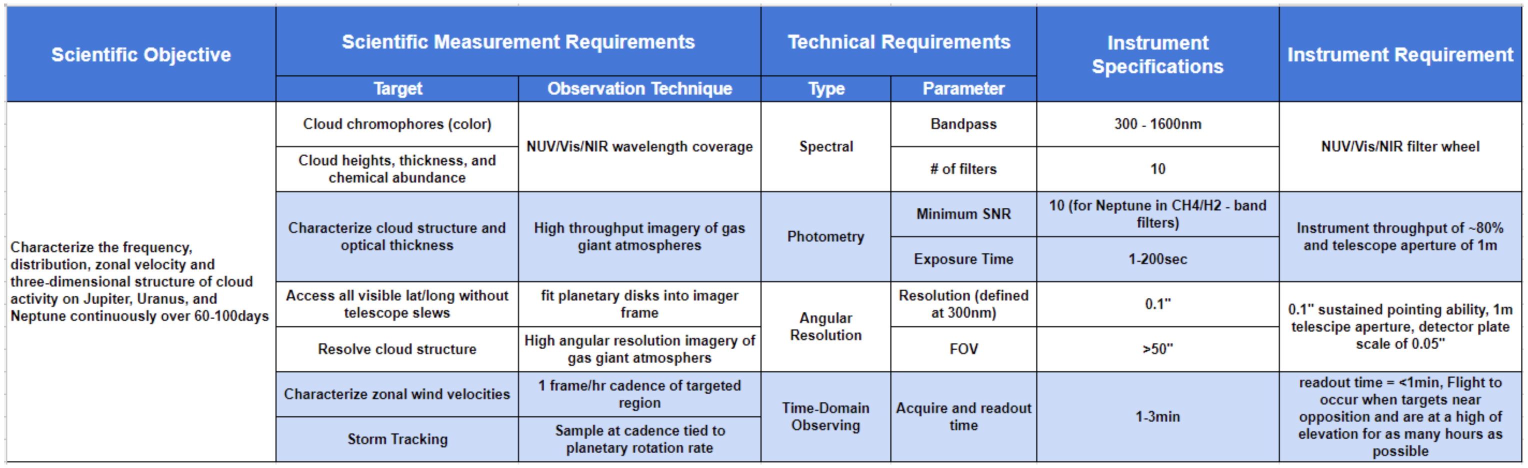

Scientific Objective	Scientific Measurement Requirements		Technical Requirements		Instrument Specifications	Instrument Requirement
	Target	Observation Technique	Type	Parameter		
Characterize the frequency, distribution, zonal velocity and three-dimensional structure of cloud activity on Jupiter, Uranus, and Neptune continuously over 60-100days	Cloud chromophores (color)	NUV/Vis/NIR wavelength coverage	Spectral	Bandpass	300 - 1600nm	NUV/Vis/NIR filter wheel
	Cloud heights, thickness, and chemical abundance			# of filters	10	
	Characterize cloud structure and optical thickness	High throughput imagery of gas giant atmospheres	Photometry	Minimum SNR	10 (for Neptune in CH4/H2 - band filters)	Instrument throughput of ~80% and telescope aperture of 1m
				Exposure Time	1-200sec	
	Access all visible lat/long without telescope slews	fit planetary disks into imager frame	Angular Resolution	Resolution (defined at 300nm)	0.1"	0.1" sustained pointing ability, 1m telescipe aperture, detector plate scale of 0.05"
	Resolve cloud structure	High angular resolution imagery of gas giant atmosphers		FOV	>50"	
	Characterize zonal wind velocities	1 frame/hr cadence of targeted region	Time-Domain Observing	Acquire and readout time	1-3min	readout time = <1min, Flight to occur when targets near opposition and are at a high of elevation for as many hours as possible
	Storm Tracking	Sample at cadence tied to planetary rotation rate				

This table breaks down the HERESY balloon planetary science objective into a series of targeted measurements. These are further described and flowed down into instrument requirements.

Table 2. Targeted Cloud Feature Sizes on Outer Planets from Scowen 2014

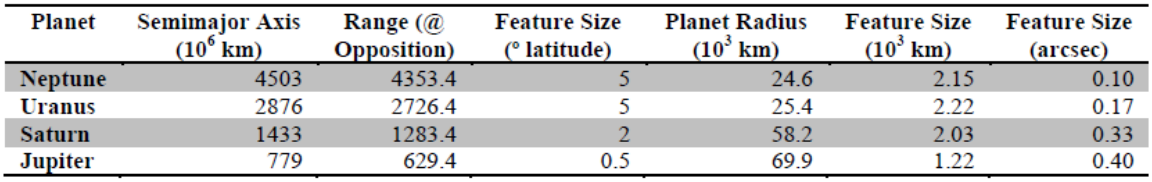

Planet	Semimajor Axis (10^6 km)	Range (@ Opposition)	Feature Size (° latitude)	Planet Radius (10^3 km)	Feature Size (10^3 km)	Feature Size (arcsec)
Neptune	4503	4353.4	5	24.6	2.15	0.10
Uranus	2876	2726.4	5	25.4	2.22	0.17
Saturn	1433	1283.4	2	58.2	2.03	0.33
Jupiter	779	629.4	0.5	69.9	1.22	0.40

This table assumes gas giant range at opposition – worst case observing scenario for storm angular sizes – and describes the required minimum resolution to image cloud features on each planet. The angular size of features on Neptune at opposition are at the limit of what the HERESY instrument was designed to resolve.

Table 3. Maximum Exposure Times from Scowen 2014

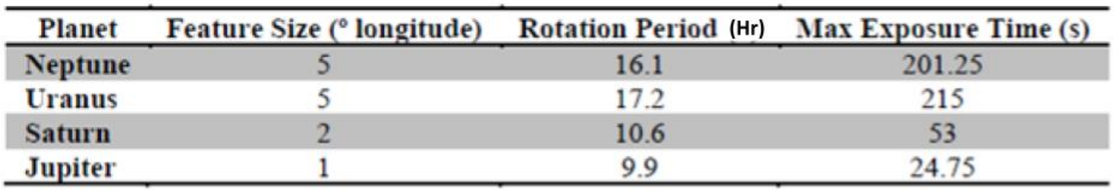

Planet	Feature Size (° longitude)	Rotation Period (Hr)	Max Exposure Time (s)
Neptune	5	16.1	201.25
Uranus	5	17.2	215
Saturn	2	10.6	53
Jupiter	1	9.9	24.75

Calculated maximum exposure times for the HERESY CCD when imaging gas giants from a balloon platform.

Table 4. HERESY Proposed Filter Set from Scowen 2014

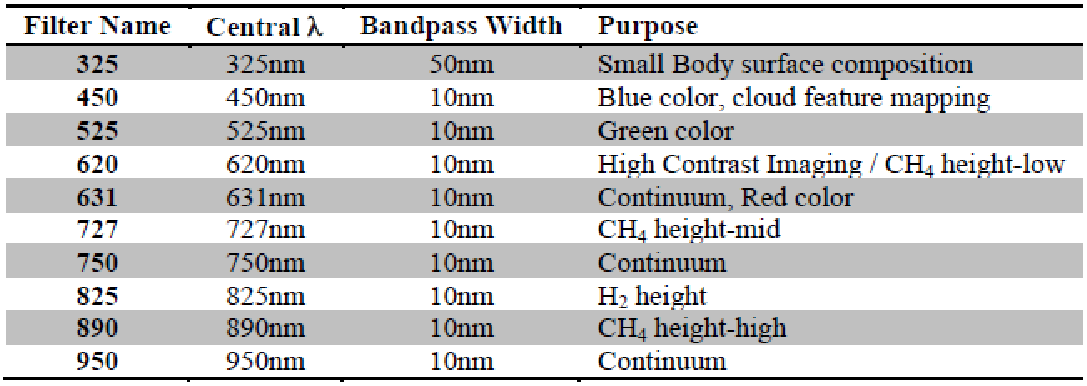

Filter Name	Central λ	Bandpass Width	Purpose
325	325nm	50nm	Small Body surface composition
450	450nm	10nm	Blue color, cloud feature mapping
525	525nm	10nm	Green color
620	620nm	10nm	High Contrast Imaging / CH_4 height-low
631	631nm	10nm	Continuum, Red color
727	727nm	10nm	CH_4 height-mid
750	750nm	10nm	Continuum
825	825nm	10nm	H_2 height
890	890nm	10nm	CH_4 height-high
950	950nm	10nm	Continuum

The filters span the near-UV to near-IR and feature filters strategically chosen to target certain aspects of gas giant cloud layers. The vertical structure of discrete storms can be determined by using a series of methane absorption narrow-band filters (Gierasch et al. 2000). This same technique was used by the Galileo and Cassini spacecrafts to image both Jupiter and Saturn's cloud features. Several continuum filters will be used as a baseline for interpreting cloud reflectivity and to remove any false interpretations caused by cloud chromophore effects.

Table 5. HERESY High-Level Engineering Requirements

#	Flow-Down from Science Technical Requirements	High-Level Engineering Requirement	Rationale	Verification
1	Angular resolution of 0.1" sustained pointing ability (must remove jitter signal)	Actuated stage must exceed or match speed and frequency of jitter	Functional Requirement	Demonstration
		The actuated stage must be able to move in increments smaller than 1 pixel width of chosen science detector	Functional Requirement	Demonstration
2	Detector SNR of 10 and accomodating up to 200sec exposure time (minimize dectector dark current)	Actuated stage must operate nominally in a cryogenic environment	Instrument Test	Test
		The detector must be able to be cooled while being moved by the actuated stage	Functional Requirement	Test
3	instrument throughput of ~80%	The detector shall be representative of a science-grade flight detector with QE of >80% across the NUV/Vis/NIR range	Instrument Test	Analysis
4	Detector readout time of <1min (time-domain observing)	The detector readout electronics shall readout each image and start the next exposure in <60sec	Functional Requirement	Demonstration

High-level engineering requirements for HERESY that are flowed from the Science Traceability Matrix.

Figure 7. The PI H811-V Vacuum-Rated Hexapod

The hexapod shown with Chapstick for size comparison, and the hexapod shown with a corner cube mounted to it during position confirmation using the laser and PSM.

Table 6. PI H811-V Hexapod Specifications (Physik Instrumente)

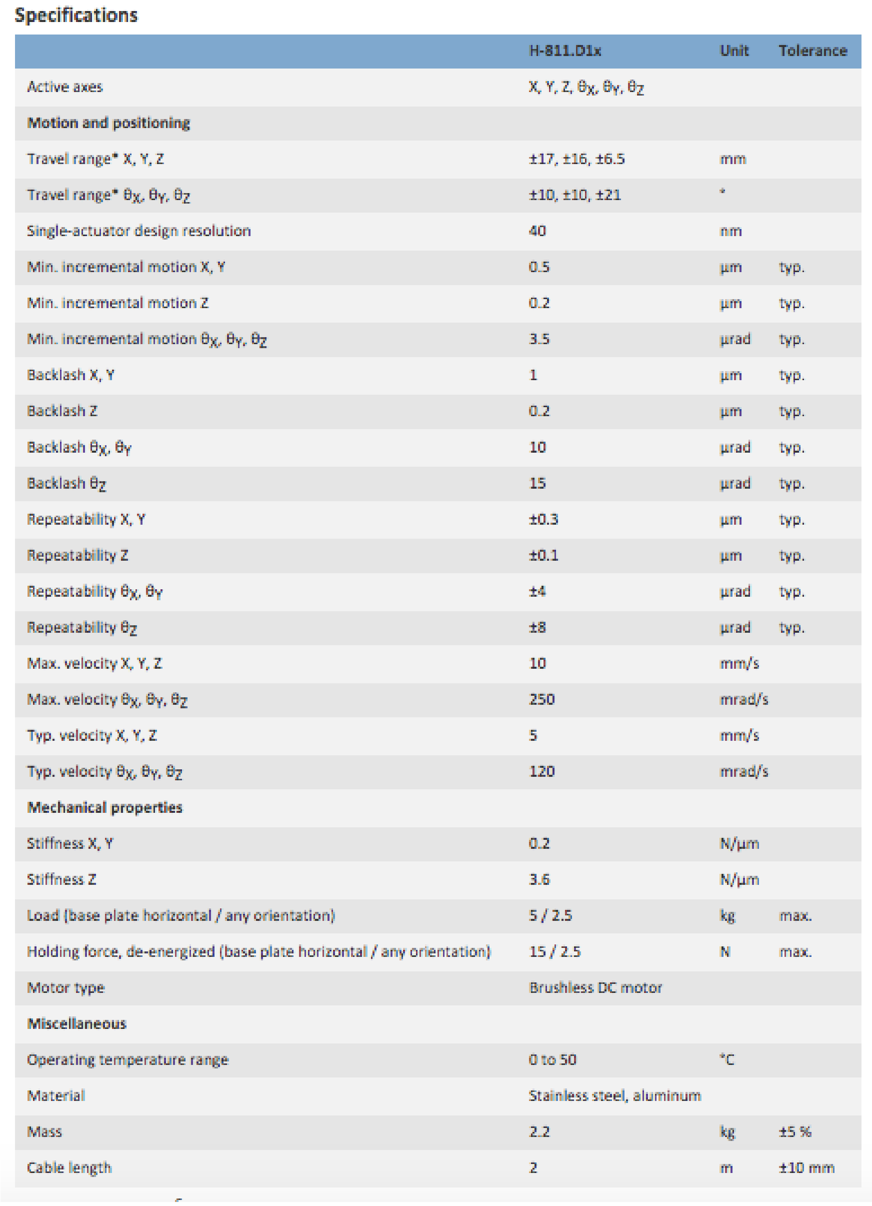

Specifications

	H-811.D1x	Unit	Tolerance
Active axes	X, Y, Z, θ_X, θ_Y, θ_Z		
Motion and positioning			
Travel range* X, Y, Z	±17, ±16, ±6.5	mm	
Travel range* θ_X, θ_Y, θ_Z	±10, ±10, ±21	°	
Single-actuator design resolution	40	nm	
Min. incremental motion X, Y	0.5	µm	typ.
Min. incremental motion Z	0.2	µm	typ.
Min. incremental motion θ_X, θ_Y, θ_Z	3.5	µrad	typ.
Backlash X, Y	1	µm	typ.
Backlash Z	0.2	µm	typ.
Backlash θ_X, θ_Y	10	µrad	typ.
Backlash θ_Z	15	µrad	typ.
Repeatability X, Y	±0.3	µm	typ.
Repeatability Z	±0.1	µm	typ.
Repeatability θ_X, θ_Y	±4	µrad	typ.
Repeatability θ_Z	±8	µrad	typ.
Max. velocity X, Y, Z	10	mm/s	
Max. velocity θ_X, θ_Y, θ_Z	250	mrad/s	
Typ. velocity X, Y, Z	5	mm/s	
Typ. velocity θ_X, θ_Y, θ_Z	120	mrad/s	
Mechanical properties			
Stiffness X, Y	0.2	N/µm	
Stiffness Z	3.6	N/µm	
Load (base plate horizontal / any orientation)	5 / 2.5	kg	max.
Holding force, de-energized (base plate horizontal / any orientation)	15 / 2.5	N	max.
Motor type	Brushless DC motor		
Miscellaneous			
Operating temperature range	0 to 50	°C	
Material	Stainless steel, aluminum		
Mass	2.2	kg	±5 %
Cable length	2	m	±10 mm

The hexapod was selected due to its large throw, positional accuracy, repeatability, and speed. It was also vacuum-rated OTS. However, the focal plane attached to the hexapod's face is cryogenically cooled which drives a creative thermal design to keep the instrument above its zero degrees lower operating limit.

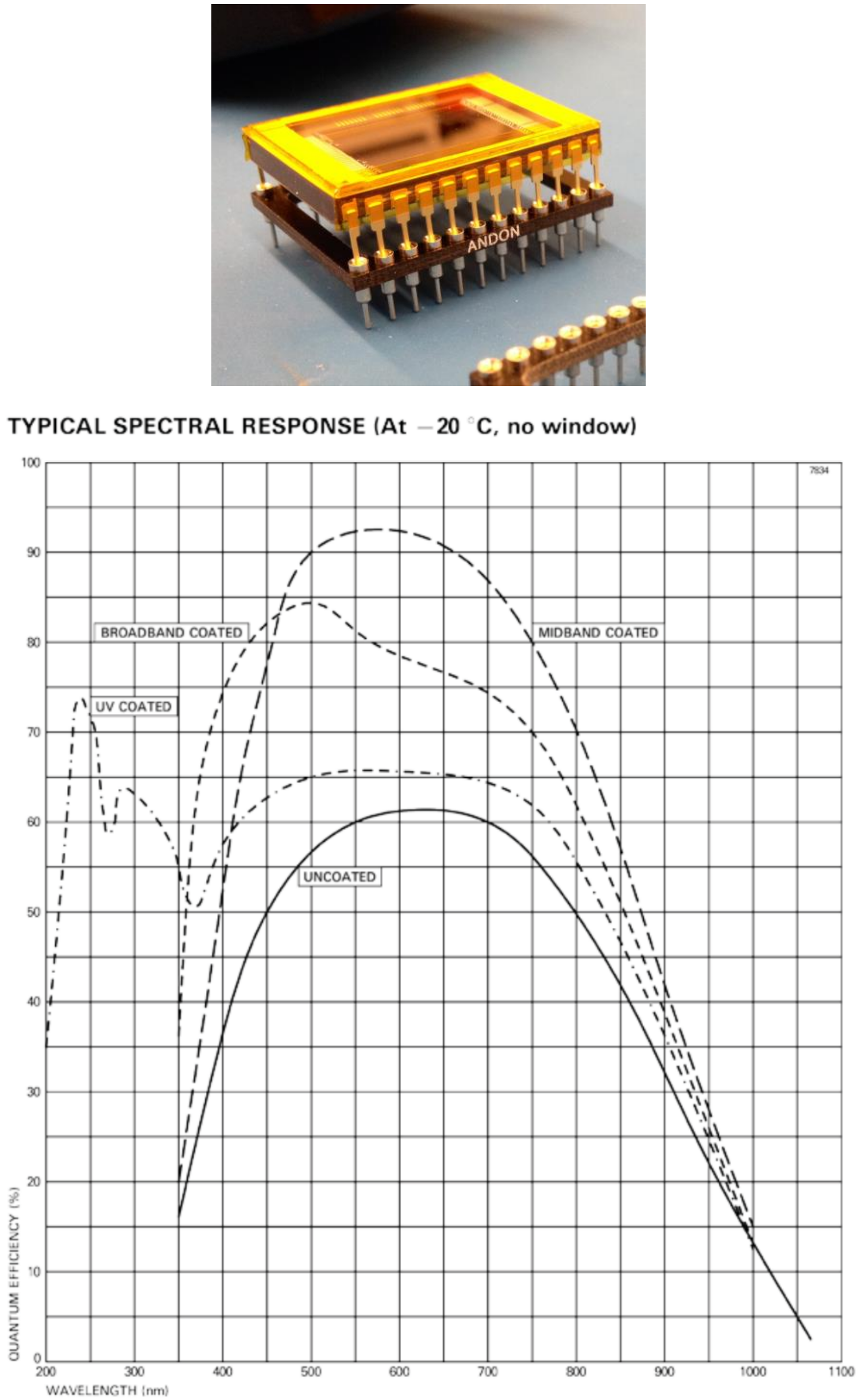

Figure 8. e2v 47-10 AIMO CCD and custom interface PCB

The packaged CCD from e2v (Above), and QE of the e2v 47-10 device (Below). (https://www.teledyne-e2v.com/)

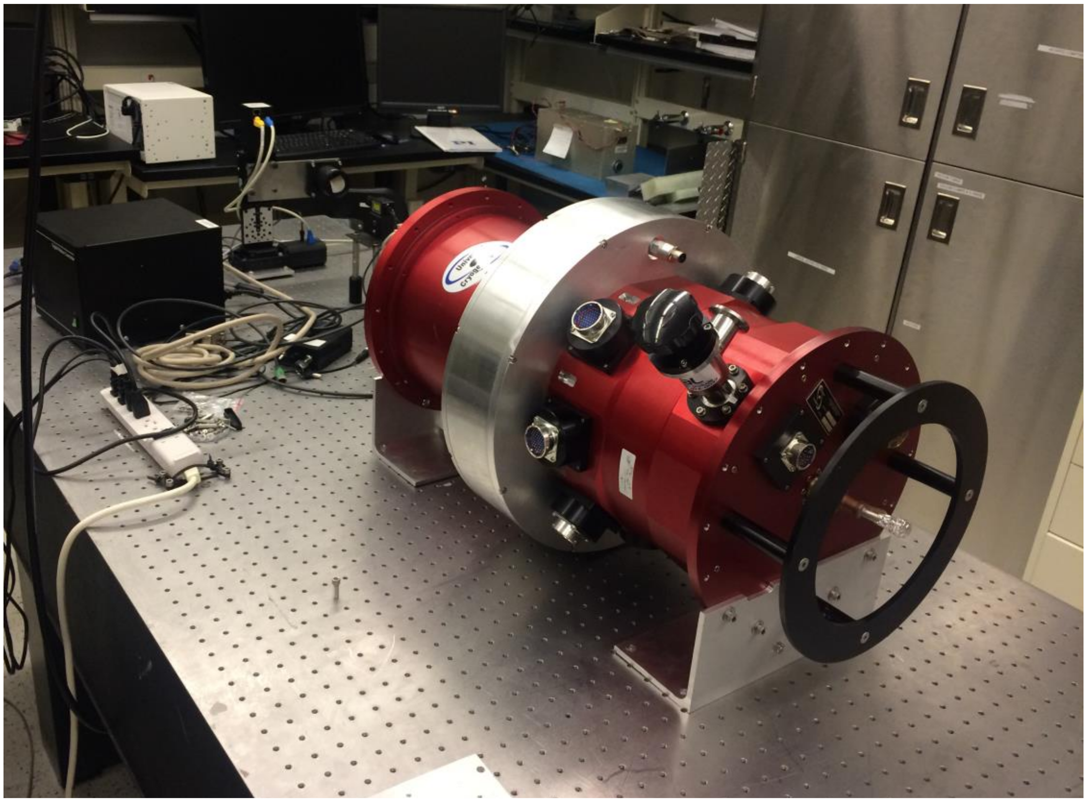

Figure 9. Cryostat Mounted to Optics Bench

Aluminum L-brackets were designed and implemented to allow the cryostat to mounted orthogonally on the optics bench for testing.

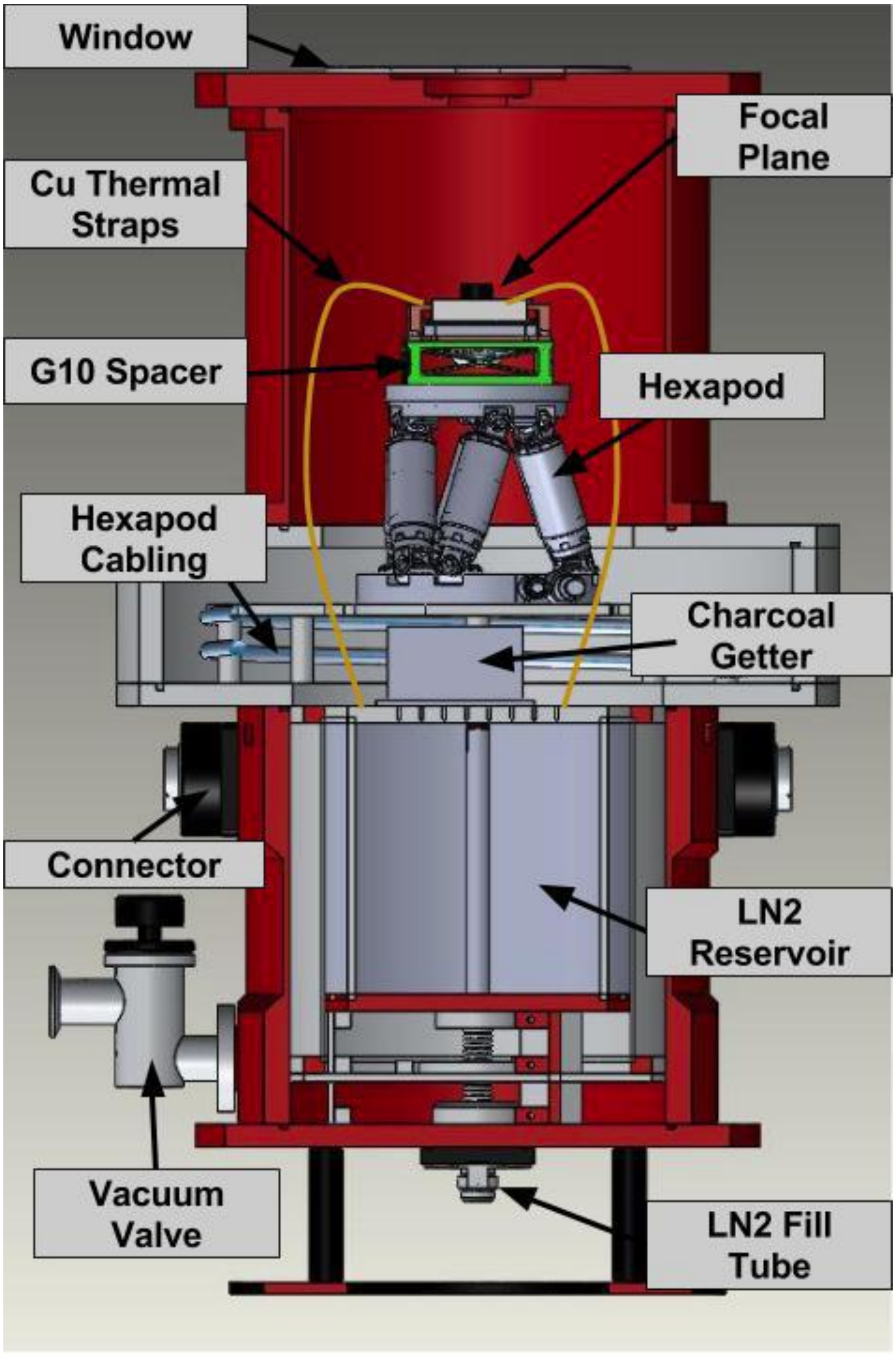

Figure 10. Cryostat Infographic

This image details the cryostat design for holding the hexapod focal plane under vacuum and cryogenically cooling the CCD while at the same time keeping the hexapod at near room temperature.

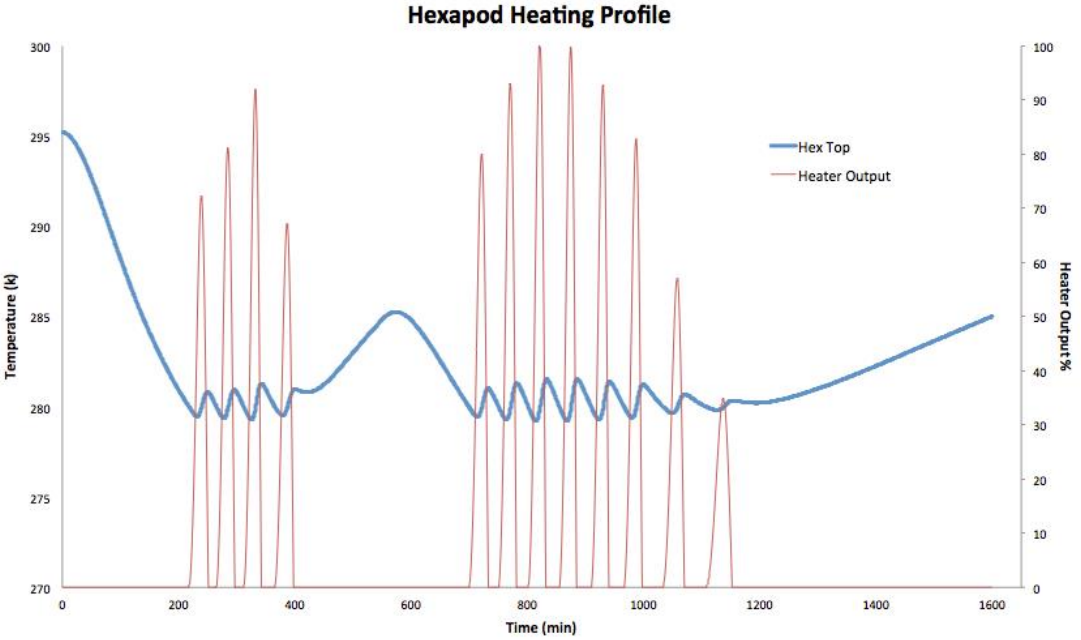

Figure 11. Hexapod Heater Duty Cycle

Over time the cooled CCD slowly pulled heat away from the top of the hexapod forming a thermal gradient across the instrument. There was concern that if this gradient became too severe, that it could affect instrument performance. Therefore, a heater was placed at the hexapod top mounting surface with a duty cycle to keep the surface at a setpoint of ~7°C (280k). The hexapod's coldest specified operating temperature is 0°C.

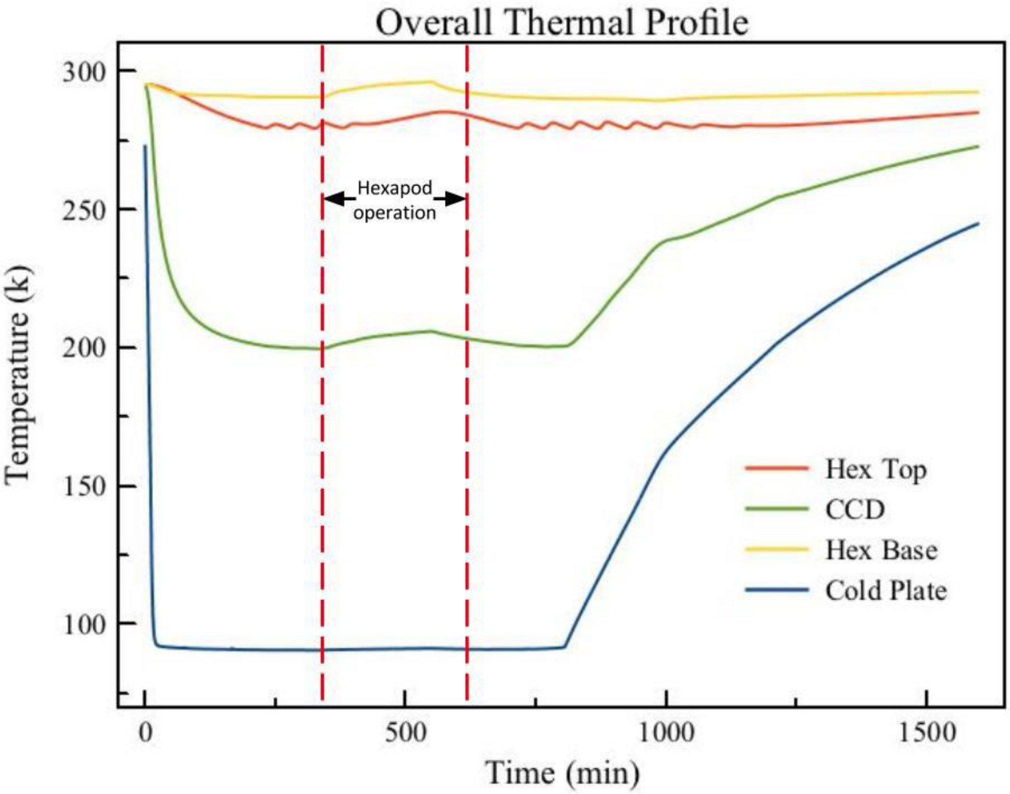

Figure 12. Overall Thermal Profile of HERESY During Operation

The CCD was held at 200 k with liquid nitrogen while at the same time the hexapod operates at near room temperature. There is a slight rise in CCD temperature during extended hexapod operations, but the associated rise in dark current is negligible.

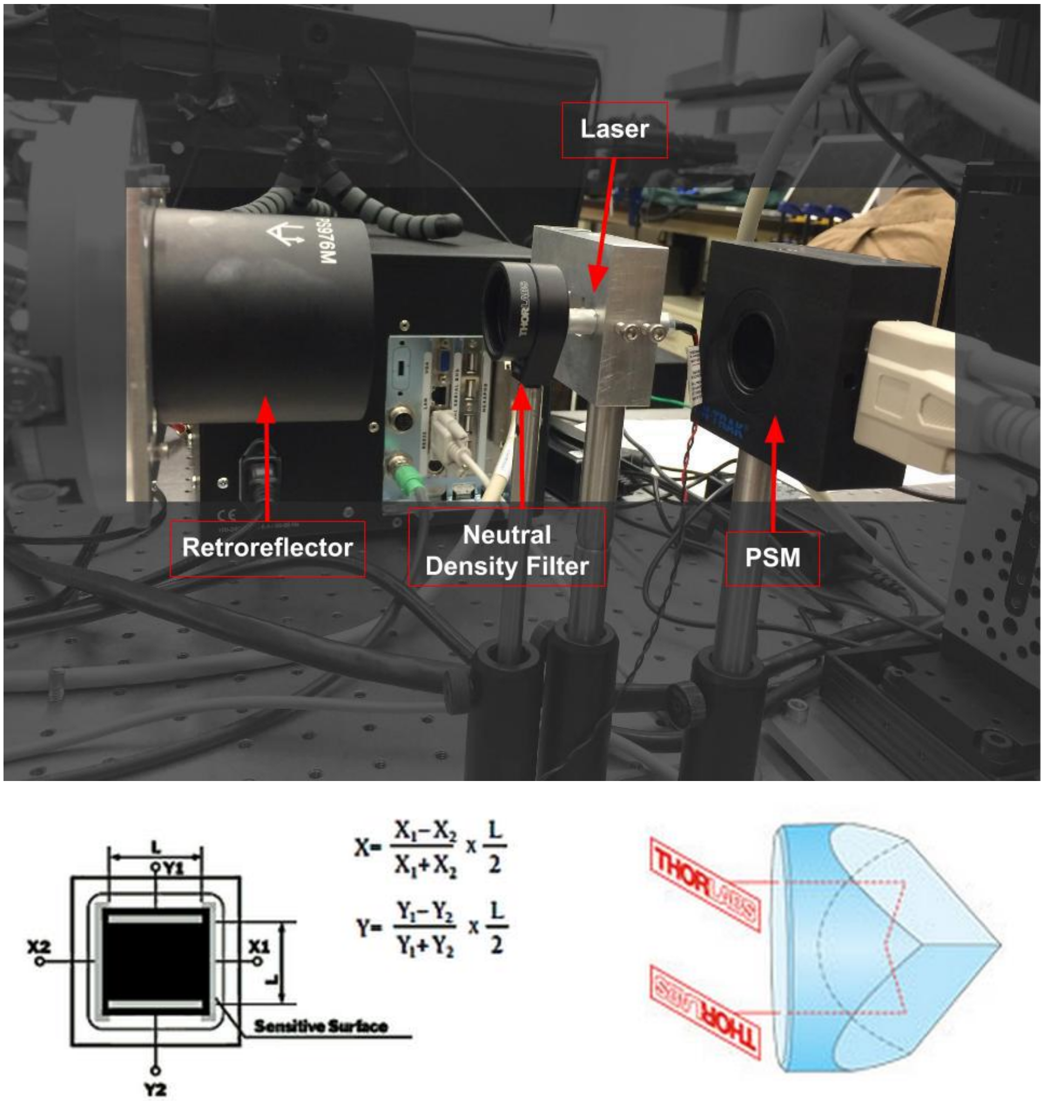

$$X = \frac{X_1 - X_2}{X_1 + X_2} \times \frac{L}{2}$$

$$Y = \frac{Y_1 - Y_2}{Y_1 + Y_2} \times \frac{L}{2}$$

Figure 13. PSM Position Verification Test Setup

This test setup was used to verify the positional accuracy and speed of the hexapod and XY stages. It was also used to track the movement of the XY stages, create an error signal, and send the associated information to the hexapod controller to command corrective movements. A neutral density filter was required to dim the laser before it reached the PSM to avoid oversaturation.

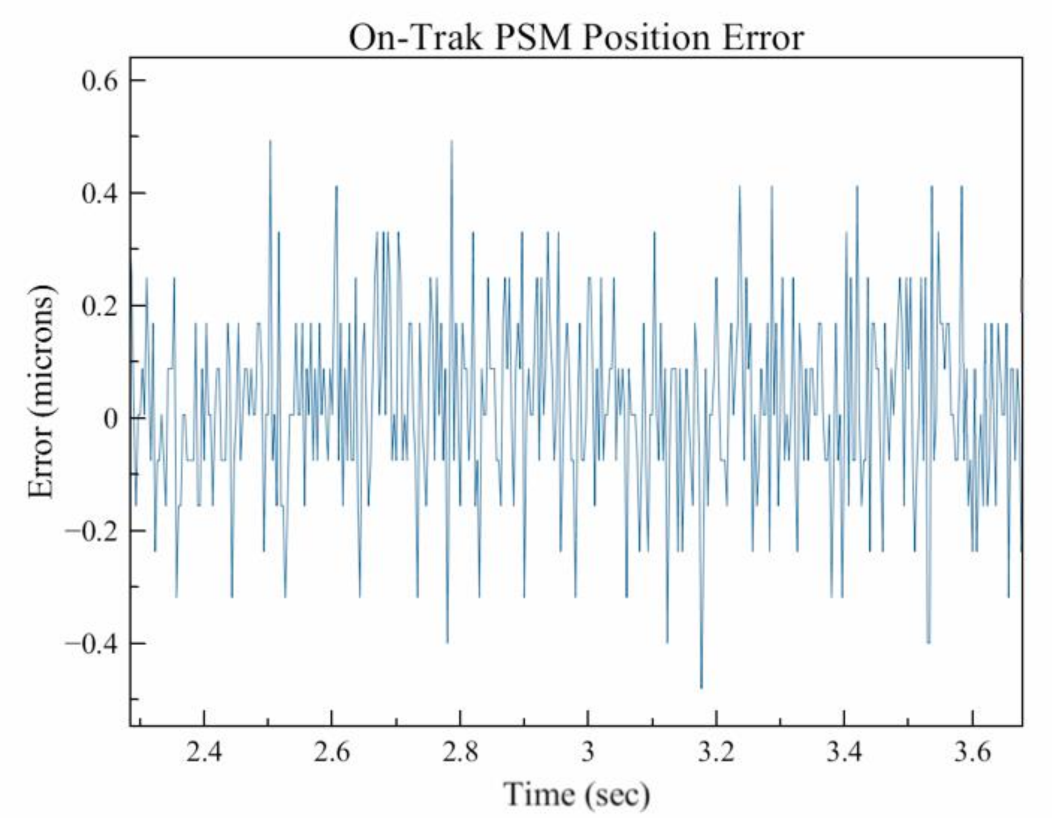

Figure 14. Minimum PSM Resolution Due to Noise

This plot is of the PSM signal with the laser beam focused on it and stationary. This demonstrates the random noise generated by the PSM constrains the positional accuracy of the unit to +/- 0.2 microns.

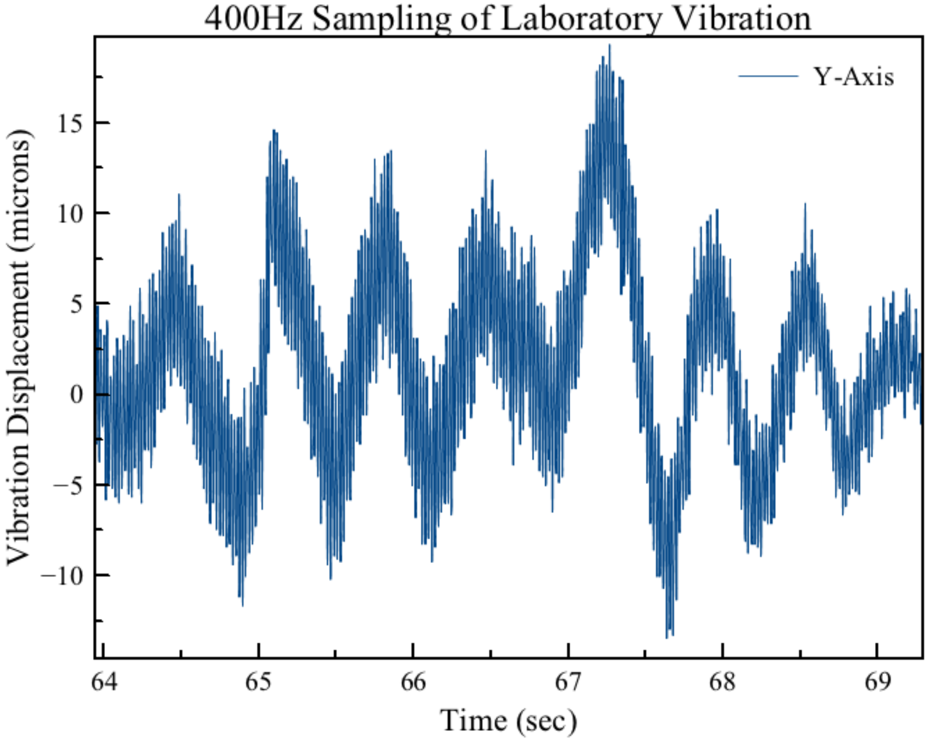

Figure 15. 400Hz Characterization of Laboratory Vibration

This, plot taken with the laser and PSM, shows vibration imparted into the lab environment by activities in the surrounding building (elevators, A/C units, etc.) which could affect the HERESY test setup.

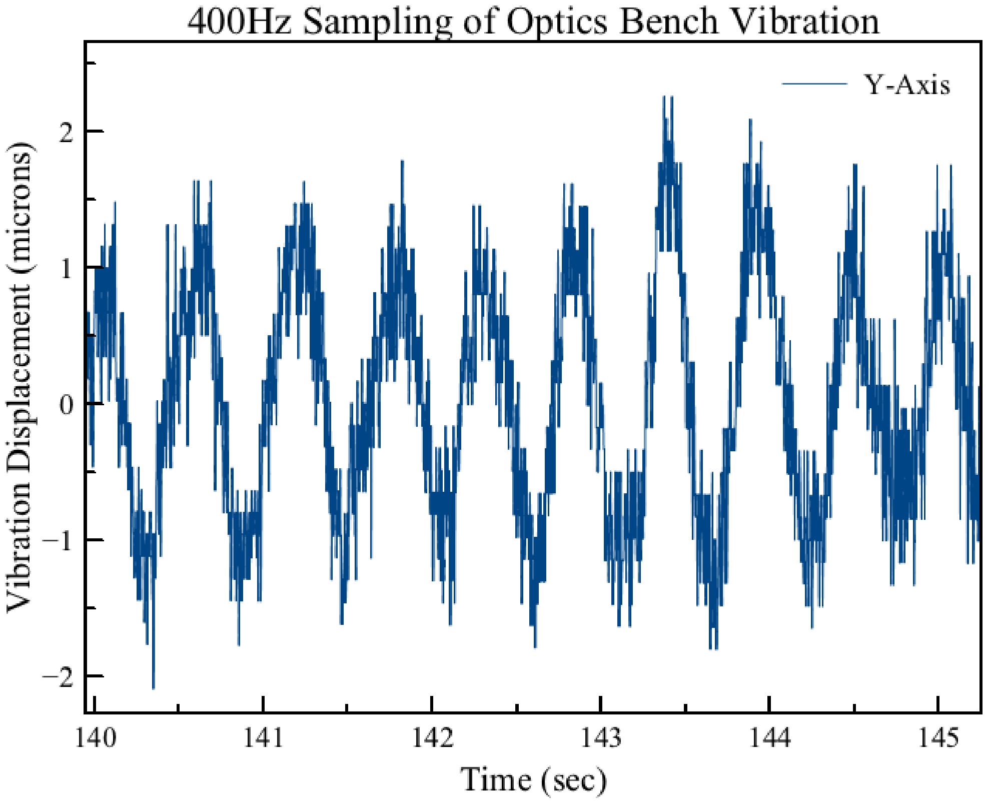

Figure 16. Optics Test Bench Dampened Vibration

This is a plot demonstrates a removal of laboratory environment vibrations (as compared to Figure 15). The max vibration imparted into the test setup after dampening by the optics bench is a low-frequency +/- 1 micron signal.

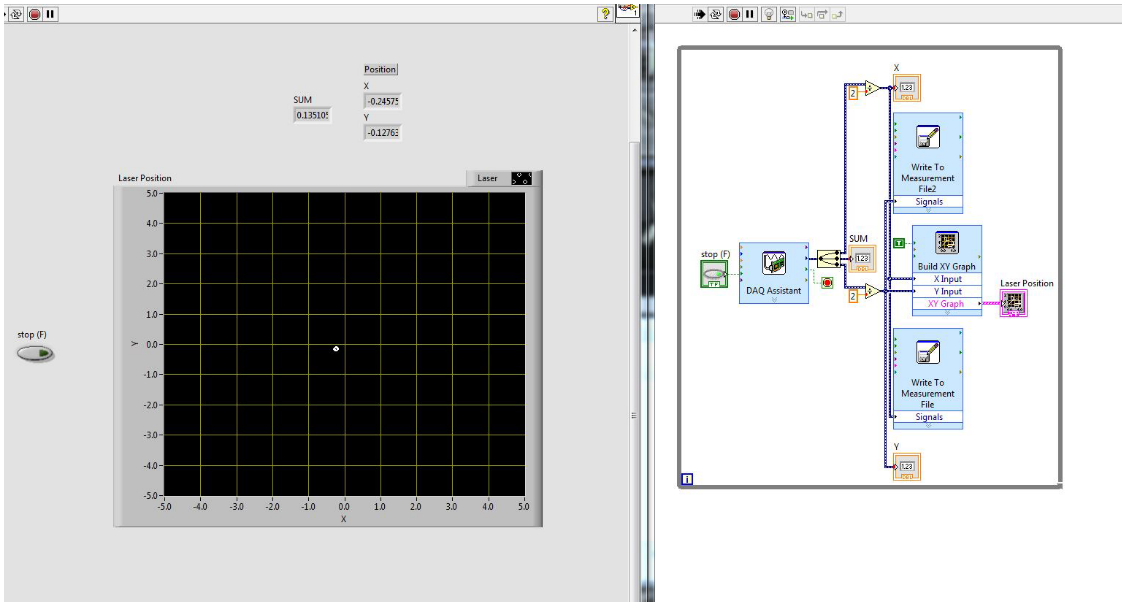

Figure 17. Custom PSM LabView Sampling Interface

This shows a LabView interface that was used to align the laser and PSM and also used to fast sample the laser position during movement tests. The XY plot on the left shows the physical position of the laser in real time across the PSM.

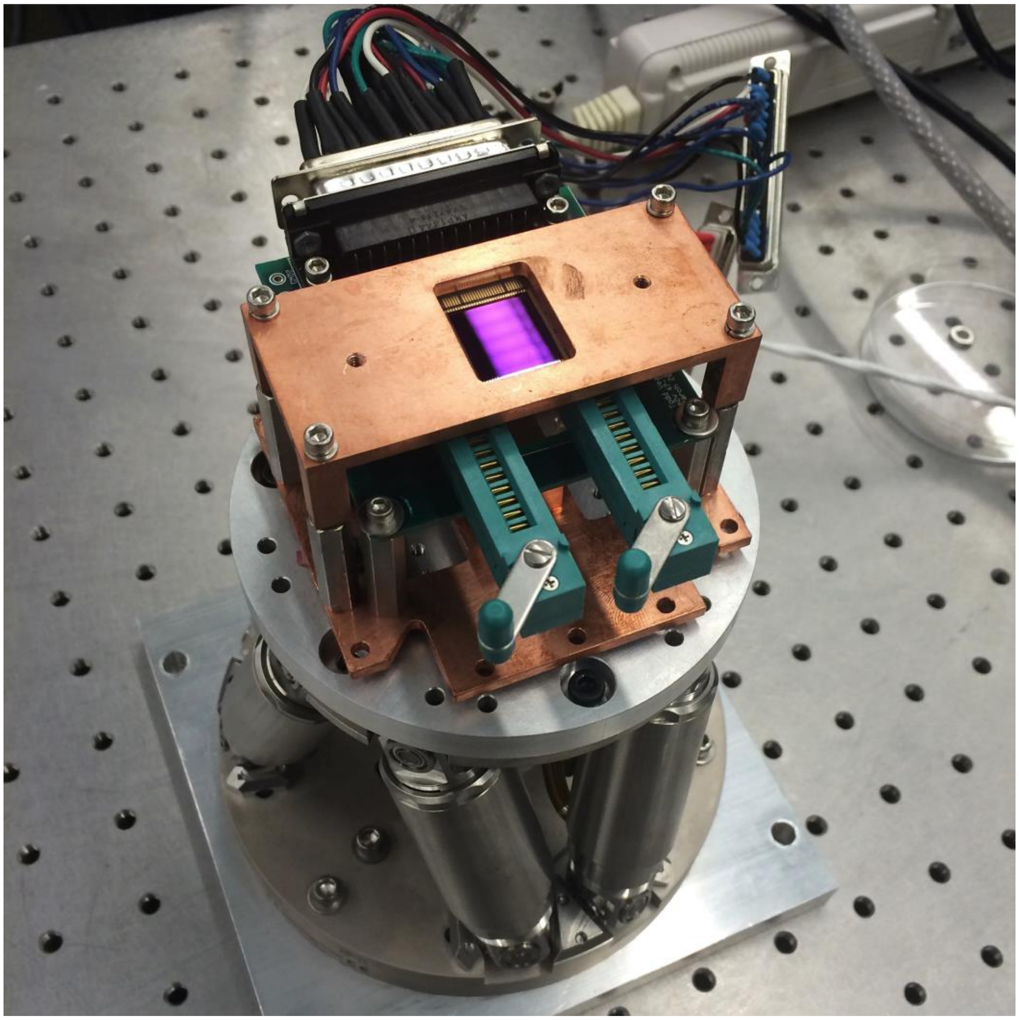

Figure 18. Hexapod with CCD Mounted

In early testing of the hexapod focal plane Zero Insertion Force (ZIF) sockets were used to easily ad safely mount and unmount the CCD from the hexapod.

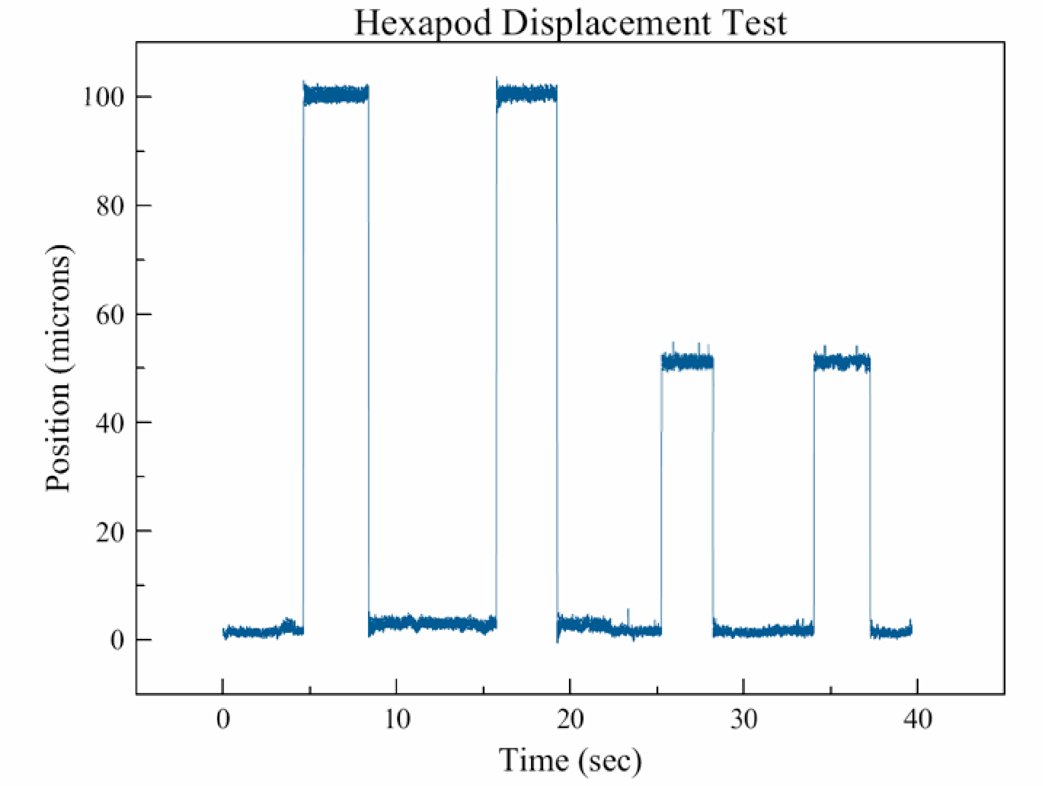

Figure 19. Hexapod Precision Displacement Test

The hexapod was measured by the laser beam projected across the PSM as it was commanded to move. This figure shows a test where the hexapod was commanded through a series of 100 micron movements and 50 micron movements. These position confirmation tests were repeated for the XY stages.

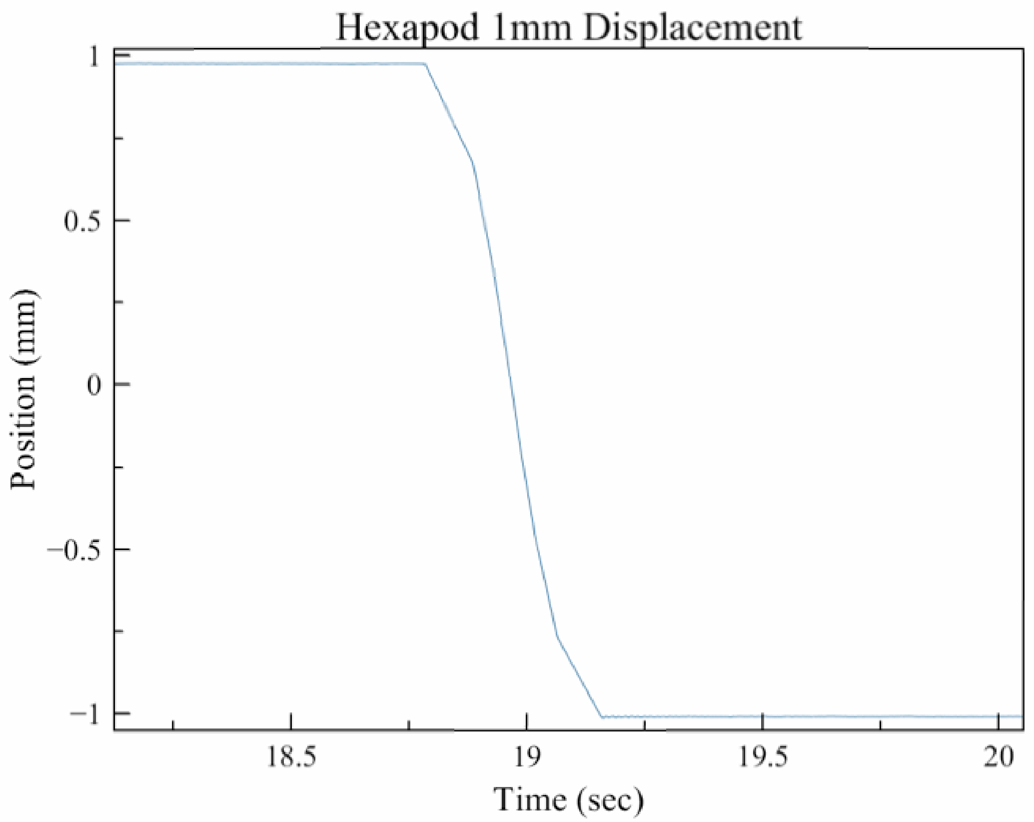

Figure 20. Hexapod Velocity and Acceleration Test

The hexapod was measured by the laser beam projected across the PSM as it was commanded to move 2mm from rest. This movement was then used to calculate the velocity and acceleration of the hexapod. The same test was also used to determine the velocity and acceleration of the XY stages.

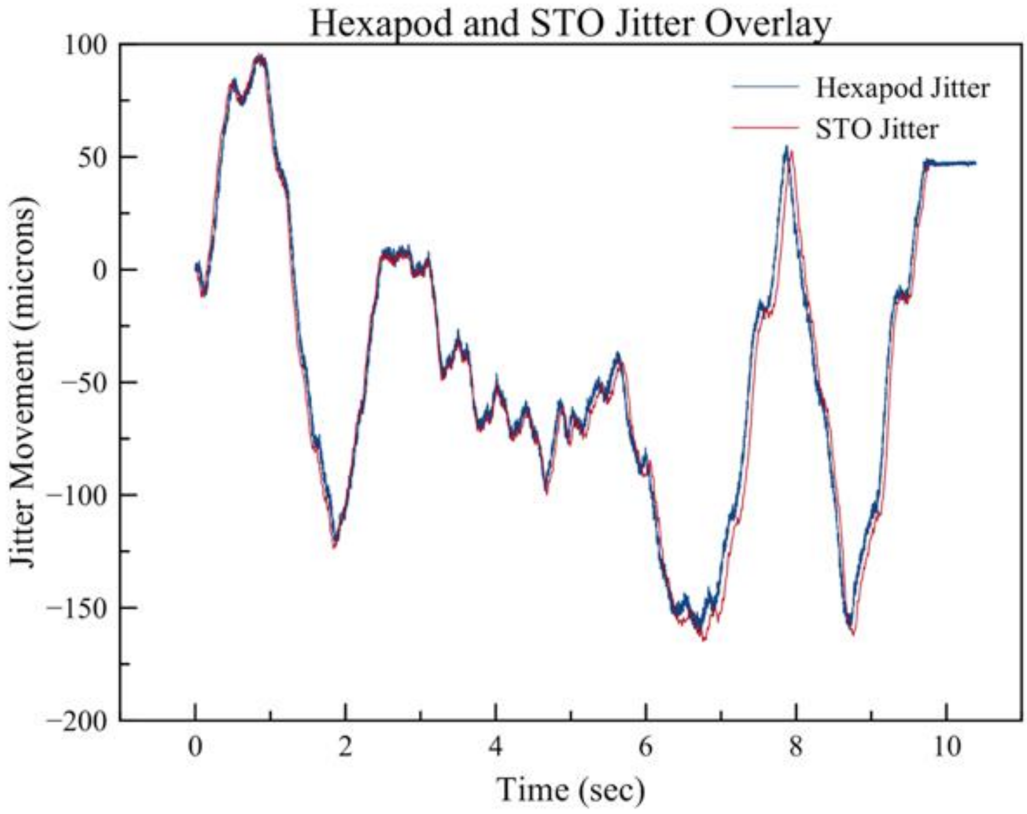

Figure 21. Hexapod Recreating STO Jitter Signal

Demonstration that the hexapod can match the precise shape of the error signal seen on the STO mission.

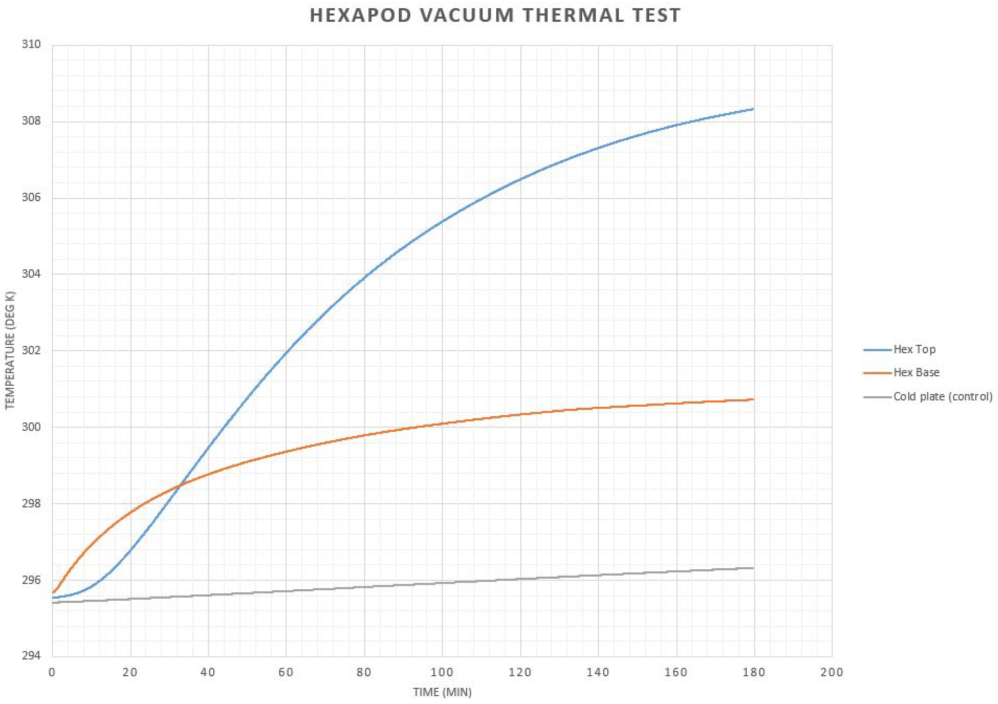

Figure 22. Hexapod Heat Production Under Vacuum

The hexapod was integrated inside the cryostat and the cryostat was then pumped down with no cryogen introduced. After pump-down, the hexapod was turned on and set through a series of movements to see if it was able to dissipate enough heat under vacuum to avoid overheat. The hottest part of the hexapod leveled out at ~30°C, which is comfortably below the hexapod's maximum operating temperature of 50°C.

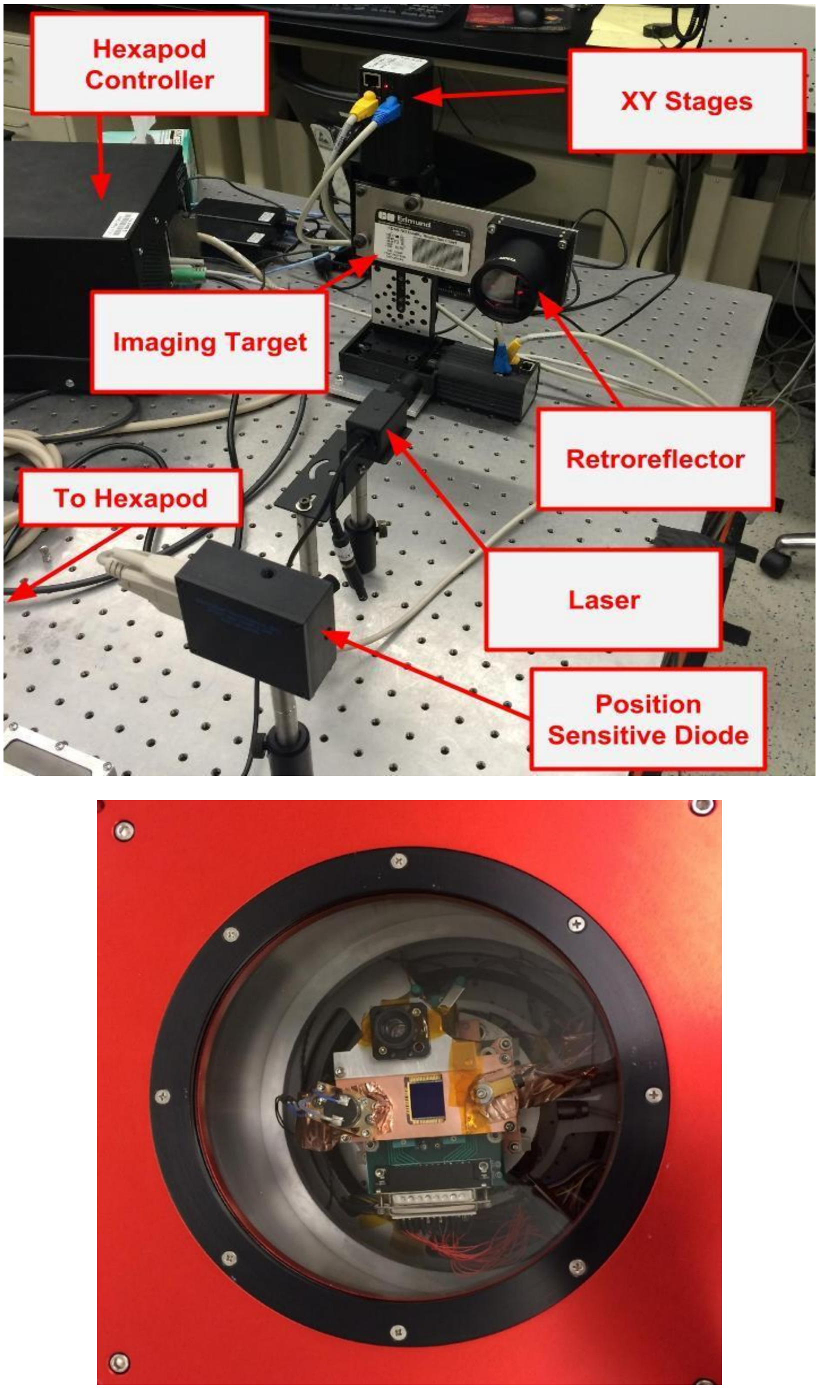

Figure 23. Phase III Test Setup

An infographic showing the XY stages, laser, retroreflector, and PSM simulating an error signal (above), and the hexapod with cooled CCD imaging through the cryostat window (below).

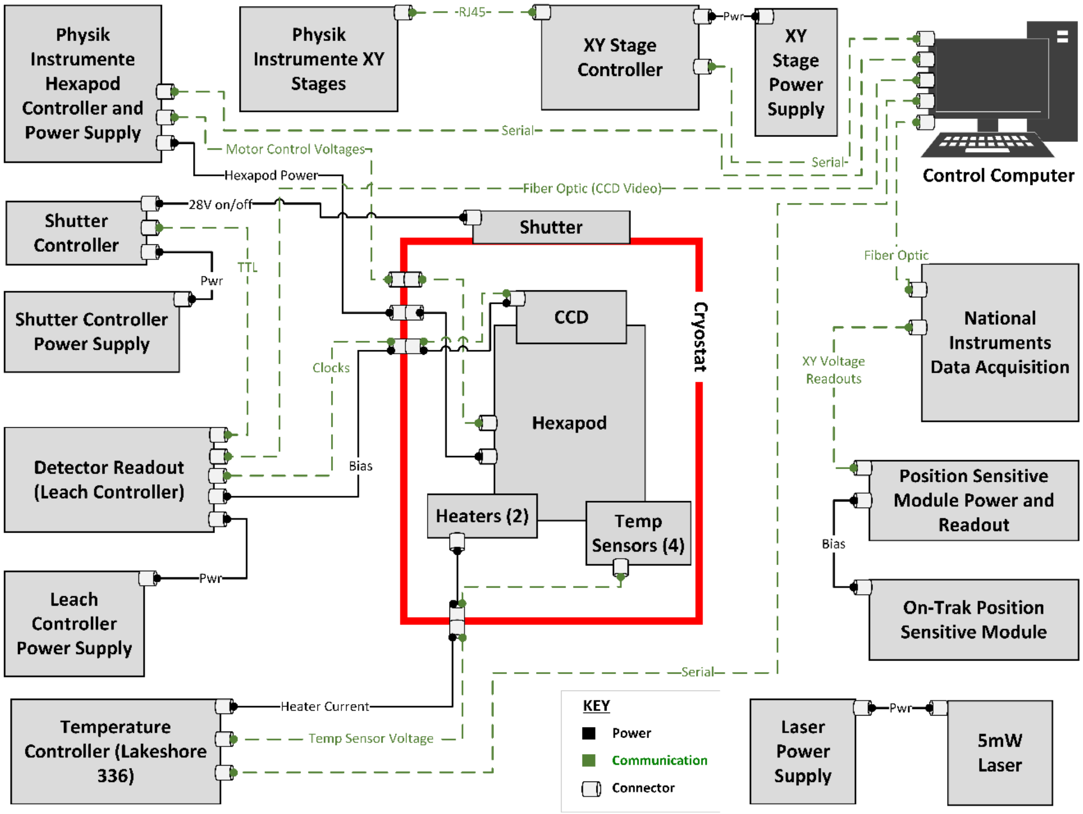

Figure 24. HERESY Laboratory Functional Block Diagram

A large amount of instrumentation was required to operate HERESY in its prototype form. In future iterations, these units could likely be designed to fit into a singular and compact avionics box.

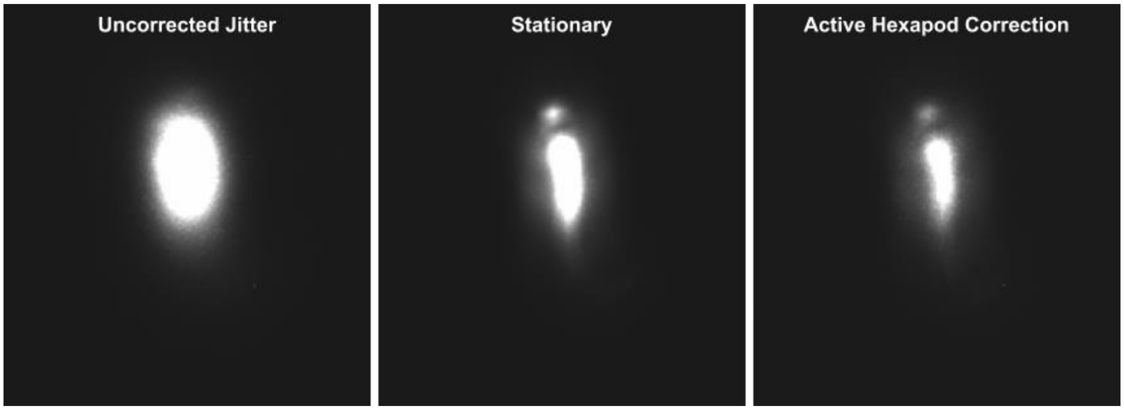

Figure 25. Filament Imaging Test

Sequence of identically scaled images of the illuminated filament demonstrating how HERESY can eliminate jitter and restore image structure during a 60 second exposure.

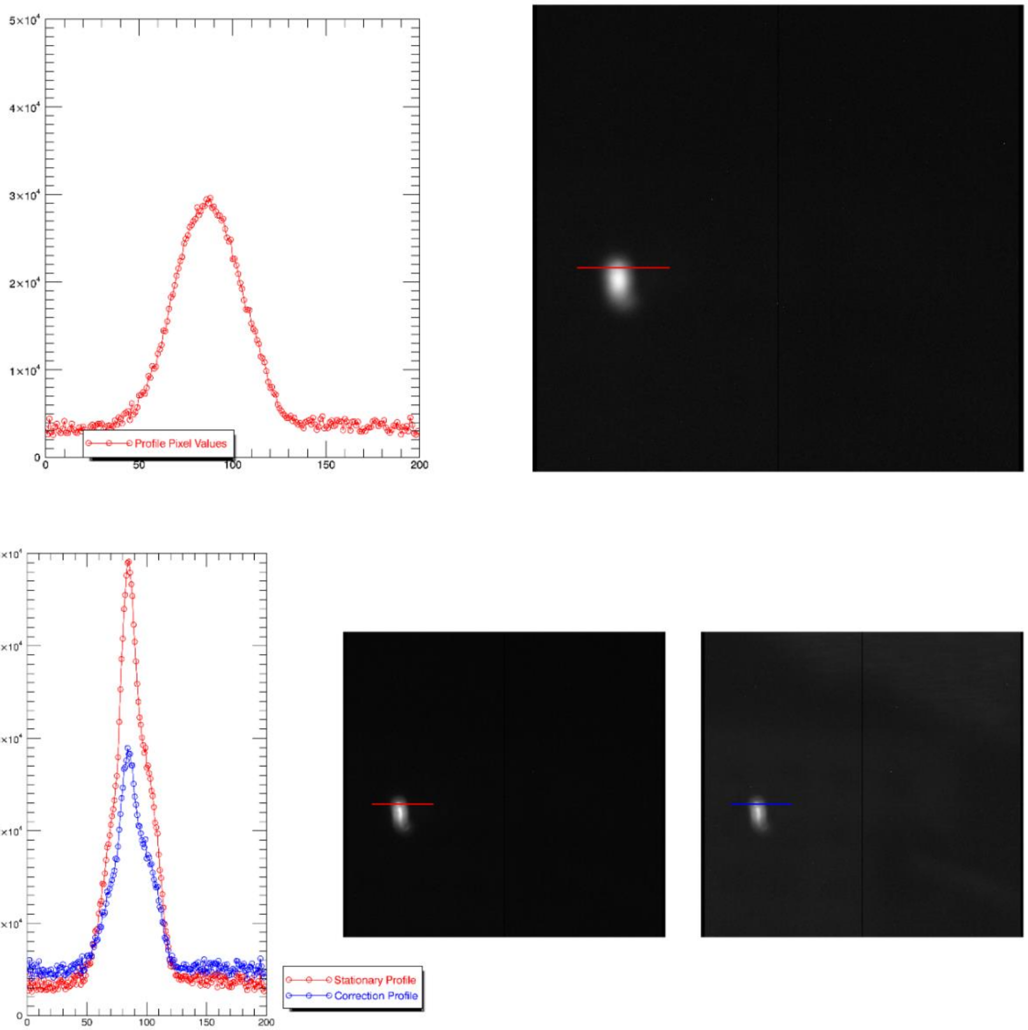

Figure 26. Filament Imaging Analysis

(Above) A 60-second exposure of the filament by a stationary hexapod with the XY stages recreating the STO jitter, (Below) 60-second exposure of the filament while everything was stationary and while the XY stages were recreating the STO jitter, but this time with the hexapod actively correcting.

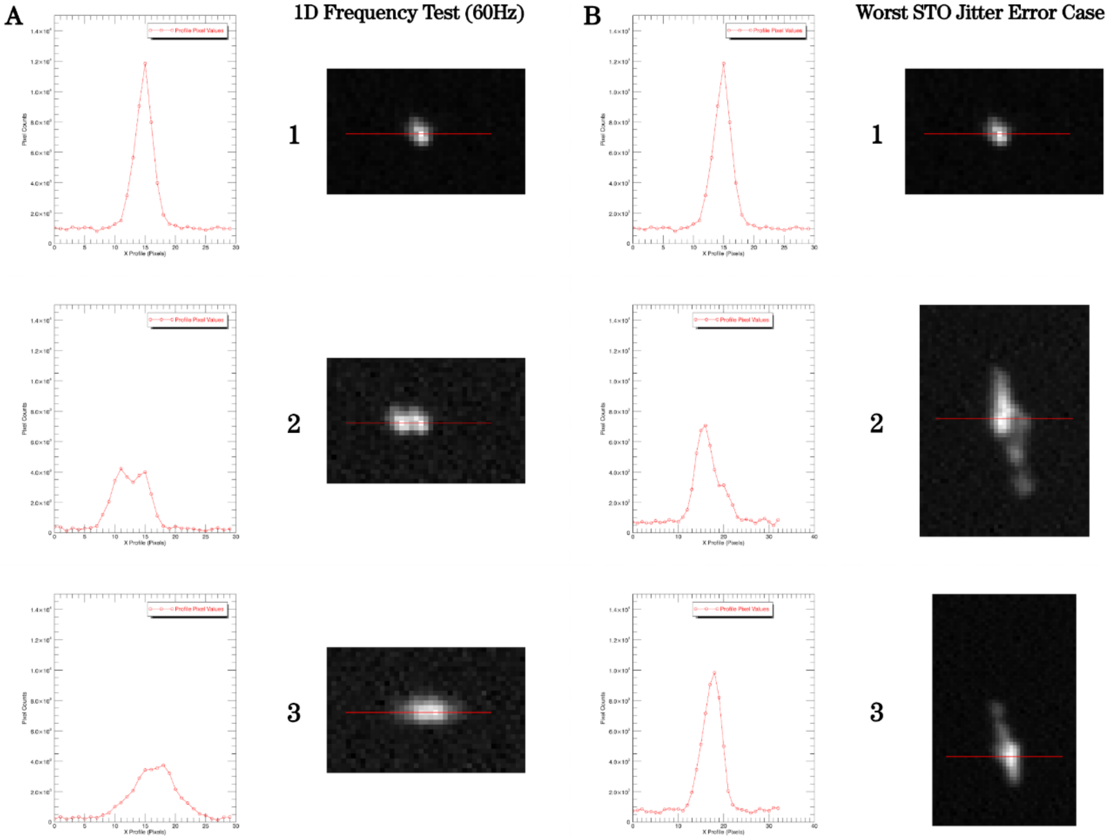

Figure 27. Hexapod Stress Testing

(A) shows a case where a point source was attached to the XY stages and exercised in a1D 100 micron back-and-forth pattern at 60Hz. (B) shows a case where an amplified version of the STO jitter signal was run (~25Hz and up to 300 micron displacement). The images in (A) and (B) were 30 second exposures – 1) is stationary, 2) is XY stages only with the hexapod stationary, and 3) is the hexapod actively attempting to correct for the error signal. In (A) 2) the image can clearly be seen to be bimodal in the profile graph, but the hexapod still manages to correct enough to reclaim the PSF gaussian in 3). (B) shows blurring that the hexapod could not completely correct, but the final image only sustained a ~17% decrease in peak intensity meaning the hexapod restored the bulk of the original PSF.

3 COLORADO HIGH-RESOLUTION ECHELLE STELLAR SPECTROGRAPH (CHESS) FOCAL PLANE

3.1 Background

Sounding rockets are suborbital boosters that launch instrumentation and experiments to Low-Earth Orbit equivalent altitudes. These missions are orders of magnitude less expensive than orbital missions but are limited by their short duration of flight (~15 minutes of data collection time). Therefore, they are primarily flown to space-qualify hardware/instrumentation or to retrieve data that must be collected outside Earth's atmosphere and does not require long duration measurement.

The Colorado UV Sounding Rocket Program at Colorado University (CU) Boulder has successfully flown several such sounding rocket missions. On the previous several CU – Boulder flights, the primary instrument was a high-resolution UV-optimized echelle spectrograph, known as CHESS, and has used a cross-strip anode Micro Channel Plate (MCP) detector to image the FUV bands in flight. MCPs have a rich flight heritage of space-based UV observing (FUSE and GALEX for example) but have the disadvantage of relying on a series of bulky high-voltage cascading electron-multiplier tubes (require ~300V).

At first glance, CCD or CMOS detectors would seem like an obvious replacement for MCPs with their smaller size, superior pixel density, extreme light weight, and low power requirement, but standard silicon detector Quantum Efficiency (QE) sharply drops to zero over any wavelengths bluer than the NUV (France, 2016). However, the Advanced Visible/UV Detector and Imaging Systems Group at JPL's Micro Devices Lab has pioneered a technique known as Delta-Doping where a silicon

CCD is enhanced via Molecular Beam Epitaxy to display impressive uniform sensitivity across the UV range. Delta-Doping is well characterized in the lab environment but needs a platform, such as a sounding rocket, to increase TRL in the space environment. The Delta-Doped CCDs that JPL produces are large format with a pixel pitch of 10.5 µm – this expands the array elements to over 30 times that of the MCP previously flown on CHESS while also reducing pixel size by a factor of 2.

Using delta-doping technology, a CCD's performance also remains a consistent ~30% QE across the FUV band compared to the ~15% FUV QE of MCPs (Blacksberg, 2008). Therefore, the efforts described in the following chapter were a collaboration between JPL, CU - Boulder, and ASU to fly a delta-doped UV optimized CCD aboard the Colorado High-resolution Echelle Stellar Spectrograph (CHESS) sounding rocket. JPL provided the detector, CU - Boulder provided the launch vehicle via their UV Sounding Rocket program, and ASU was responsible for integrating the JPL CCD into a flight-worthy payload for the launch. Therefore, I, representing ASU, essentially served as the 'middle-man' between CU – Boulder and JPL and worked closely with both groups to build up and deliver the rocket camera payload.

The initial mechanical, thermal, and electronic designs of the ASU-provided CHESS detector payload were previously modeled by my graduate predecessor before I took over the project. During my graduate work, I became the acting payload engineer, fabricated and tested all the payload flight components (including design iteration to implement needed modifications), wrote the interface code for control of the payload, characterized the flight detector (in the lab and on-sky), produced an Interface Control Document, and facilitated the delivery to CU – Boulder for launch integration.

3.2 CHESS Science Objectives

The science motivation behind the mission was to use a resolving power of R = ~150,000 over 100-160nm bandpass echelle spectrograph to measure key atomic and molecular spectra of the Local Interstellar Medium (LISM). The LISM has not been characterized in the UV (cannot be measured from the ground due to atmospheric absorption) with the resolution that CHESS can provide and the spectral features imaged will provide new insights into the inner workings of our immediate interstellar environment.

The benefit of the FUV for probing the LISM are the high-density of spectral features in this regime and, while previous UV space-based spectrographs seen on HST and FUSE had strict brightness limits, CHESS does not and can leverage high SNR LISM measurements by probing nearby young bright stars. Since the LISM determines the structure of the heliosphere, new results from CHESS can provide a new data set for the characterization of cosmic ray flux of the inner solar system, and since all stars and planets are thought to have similar interactions, then understanding our own local cosmic ray flux will help us to understand the flux of nearby exoplanets (France, 2016).

To explore different ionization environments of the LISM, measurements of different ionization stages are required. Additionally, thermal and elemental structure are key for determining three-dimensional morphology of LISM translucent clouds (Redfield, 2000). Temperature modeling of the LISM can help determine the evolution the local stellar neighborhood (Frisch, 2011). Resolution of regional temperatures is constrained by distinguishing the differences between thermal and turbulent variations within the cloud structure. This requires a high spectral resolution – a minimum of $R \geq 100{,}000$ for a $\Delta v < 3$ km/s within the cloud structure (France, 2012).

Elemental depletion within the LISM onto dust grains is another key to the complete model of the ISM. Measurement of serval ions can provide insight to depletion levels in the LISM. It is well understood that silicon and carbon are the two most abundant elements in the LISM, but these atoms are also known to be major ingredients of interstellar dust (Frisch, 2011). Therefore, for CHESS, it is important to measure several ionization states of the same species, so that data is not degraded by certain atoms in the LISM onto dust grains.

Each single CHESS science measurement captures an elemental ionization species across the FUV. Examples of these series are carbon (CI λ110.3 – 113.0, 126.1, 156.1; CII 103.6, 133.5; CIII 117.6; C IV 154.8,155.0 nm), nitrogen (NI λ113.5, 120.0; NII 108.5; NV 123.9, 124.3 nm), oxygen (OI λ104.0, 115.2; O VI 103.2, 103.8 nm), and silicon (SiII λ126.1, 126.4, 152.6,153.3; SiIII 120.6; SiIV 139.3, 140.2 nm) (Beasley, 2012). An example spectral measurement result from a previous CHESS mission can be found in Figure 28.

A science traceability matrix for the sounding rocket CHESS instrument can be found in Table 7. This matrix includes a list of science objectives and intended measurements as well as specified instrument performance to achieve these measurements. The specifications for the CHESS echelle spectrograph can be found in Table 1.

3.3 CHESS Engineering Objectives

The UV range is notoriously challenging to detect since Earth's atmosphere is completely opaque below ~250nm. Therefore, CHESS must be proven aboard a sounding rocket platform in space (above the atmosphere) to allow access to FUV. To measure spectral features across the FUV bandpass, CHESS utilizes a custom echelle spectrograph made from lithographically-ruled silicon. This custom echelle has orders of magnitude lower scatter and higher throughput compared to mechanically-ruled gratings. Hubble and FUSE's spectrographs cannot image the FUV spectrum (specifically 100-160nm) with even moderate resolution, so it is well worth increasing the TRL of the CHESS high-resolution, low-scatter echelle to open the door for advanced instrumentation on future UV/Optical space telescopes (Beasley, 2012).

The CHESS sounding rocket platform also provides an excellent platform to vet new detector technology in the space environment. This flight intended to test a Delta-Doped CCD from JPL. JPL Delta-Doped CCD technology is a method by which a few-atom-thick layer of highly doped silicon is deposited on the back of a CCD. The purpose of this highly doped layer is to alter the shape of semiconductor band structure to increase the internal QE of the detector to its theoretical silicon reflection limit.

Short wavelength UV photons tend to be absorbed near pixel structure surfaces (Kitchin, 2014), so the JPL devices are thinned and back illuminated. High substrate voltages (80V for the LBNL devices) are then applied to force the associated photoelectrons created from the interaction into the depletion region for readout (Blacksberg, 2008). Similar to the custom UV-sensitive echelle spectrograph on CHESS, proving these delta-doped detector's UV sensitivity in space aboard a sounding rocket will increase the TRL high enough to justify proposing the technology for use on a future UV/Optical space telescope.

3.3.1 Alternative Approaches to FUV Imaging

Detection of FUV photons in the 100 – 300 nm band drops to near zero for conventional CCD technology. The detection problem for these key wavelengths stems from the shallow absorption depth in silicon for photons of these wavelength and unstable surface charge intrinsic to standard back-illuminated devices. In front illuminated CCDs, shallow FUV photon absorption strands the created photoelectrons in the pixel structure and leads to recombination before the electrons can be captured in the depletion region. This problem is solved through thinning the CCD substrate and back illuminating the detector (photons are absorbed directly into the depletion region), however, in this configuration, FUV photons are susceptible to a potential over the native oxide layer that scatters electrons before reaching the pixel well (Hoenk et al., 1994). This is where JPL CCD delta-doping technology comes in to sharply alter the potential shape of the conduction band and overcome this back-illuminated photoelectron scattering issue (Blacksberg, 2008).

Over the years there have been several other successful approaches to FUV imaging. However, compared to the delta-doped CCD solution, these methods present a challenge for collecting high resolution images and often are susceptible to wildly varying FUV photoelectron yield (Hoenk et al., 1994). MCPs are one such technique (used on previous CHESS flights) which are essentially a grid of photomultiplier tubes that react to the incoming wavelength of interest and cascade energy onto an imager. The resolution of MCPs are constrained by the photomultiplier grid density and the yield greatly varies due to the cascading effect. However, MCPs have been flown successfully on several space missions.

Other approaches in the past have also utilized CCDs which include biasing a thin metal layer on the backside called a 'biased flash gate' and introducing a chromophore layer to transform FUV photons into visible photons for detection. Nevertheless, these too suffer from serious photoelectron yield discrepancies and over time are susceptible to long-term unreliability and the potential for radiation damage (Hoenk et al., 1994).

Therefore, delta-doped CCD technology from JPL truly presents a novel solution for the high-resolution detection of the FUV bandpass, provides unparalleled QE, and provides a stable data product for conducting high-quality photometry.

3.4 Sounding Rocket Launch ConOps

The Concept of Operations for the CHESS mission drove the requirements of the payload mechanical and thermal design. First and foremost, the harsh launch loads of the Black Brant IX rocket (Figure 29 is an image of the rocket being prepped for flight) are well characterized and therefore were accounted for using proven aerospace-grade materials and the construction of a shock-resilient payload structure. The CCD also needed to be cooled to its cryogenic operating temperature at launch, which proved to be an interesting challenge in itself. A spacecraft might use a radiator or thermoelectric cooler to maintain cold focal plane temperatures in flight, but since the data collection of the CHESS mission is ~15 minutes, a liquid nitrogen cooling loop was employed (for cost savings and simplicity). On the launch pad, first liquid nitrogen is circulated through the payload's cooling loop, bringing the detector to operational temperature. At launch, the liquid nitrogen umbilical is pulled away and as the rocket increases in altitude the unpressurized payload electronics compartment begins to decrease in pressure.

Another issue was that as the rocket passes through the stratosphere and above, convection is eliminated meaning that the payload electronics must have a conductive or radiative method of dissipating their heat. Due to the short rocket flight time, the solution for CHESS was to heat sink all the electronics in a way to survive for at least the data collection period of the flight.

After reaching peak altitude, the science targets then needed to be pointed to so that the UV light collected from them could be reflected off of the echelle grating. If this was an orbital mission meant for long-term survivability exotic materials might have been used as an FUV window (transparent in FUV wavelengths), however, for simplicity the CHESS payload setup has a shutter that simply opens to the space environment with no window for letting light hit the echelle spectrograph. At the top of the rocket launch parabola, data collection is initiated by a line-of-sight communications link and low-resolution images are downlinked to the ground in real-time in an effort to preserve data in case of a botched landing or recovery effort. Science targets preselected well before launch are pointed to via reaction wheels. Finally, the rocket reenters Earth's atmosphere, deploys a parachute, lands, and is recovered via helicopter.

A high-level requirements matrix for the sounding rocket CHESS detector instrument can be found in Table 9. This matrix includes the flow-down science and environmental requirements that defined the mechanical, thermal, and electrical interfaces of the detector payload. Figure 30 shows a labeled cutaway look at the

CHESS rocket payload interior to serve as a visual for where the detector instrumentation is positioned within the rocket skin.

3.5 CHESS Detector Payload Instrumentation

The detector is a back-illuminated two-layer delta-doped 3.5k × 3.5k SNAP LBNL p-channel CCD with enhanced QE in the FUV. The device is 300 µm thick and requires a high substrate bias voltage (40-80V) in order to fully engage the depletion region (Bebek, 2006). Clocking signals and DC voltages are provided to the CCD through a custom PCB interface board, and a copper mass is clamped to the backside of the detector for cooling. The copper mass has a liquid nitrogen fill tube in its interior and a temperature sensor and resistive heater are mounted near the CCD to monitor and regulate thermal conditions. The detector, thermal sensor/heater, and copper mass are all contained within a cylinder with electrical feedthroughs and liquid nitrogen fill tube on one side and a vacuum conflat on the other side, which will mount to the CHESS rocket.

Exterior to the 'focal plane section' is the small-cam controller, which both provides waveforms to operate the CCD as well as readout and digitize the output video signals. An RTD computer is used to communicate with Small-Cam, start desired exposure sequences, and store image products. An Omega temperature controller and heater circuit is used to hold the detector at its operating temperature +/- 5°C. To increase readout speed, the CCD reads charge out in four quadrants simultaneously. The video signals from these quadrants are sent to custom pre-amplifier boards where they are amplified and split into differential signals for noise reduction before being sent to Small-Cam's ADCs for final image reconstruction.

Figure 31 shows a high-level block diagram for the detector payload and interactions between all its associated components.

3.5.1 Preamps

A series of four preamplifiers (one for each CCD output) are employed to amplify and condition the CCD video signals (seen in Figure 32). Shielded coaxial cables first transmit the video signals into the pre-amplifier inputs to prevent electromagnetic interference (EMI) noise. The preamps correct a known -18 volt DC offset intrinsic to the LBNL delta-doped CCDs. Each video signal is then amplified and turned into a differential signal (inverted/non-inverted) and then are transferred by more coaxial cables to the Small-Cam CCD Controller where the differential signals are recombined to eliminate noise. It is also worth noting that four 20 kOhm resistors are also mounted from the CCD input signals to ground to act as the load resistors for the CCD output amplifiers per the LBNL specs (Veach, 2013).

3.5.2 Thermal Control

The thermomechanical structure must both bring the CCD down to cryogenic temperatures and then be capable of holding a temperature to within +/-5 deg k. In addition, the thermomechanical structure must survive the high sustained g-force of rocket flight. When cooling detectors in a lab environment, custom cryostats are often used, which have decently sized holding tanks that can be used to store cryogen for keeping instrumentation cold for long periods of time (typically 12-24 hours). However, due to the logistics of rocket flight, the detector payload was required to be designed in a way that allowed the CCD to be cooled down to and held at its operating temperature without the use of a cryogenic fill tank.

Therefore, the thermomechanical structure of the payload was designed with two exterior input/output VCR pipe fittings attached to internal copper piping. Liquid nitrogen is then pumped and flowed into the VCR fitting and through the copper pipe. A schematic of the thermal cooling system is seen in Figure 33. Two copper blocks with a channel cut in them to match the copper piping are then clamped snuggly over the copper pipe, creating good thermal contact between the piping and clamping blocks. Finally, a cubic copper 'cold head' is mounted on top of the underlying copper cold structure to form a robust thermal mounting point for the CCD. To conductively isolate the thermomechanical structure from the rest of the payload structure, all of the copper is thermally buffered from the rest of the payload via G10 fiberglass mounts. An image of the copper cold structure fully constructed along with associated SolidWorks thermal modeling can be seen in Figure 34.

CCD temperature is monitored and controlled by a compact Omega temperature controller (seen in Figure 32) and custom heater circuit. A small resistance temperature detector (RTD) is mounted close to the CCD thermal interface and used to report CCD temperature. Two 25 watt heaters are mounted within the 'cold head' and are turned on or off based on a PID loop in the Omega controller. The Omega PID outputs an analog voltage based on a chosen setpoint.

Since the controller cannot provide enough current to heat the copper cold head and the CCD, a custom heater control circuit was designed and added to the system. The heater circuit takes the analog output from the Omega controller and processes it through an op-amp. The op-amp then delivers one amp of current into a thermal control circuit that terminates in a MOSFET switch. When the MOSFET is in its on state, it enables current to flow to the heaters at the CCD cold head. The heater duty cycle is dependent on the output of the Omega PID signal over time.

3.5.3 Small-Cam Leach Controller

The architecture of Small-Cam is extremely similar to the Leach controller used in HERESY that was described in the previous chapter. However, volume and mass restrictions play a much larger role in rocket payloads than balloon payloads. Therefore, Small-Cam is a custom-built CCD Leach controller optimized for compactness. It is roughly a third of the size of the standard OTS Leach controller. The controller provides the DC voltages and AC timing signals to operate the device and reads out the CCD video with a 16-bit ADC (http://www.astro-cam.com). During the characterization and fine-tuning of the Small-Cam clocking signals, a logic analyzer was used to map timing pulses. A capture of the square wave pulse structure of the vertical and horizontal clocks of one of the CCD quadrants can be found in Figure 35.

Input/output from the controller to the CPU is done over fiber optic cable. The controller is also capable of precisely operating a shutter by TTL on/off signal. An image of the controller chassis and connector interface is found in Figure 36.

3.5.4 RTD Computer

The payload flight computer is a ruggedized PC/104 Intelligent Data Acquisition Node (IDAN®) Intel9 Core 2 Duo 1.2 GHZ designed by RTD Embedded Technologies (www.rtd.com). The computer was chosen to provide enough computing power and have sufficient RAM for on-the-fly data reduction and enough storage space for data storage until after the rocket is recovered. The storage disks are solid state for robustness on a sounding rocket flight and for use in low gravity. Communication is available through serial port or Ethernet.

To reduce risk, a CU – Boulder requirement was to ensure that the operating system could boot up in under 20 seconds (part of Table 9, high-level requirement 3). This would ensure that a power flicker in the rocket 28 volt line or a commanded reboot to troubleshoot an issue would not cut too far into the ~15 minutes of data collection time. To accommodate this, Fedora LXDE – a minimalist version of Linux – was chosen. This was useful to accommodate both lab testing and as an operating system for flight since it allowed for an X11 desktop environment when desired but could also be preset to default to command-line only. The boot time for this version of Fedora loaded onto the RTD 'out-of-the-box' was approximately 50 seconds, but this was able to be cut down to 15 seconds by using a *systemd-analyze* command line and manually disabling operating system (OS) services such as network WiFi search tools, Bluetooth, and auto journaling (background data logging tool). In addition, the OS was hard-coded to boot to a command line when powered on and automatically run the flight software for command of the CCD. From the ground, the RTD could then be accessed via secure shell over ethernet through a line-of-sight communications link. The functionality of the CCD command code is covered in a later section.

RTD IDAN specifications can be found in Table 10. An image of the RTD computer in its flight chassis can be found in Figure 36.

3.5.5 Structure

The detector payload was required to hook on to an existing optics opening on the rocket to enable imaging of the echelle spectra. The interior of the rocket is held under ultra-high vacuum (UHV) before launch to prevent contamination, which was a driving requirement for the payload structural seals. Therefore, the cylindrical payload structure ends are 6.75 inch knife-edge conflats (sealed by copper gaskets) and is 5.96 inches long, so that when mounted, the detector is positioned at the focal point of the spectrograph.

The structure also had to be designed to survive the extreme rocket vibrational launch environment. Therefore, all load-bearing components and fastener hardware are constructed from stainless steel. One challenge of the design was to make sure the structure was both vibrationally robust and thermally isolated from the exterior environment. Since the CCD is clamped onto the copper cold structure, if the system was not rigid enough, it could lead to catastrophic destruction of the delicate silicon focal plane. Therefore, the main copper cooling structure was bolted in the center of one conflats side with the welded fill-tube inside of it for cool-down. Any area where the copper would potentially contact the rest of the bulk stainless-steel tube was thermally buffered by clamping G10 fiberglass between the interface. On the exterior, but not in contact with, the four corners of the copper cold structure, four stainless steel rods were also mounted to the conflats. These rods, which rise around the cold structure, have 4-40 tapped holes on their tops to provide the support for CCD mounting. There are also four clamping arms that hold onto a G10 fiberglass sleeve that fits snuggly onto the cold head to ensure that the thermal interface to the CCD cannot wobble. As a final safety measure, the four rods are also bound to each other via stainless steel safety wire.

Mechanical stress on the payload structure imposed from launch loading was modeled in SolidWorks. 10 and 100-g axial and orthogonal loads were simulated, with

10-g being the average load expected with rocket engine on and 100-g used as a stress test. The 10-g load showed <7 micron displacement of structures which was well within safe limits and less than a CCD pixel size. The 100-g load showed displacement of 4 microns in the axial direction and up to 70 microns orthogonally. From this analysis the structure was deemed safe for flight with a large safety factor (Veach, 2013).

A challenge of the design was to create a mechanism that would ensure thermal contact between the CCD and the copper cooling structure. If a rigid system is built that simply holds the CCD thermal mounting interface on top of the cold head, during cryogenic cooling, the copper would contract and 'pull away' from the CCD, effectively preventing cool-down. For laboratory applications, springs are typically employed to gently push the CCD into the cooling structure, and when thermal contraction occurs, the CCD is placed on tracks and constantly pushed into and held against the cold surface. However, due to the extreme vibrational environment of sounding rocket launches, low force springs in the system could create a 'bouncing effect' and continually smack the CCD into the cold head at high frequency.

To solve this issue, Belleville washers were used – which act as springs but increase damping in the high-G environment of rocket launch. Due to the delicate nature of the LBNL flight CCD, to solve this issue, a digital torque wrench was employed to precisely tighten the Belleville washers holding the CCD to the cold head. After integrating the CCD onto its interface PCB, a custom aluminum part both clamps together the CCD/PCB structure (to make sure the CCD does not come loose from its connectors), and has through holes where long 4-40 screws are fed-through leading to the stainless steel rods discussed in the last paragraph. The 4-40 screws act as ‘tracks’ that allow the CCD to move in the z-direction and the Belleville washers discussed earlier act as the forceful springs that keep good thermal contact between the CCD and the cold head.

3.6 CHESS Detector Characterization

As part of the verification and validation process, the CCD from JPL needed to be independently characterized at ASU to prove that the CCD showed acceptable performance when integrated into the flight payload. Since the sounding rocket flight profile only allows for ~15 minutes of data collection, it becomes important that the detector read time is as low as possible (to minimize time between exposures) and SNR is high as possible (high Quantum Efficiency and low read noise).

3.6.1 LBNL SNAP 3.5k x 3.5k CCD

The CCD selected for CHESS is a 3.5k x 3.5k device SNAP LBNL probe (flight spare from the SuperNova Accelerator Probe mission, Albert, 2005) with 10.5 micron square pixels – bringing the total active area of the CCD to 36.8 mm^2. For the engineering build-up, JPL provided several of these detectors for testing. The CCDs are packaged by JPL in a ‘picture-frame’ configuration. This is essentially a square PCB with a square aperture cut out in its center (hence the picture-frame look) containing wire traces that terminate in two 2-row 40-pin male header pin connectors. Since JPL thins the devices for back-illumination, the CCDs are thermally epoxied to a rectangular piece of AlN (aluminum nitride) and then the AlN bulk is epoxied onto the frame of the PCB. This placed the CCD in the middle of the ‘picture frame.’ Voltages and signals are then passed to and from the CCD through a series of gold wire bonds that connect the CCD traces to the PCB picture frame traces. 2-row 40-pin header connections are a very common electrical interface, making it relatively straightforward to design an interface board to connect with the CCD PCB. Figure 37 shows an electrical layout of the PCB designed to mechanically and electrically connect the CCD to the detector payload for testing and flight.

While displaying many characteristics similar to other scientific-grade CCDs, the LBNL SNAP devices exhibit several unique characteristics. Most solid-state detectors can operate at room temperature despite a higher dark current production rate. However, it was observed that the SNAP CCDs become over-saturated and unusable due to dark current at around 220 k (their nominal operating temperature is between 140 – 170 k). Most solid-state detectors can also be powered while under typical fluorescent room illumination (what you might expect overhead lighting to be in a normal lab environment), but the SNAP CCDs are advised to never be powered under room lights since they can undergo an effect called 'super-saturation' where the oxide layers can be damaged if full pixel well is held >1000 times the full well charge for an extended time. Like most CCDs the SNAP CCDs are also very sensitive to electro-static discharge (ESD).

With all these factors combined, it can become challenging to work in a test environment with these devices. A slip-up where the proper ESD safety equipment was not used, or the detector is exposed to direct room lights while powered can end up in a blown detector – and each CCD is extremely challenging and expensive to produce. In addition, since the LBNL CCDs remain saturated at any temperature above cryogenic levels, it can take several hours to perform even the simplest of tests. Despite these challenging aspects, by following many carefully planned procedures and techniques, the flight CCD was able to be characterized and integrated into the flight payload without destruction.

3.6.2 QE

JPL performed an initial ‘aliveness’ test for the flight CCD as well as confirming the CCD was sufficiently sensitive in the FUV. However, verification of the functionality of the CCD was required when integrated into the ASU flight system. Therefore, an ASU characterization of the flight CCD was performed, but only in the near-UV to near-IR range due to limitations of the LASI test equipment.

My procedure for laboratory testing was to first mount the flight CCD in a windowed cryostat with the advantage of a liquid nitrogen tank capable of keeping the detector cold for up to 12 hours. A shutter was mounted in front of the window that was precisely operated by a CCD controller via TTL. Finally, the entire setup was mounted inside a ‘dark box’ with a NIST-calibrated photodiode and monochromator setup. A diagram of the test setup is found in Figure 38. The system was automated by a Python code that collects data in increments of 10nm (max resolution of the system based on slit size of monochromator). The response functions of the photodiode and CCD are then compared by the ‘Janesick QE method’ using the relationship of these equations:

$$\mathrm{QE} = \frac{A_D\, S(\mathrm{DN})\, G_{ADC}(\mathrm{e}^-/DN)\, \mathrm{QE}_D}{P_A\, S_D\, T_i}$$

$$\mathrm{QE}_D = \frac{12390\,R_e}{\lambda}$$

where A_D is the active area of the photodiode (cm^2), S is the raw SCCD signal (DN), G_{ADC} is the gain of the CCD, QE_D is the QE of the photodiode, P_A is the pixel area (cm^2), S_D is the current generated by the photodiode (e^-/sec measured by a picoammeter), T_i is the exposure or integration time (sec), and R_e is the calibrated photodiode responsivity expressed amps per watt and is provided by NIST. The result from using the formulas above allows for the plotting of a QE % vs. Wavelength graph (Janesick, 2001).

Figure 39 is a plot of the measured QE of the CCD using the setup and formulas described above. Each plotted point represents a 10nm step of the monochromator as it scanned through the NUV-optical-NIR wavelength range. The blue shaded region shows the error bars for the QE measurements and the purple '1-r Si' line represents the maximum QE that a silicon-based detector can achieve due to the light-loss induced by the reflectance of silicon itself (Green, 1995).

3.6.3 CCD Photon Transfer Curves (PTC)

Unlike QE, for Photon Transfer Curves (PTC) measurement a photodiode was no longer needed, and instead the monochromator was used to evenly illuminate the CCD without needing to change wavelengths. Using an automated Python code, the exposure time was gradually increased until detector saturation. Two images must be taken at each exposure level to accommodate the noise calculation (see below). Plotting CCD signal vs. noise on a log-log graph forms the PTC. From the curve one can obtain pixel full well, linearity, and gain. PTC calculations are performed with uncalibrated raw frames so that noise characteristics of the detector are persevered. Signal and noise are calculated from windowing a 100 × 100 pixel region of the CCD raw frame and using the following equations:

$$S(DN) = \frac{\sum_{i=1}^{N_{pix}}[S_i(DN)]}{N_{pix}} - S_{OFF}(DN)$$

$$\sigma_S^2(DN) = \frac{\sum_{i=1}^{N_{pix}}[S_i(DN) - S(DN)]^2}{2N_{pix}}$$

The 10,000 pixels (100 x 100) are then averaged and a fixed electrical offset subtracted, where S(DN) is 'signal' in digital numbers, $S_i(DN)$ is the signal value of the ith pixel, N_{pix} is the number of pixels in the windowed array (in this case 10,000), and $S_{OFF}(DN)$ is the average offset level. For the noise calculation, the standard deviation is found after pixel-to-pixel non-uniformity is removed. This is done by subtracting two back-to-back frames taken at the same exposure level. A factor of two must be included in the denominator of the noise calculation since, when two frames are subtracted from each other, the random noise of the final product increases by the square root of two (Janesick, 2001).

For the CHESS mission, the LBNL SNAP CCD is required to readout in 20 seconds or less. Read noise increases proportionally as read time decreases, so it was chosen to read out the detector at the maximum allowed 20 seconds in an attempt to achieve the best noise performance. The CCD is a 12.2 MegaPixel device and has four separate output amplifiers (one in each corner of the device) thereby dividing the detector into four quadrants. Therefore, reading out the four quadrants in 20 seconds yields a 150 kHz clocking rate for the CCD control electronics. Read noise is calculated by PTC or by comparing the difference frames of two flat fields and two biases.

Figure 40 shows the PTC calculated for the flight CCD. A curve was formulated for each quadrant, since with four different readout registers, detector performance varies. The full pixel well was confirmed to match up with JPL documentation of ~120,000e$^-$/pixel (Bebek, 2006).

3.6.4 CCD Read Noise

A key requirement for the CCD to be feasible for the CHESS mission was that it had to perform with <20 e$^-$ read noise (part of Table 9, high-level requirement 2). The higher the read noise, the longer the required exposure time to boost the SNR to acceptable levels, and since the sounding rocket only allows for ~15 minutes of data collection, it becomes easy to understand the need to lower the noise floor. To measure detector noise, a Janesick method that involves a data reduction of two unprocessed flat fields and bias exposures was used. The detector gain must first be calculated, which is needed to give the final CCD noise number in electrons (e$^-$). The formulas are as follow:

$$Gain = \frac{(\bar{F}_1 + \bar{F}_2) - (\bar{B}_1 + \bar{B}_2)}{\sigma^2_{F_1 - F_2} - \sigma^2_{B_1 - B_2}}$$

$$CCD\ Noise\ (e^{-}) = \frac{Gain \times \sigma_B}{\sqrt{2}}$$

Where $\bar{F}\,\bar{B}$ represent an averaged flat-field and bias respectively. The $\sigma^2_{F_1-F_2}$ term represents the squared standard deviation of the difference between two flat fields (Janesick, 2001). The same is also taken for the bias exposures. The QE and PTC characterization of the LBNL CCD was done in a cryostat test chamber that included a window for easy illumination of the focal plane. However, after initial prototype verification and validation, the CCD then needed to be transferred to the rocket payload conflat structure for final functional checkout.

While as similar as possible to the electrical scheme of the original cryostat setup, the connector and wiring schemes were slightly different on the final payload. In addition, in the original test setup, different instruments were being powered by different independent power supplies and could be positioned at various distances from each other depending on whatever the layout on the optics bench was during any test. After the CCD was integrated into the rocket payload structure the first problem was that it was not designed to allow the for the illumination of the CCD unless it was integrated onto the rocket itself – therefore, a solution had to be figured out for how to take a flat-field of the detector while inside the rocket payload structure.

The solution was to mount two incandescent bulbs inside the rocket payload. In the original prototype setup, a TTL signal line from Small Cam was used to control a shutter, but instead this line was applied to the light bulbs. Therefore, any "exposure time" set in software would instead turn on the light bulbs (rather than exercise a shutter) for the defined period of time. A four-quadrant illuminated CCD in the rocket payload can be seen in Figure 41. Using this illumination method, bias frames (or zero second exposures) as well as flat fields could be taken to perform the read noise calculation outlined above.

It was immediately apparent that the initial electrical setup and testing of the payload contained several EMI and ground loop issues. Initial measurements of CCD read noise was >300 e^-, which is high enough to assuredly point to a major electrical flaw. Based on past characterizations of the LBNL devices at JPL, read noise was measured as low as 3 e^-, so there was obviously room for improvement. In the lab test setup of the equipment, the preamps, Small-Cam, and the flight computer were all being powered by separate power supplies, so the first corrective action involved reconfiguring the power and grounding scheme into its final flight form. This meant that a single +28 volt line was split out to be the power input to the RTD flight computer, temperature controller, and Small-Cam. The preamp boards were powered from positive and negative 15 volt outputs from Small-Cam. All unit chassis were then mounted to a custom aluminum plate to ensure a common ground. A star-point was established on the aluminum plate which served as a connection point to the cryostat chassis.

A ground issue was also identified in Small-Cam by the vendor where extra grounding connections needed to be added between the interior boards. All the boards then had to be connected to the star-point ground to solve the issue. With this new power and ground scheme, the read noise measurements of the CCD were cut in more than half with each quadrant read noise measured around ~150 e^-. However, this read noise level still needed to be decreased by a factor of 10 to be acceptable for flight. Therefore, the last step was to work to rewire all exterior cables to ensure the right signals were grouped together in twisted shielded pairs, make sure that the connectors were adequately grounded, and finally to make sure the cable harnesses themselves were tied to the common star-point ground point on the aluminum plate. With this effort complete, each detector quadrant's read noise was brought down between 10-15 e^- thereby fulfilling CU – Boulder's requirement.

3.7 Observatory Testing

In parallel with the build-up of the CHESS project, a further partnership with JPL was established to help support a Strategic Astrophysics Technology grant (SAT) that they were awarded to demonstrate the functionality of their delta-doped LBNL SNAP CCDs. This was a logical extension of the CHESS project work, as the test apparatus was already in place to test these specific detectors. However, for the SAT project, JPL provided a detector of the same architecture as the CHESS flight device but with an Anti-Reflective (AR) coating. Coupled with delta-doping, thinning, and backside illumination – the AR coating impressively delivers >90% QE over the visible range for the LBNL devices. However, these same AR coatings are opaque in the FUV range which is the CHESS mission's target wavelength range, therefore the CHESS flight CCD is an 'uncoated' device. Since the AR coated SNAP CCDs were electrically identical to the uncoated CHESS flight CCD, this was a great opportunity to gain experience working with these types of devices.

3.7.1 Observatory Setup

Converting a laboratory test setup into an instrument that can be mounted on a telescope is a challenging task. It is true that all the instrumentation was built to be compact for flight on the CHESS sounding rocket, however, the Colorado team was responsible for mounting the instrumentation after delivery. Therefore, the AR coated CCD was mounted within the windowed cryostat mentioned earlier, but all the electronics boxes responsible for things like shutter control, power conditioning, temperature control, etc. had to be mounted on the telescope. The reason these loose components become an issue is that they cannot be simply left on the observatory floor since the telescope has a large travel range and tracks the sky during observations. Therefore, the components had to 'fly' above the observatory floor while attached to the telescope.

To accomplish this a steel box with a door attached was procured. A custom aluminum shelf was built and inserted and additional slots were added in the bottom of the box. After the instrumentation was placed through the door into the box, ratchet straps were run through the slots to securely fasten each component into place. The CCD controller itself, Small-Cam, had the shortest cables (by design, meant to reduce noise), so this was ratcheted directly to the side of the CCD cryostat. The telescope that the tests were conducted on was the 61" Kuiper Telescope on Mt. Bigelow in Tucson, Arizona run by University of Arizona's Steward Observatory. Therefore, to mount the box to the 61" scope, work was performed the Steward Observatory operations team to come up with a robust solution involving large steel brackets. The mounting of the steel box mass onto the side of the telescope created a large moment arm, but the telescope fortunately can be rebalanced by the observatory team to accommodate it. Figure 42 shows the CCD test setup and all associated electronics mounted to the back of the Kuiper 61" telescope.

There were a couple issues with this AR coated SNAP CCD that are worth pointing out – there were known cosmetic defects on this particular device (considered ‘experimental’ by the JPL team) including large swaths of dead columns running through the center of the CCD that showed up as either dark bands or completely saturated bands and only two of the four quadrants were operational.

In addition to the existing CCD issues, the position of the focal plane on the back of the telescope was slightly different than the detector system that is resident to the Kuiper Observatory, the Mont4k. This meant that the telescope had to be slightly refocused to account for this discrepancy, and since the guide camera on the telescope used a pickoff mirror and did not have an adjustable focus of its own, the guide camera was then out of focus. While the telescope beam was properly focused onto the SNAP CCD focal plane, since the guide camera was out of focus and essentially unusable, the resulting images taken were blurrier than ideal due to the reduced telescope tracking ability.

After the SNAP CCD in its cryostat, and the rest of the associated electronics were finished being mounted to the back of the telescope, the CCD was cooled down with liquid nitrogen and performed a complete functional checkout. This involved checking the temperature controller (heater operation and temperature sensor readout), exercising the shutter, and taking test images. After all equipment functionality was confirmed, a series of bias, darks, and flat-field calibration images were taken. The biases were zero second exposures, the darks were taken with the shutter closed and were representative of the intended science exposure times (300 seconds), and for the flat-fields, the observatory had an illuminated out-of-focus target that the telescope could be pointed to for even illumination of the detector. The telescope also had a UBVRI filter wheel installed, so a series of 10 flats were taken using each filter.

3.7.2 Observatory Results

The first part of the observing run with the AR coated CCD involved tracking down and eliminating nagging noise issues due to the wiring and ground issues. The first several on-sky images displayed varying horizontal banding features indicative of RF interference with the CCD signal cabling. Additional on-the-fly shielding was added to the cabling using aluminum foil. It was also ensured the cryostat chassis, preamps, and Small-Cam shared a common ground, which helped reduce the issue but did not completely solve it.

After improving the noise quality of the images, the observing run involved imaging a set of photometric standard stars as well as several Messier catalog objects as a demonstration of the CCD's operation. Several Landolt standard stars were selected to image in the hopes of performing post-processing to obtain on-sky QE. However, post-analysis of the photometric frames showed that too much lingering RF noise adversely affected the images so that no accurate on-sky QE could be obtained. This same noise issue was unique to the observatory and could not be repeated in the lab.

Images of M64 (Black Eye Galaxy), M51 (Whirlpool Galaxy), and M104 (Sombrero Galaxy) were taken using V, B, and I filters. Identical 300 second exposures for each of the V, B, and I raw frames were taken three times to allow for median combined images to eliminate cosmic rays. In post processing, IDL was then used to subtract average bias, and perform flat-field correction for every raw image. Then RGB was assigned to the associated VBI filter images and stacked to produce color images.

Since there were telescope tracking issues due to the guide camera being out of focus, the images were blurrier than ideal and also had to be translated significantly during RGB stacking, to make sure the imaging target lined up correctly. As a result, the cosmetic defects of the CCD were more pronounced with multi-colored banding appearing across the images. A dark frame showing an example of the amount of cosmic rays picked up by the LBNL CCD can be seen in Figure 43. The RGB stacked images of Messier objects can be seen in Figure 44, Figure 45, and Figure 46. Despite the issues endured during observatory testing, the project was deemed a success since this was the first on-sky imaging performed with a JPL Delta-Doped detector to date.

3.8 Payload Rocket Environmental Tests

According to NASA's *Sounding Rocket Program Handbook*, payloads must be designed to account for mechanical loads, vibration, thermal, and vacuum environmental considerations of the launch and space environment. For example, sustained load factors exceeding 30 g's are often experienced during ascent, the vacuum environment of space can cause rapid overheating of electronics (the payload compartment is unpressurized) and outgassing of materials under vacuum can degrade performance of science measurements. Therefore, sounding rocket payloads are subject to an intense series of tests before they are approved for flight. For the CCD payload on CHESS, ASU was responsible for the completion of this testing and data collection before delivery to CU - Boulder. Vibration testing was carried out to the NASA Sounding Rocket Operations Contract (NSROC) standard for component level testing, low-outgassing, cleaning, and baking procedures were employed, and an operational vacuum test was conducted with all the CCD flight electronics.

3.8.1 Component Staking and Heat-Sinking

The thermomechanical structure of the camera system had to be carefully staked to ensure survival in the harsh launch environment. Even after applying torque specifications to all screws in the assembly the CU – Boulder team reported that they saw screws back out of threaded holes due to launch vibrations. Therefore, for its impressive tolerance to cryogenic temperatures and low-outgassing, 3M 2216 B/A epoxy was used. The epoxy was applied to each screw as well as the clamp that held the CCD to the copper cold structure. In the CCD cold structure of the payload there were also four aluminum legs that secured the copper cold structure in place via fiberglass clamps. There was concern that these for legs could potentially oscillate and transfer dangerous loads onto the delicate CCD pixel array, so additional stainless-steel safety wire was applied between the aluminum legs locking them into place.

Since all the CCD support electronics would also be exposed to the launch environment, they needed to be secured as well. Ideally, all PCBs would be conformally coated for launch, but for this project we did not have the experience or in-house ability to complete this process. Therefore, in lieu of conformal coating, on the heater circuit, Small-Cam, and preamp boards, any non-surface mount PCB components had 2216 epoxy applied to stake them in place. The RTD computer circuitry only included surface mount components but extra precaution was taken by mounting the CPU chassis on Barry Controls hi-damp silicone cup style mounts (this is actually a mil-spec standard mount that can accommodate any IDAN or PC/104 stacked system).

3.8.2 Vibration Testing

Orbital ATK in Phoenix generously donated the use of their facilities to conduct a vibration test on the payload. Vibration profiles were provided by Wallops NSROC and can be found in Table 11, which included random vibe, a sinusoid sweep, mechanical shock, and acceleration tests. It is worth noting that the NSROC vibration profile is 'component-level' and is harsher than what is recorded by rocket accelerometers in flight. This is to both to add margin and to account for amplified vibrations that the rocket chassis can impart onto payloads based on mounting scheme.

To accommodate the test fixture, work was done with the Orbital ATK vibration lab team to get mounting hole drawings and have them review my design before manufacturing. The design was a two-part L-bracket assembly made from half inch stainless-steel. The payload could then be mounted in the Z-direction (direction of motion parallel to the face of the CCD) or XY directions (two axes perpendicular to the face of the CCD) based on how it was positioned on the L-bracket. Figure 47 shows the payload on Orbital ATK's vibe bench in both configurations.

As part of the experimental setup, the Orbital ATK technicians glued accelerometers to the vibe bench surface (control), my mounting structure (to see if the structure itself was imparting additional shock to the payload, and the back end of the payload, opposite the CCD (tip of the payload's moment arm). The full NSROC component-level vibration profiles were carried out for the Z- and XY-directions of the payload. An example of the vibration data from the random vibe profile can be found in Figure 48.

Before the vibration test was conducted, a comprehensive series of pictures were taken of the payload interior and then the same series of pictures were taken after. No damage or changes to configuration were noted in the before and after comparison indicating a successful pass of vibration testing. The payload interior after testing can be seen in Figure 49. After integration the entire rocket will undergo a full rocket vibration test at Wallops Flight Facility.

3.8.3 Outgassing

Outgassing is a concern for any system undergoing high vacuum but was particularly critical to control for this project due to the sensitivity of the optics system. Volatiles trapped in materials are released and will tend to deposit on cold surfaces, which in the case of the CCD will be the cryogenically cooled pixel array. Any contamination threatens to act as a 'filter' and kill the UV QE of the detector (part of Table 9, high-level requirement 2). Therefore, under advisement from CU – Boulder and JPL, low-outgassing materials were carefully chosen, and all surfaces were cleaned with a combination of acetone and isopropyl alcohol any time the vacuum seal was broken, and the payload was opened in the lab.

In addition to these precautions, each screw or small metal component was bathed in isopropyl alcohol and sonicated to knock loose contaminants from any tough to clean surfaces such as on screw threads. Finally, as a rule, if the payload vacuum was broken and open to the lab for >4 hours, then it was re-baked in a vacuum oven (shown in Figure 50) at 200°C (IRlabs, 2004). This temperature and bake duration is to ensure that all hydrocarbons and water completely outgas from the material and are removed from the system by the oven roughing pump.

3.8.4 Vacuum Environmental Testing

The payload electronics compartment in the rocket is exposed to ambient pressure. Therefore, as the rocket passes through the upper parts of Earth's atmosphere and into space, the electronics compartment is essentially in a vacuum. A requirement from CU – Boulder was that it could be proven that the payload electronics could survive in a vacuum for at least 30 minutes (twice the data collection time and part of Table 9, high-level requirement 3).

The first action to take was to conduct an analysis of the electronics to get a first estimate of which electronics were in danger of overheating. The RTD computer comes heat sunk with chassis radiators, so this was not a concern. Also, the preamp circuits only draw ~200mA of current, so they were not big heat offenders. Regardless, the four preamp boards all have a preamp that is the warmest of any component, so a heat sunk was added by thermally epoxying it to the top of each of them with a copper link to the chassis of the preamp chassis.

However, the heater circuit board and the Small-Cam controller presented a real thermal challenge. Small-Cam was designed for lab use, so it had two fans attached to its chassis to circulate air and convectively cool its components. After detaching these fans (which would be useless above Earth's atmosphere), Small-Cam still drew ~1 amp and heated up rapidly. Using a FLIR camera (example data in Figure 51), the biggest thermal offenders were a series of DC-DC converters on the board used to provide the CCD with its +80 volt high voltage line as well as the video readout board which digitizes the CCD video signals with four ADCs (one per CCD quadrant readout) at a high clocking rate. This involved a tedious process of heat sinking components inside Small-Cam and then linking them to a common copper thermal braid that leads to the exterior of the chassis. Finally, the biggest thermal offender of the heater board was a MOSFET that produces the 1 amp heater current for the CCD whenever the Omega temperature controller sends a TTL signal. To mitigate this, the MOSFET was heat sunk directly to its box chassis (similar to the preamps).

After heat-sinking was complete, the entire electronics setup needed to be integrated into a vacuum chamber. To accommodate this test, time was granted in an existing vacuum chamber at ASU. To make the test possible a way to wire power to the electronics and temperature sensors through the chamber wall was designed. The only interface that could accomplish such a passthrough was a KF25 vacuum flange. To use this flange a DB25 hermetically sealed connector with KF25 flange termination was procured. Then two wiring harnesses could be constructed – one for the inside of the chamber and one for the exterior. These cables were first soldered together via wiring diagram and then tested in the lab with the feedthrough successfully.

As part of this cable assembly, 16 of 25 connections were dedicated to temperature sensors (two wires per sensor). For temperature sensing small 2x2mm sized RTD sensors were purchased. Their small size was key so that specific areas of PCBs or components could be targeted. Four sensors were dedicated to Small-Cam since it was the most at risk for overheating. Then, one sensor was placed on the heater board, one on the preamps, and two on the RTD boards. To measure temperature, a Lakeshore 336 temperature controller which can accommodate four inputs was used.

During the test the electronics were powered on during the pump-down of the chamber to simulate the rocket launch and started a timer for 30 minutes. The Small-

Cam sensors were exclusively monitored since it was the main unit of interest but a scan through of the other sensors at the 10 minute, 20 minute, and 30 minute mark was performed to make sure they remained within acceptable ranges. After 30 minutes Small-Cam heated up the most, as expected, and its hottest component reached 50°C. During the test the camera payload was also in the chamber, but with no CCD installed. The idea here was to take zero second exposures during the thermal test to see if noise performance was any different in the images. After a comparison of bias frames from room temperature lab tests and vacuum chamber bias frames, noise performance was not noticeably affected.

The test setup and chamber at ASU can be seen in Figure 52.

3.9 Flight Software

Software architecture of the payload was implemented to minimize complexity for CU – Boulder team. Upon power on, the Omega temperature controller was pre-programmed as a standalone unit to run a PID loop to control the CCD temperature to a -123°C CCD setpoint, sending TTL signals to activate the heater as necessary. The control of the CCD through Small-Cam was more complicated since the controller requires preloaded machine code 'timing files' which dictate bias voltage levels, vertical and serial register clocking schemes, and video gain settings. Astronomical Research Cameras (maker of Small-Cam) provides a C API library for software development, but this was further simplified through the use of a Python wrapper developed by the team at JPL. Functions from this Python CCD control code class were then imported into a script written for controlling the payload in flight.

The RTD computer was then hard-coded to boot directly to a command line that was running the flight script. The RTD was also designed to be accessed remotely via ethernet using ssh protocol. A code manual was delivered to CU – Boulder as part of the ICD, and the Colorado team was to use this existing code to add to the flight script several auto-imaging routines that could be run based on what developed with the rocket flight in real time. For instance the boot-up code would simply ask “enter a routine number” – routine #1 might be a ‘take bias frame’ command where the Small-Cam would take a zero second exposure with the CCD and display readout time remaining, routine #2 might be ‘take 20 second exposure’ where Small-Cam would command a 20-second integration including the opening of the CHESS shutter, etc.

3.10 Payload Delivery to CU – Boulder and QE Issues

After all the CU – Boulder thermal, mechanical, and software requirements were met, a representative from the Colorado group came to ASU to get first-hand experience with operating the equipment and help prepare the payload for shipment. An ICD was also put together that covered the operation of the RTD python interface, thermal system, and all power needs/cabling connections.

At ASU there was no access to FUV characterization of the CCD, so this was agreed to be done at CU – Boulder as a final step. The Colorado team received the payload and installed it to their UV vacuum characterization chamber, which utilizes a deuterium lamp and calibrated diode. The Colorado team’s QE characterization of the delivered payload can be seen in Figure 53. While the CU – Boulder results matched the QE results obtained across the visible spectrum at ASU, QE was an order of magnitude lower than expected across the FUV range (~30% expected, ~3%

measured). This reduction in FUV QE was unfortunately deemed unacceptable for flight. Despite careful efforts to use low-outgassing materials, deep cleaning, and vacuum oven baking, during an investigation to the root cause of the contamination, an unused screw hole on the payload structure interior (machining error during manufacture that was deemed safe to fly) appeared to have a small amount machine shop grease residue trapped in its threads.

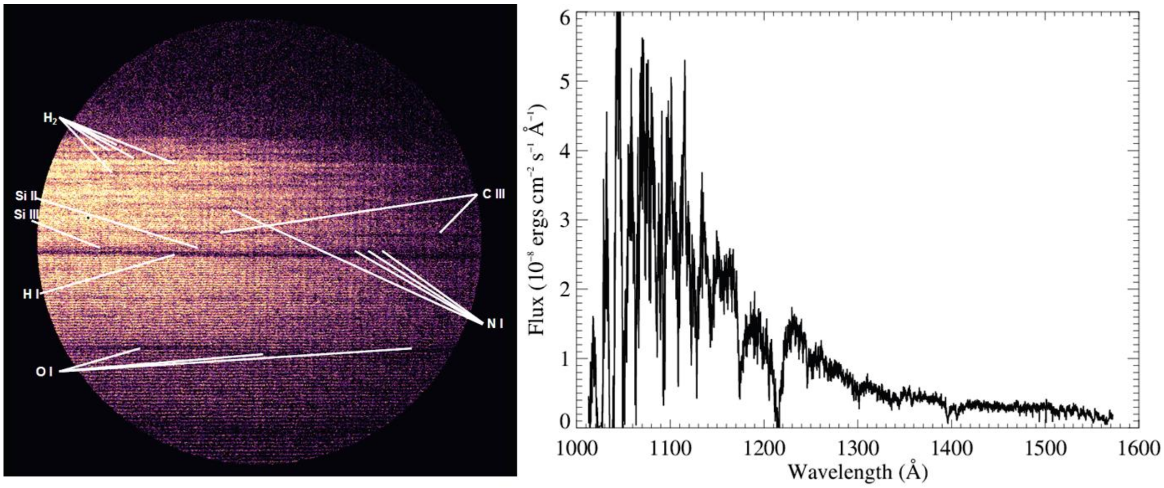

Figure 28. Spectral Data from a previous CHESS flight (Hoadley, 2017)

The left image shows spectra from the CHESS echelle being imaged by an MCP detector in flight. The plot shows a flux calibrated 1D spectrum.

Figure 29. CHESS Structure Ready for Attachment to Black Brant IX Rocket

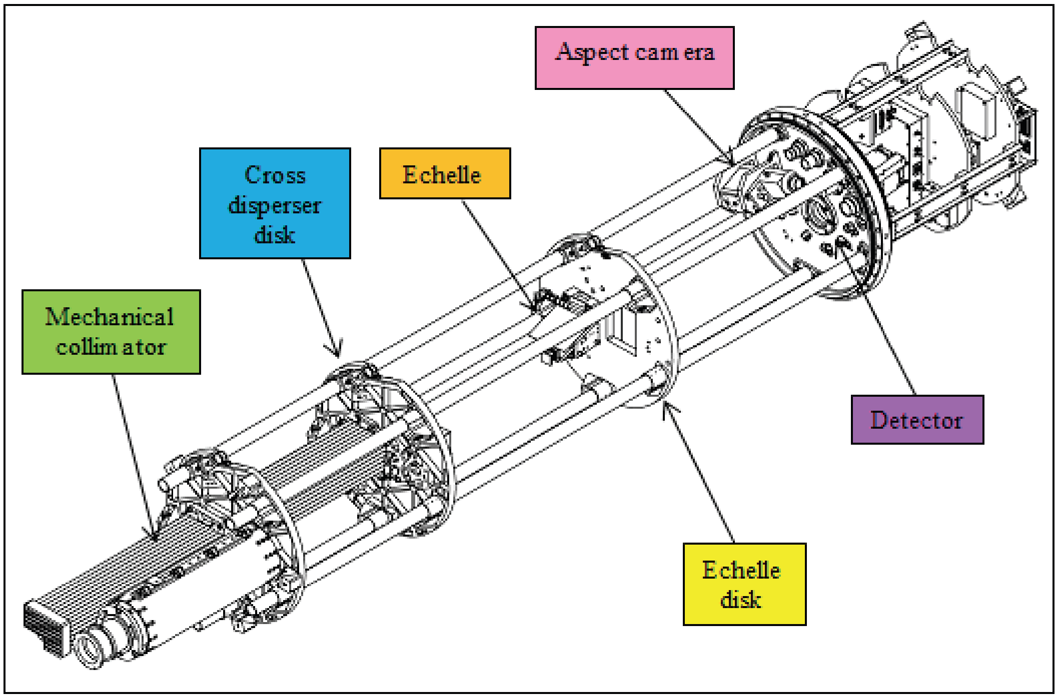

Figure 30. CHESS Rocket Cutaway (Hoadley, 2017)

The focal plane payload is mounted to the flange labeled 'Detector.' Before flight everything on the echelle and detector side of the rocket compartment are pre evacuated to prevent contamination. After launch, the electronics that sit behind the payload are exposed to the vacuum of space as the cabin is unpressurized.

Table 7. CHESS Science Traceability Matrix

Scientific Objective	Scientific Measurement Requirements		Technical Requirements		Instrument Specifications	Instrument Requirement
	Targets	Observation Technique	Type	Parameter		
Using UV spectroscopy to characterize the Local Interstellar Medium (LISM)	LISM translucent cloud atomic, molecular, and three-dimensional ionization features	Spectroscopy	Spectral	Bandpass	100--160nm	UV-Optimized Spectrograph
				Resolving Power $R = \frac{\lambda}{\Delta\lambda}$	R ~ 150,000	
		High throughput imagery	Photometry	Minimum SNR	20 (+/- 5)	DQE across FUV bandpass of 30%, and read noise <=15e^-
				Exposure Time	40sec	
		Suborbital Altitude	Flight Profile	Detector Readout Time and CPU reboot time	<=20sec	Detector and CPU short readout time to ensure all targets are imaged, vacuum-tolerant electrical system
				Thermal Environment	Electronics survive vacuum of space for ~30min	

This table breaks down the CHESS FUV observing science objective into a series of targeted measurements of the LISM. These are further described and flowed down into instrument requirements

Table 8. CHESS Echelle Spectrograph Specs (France, 2012)

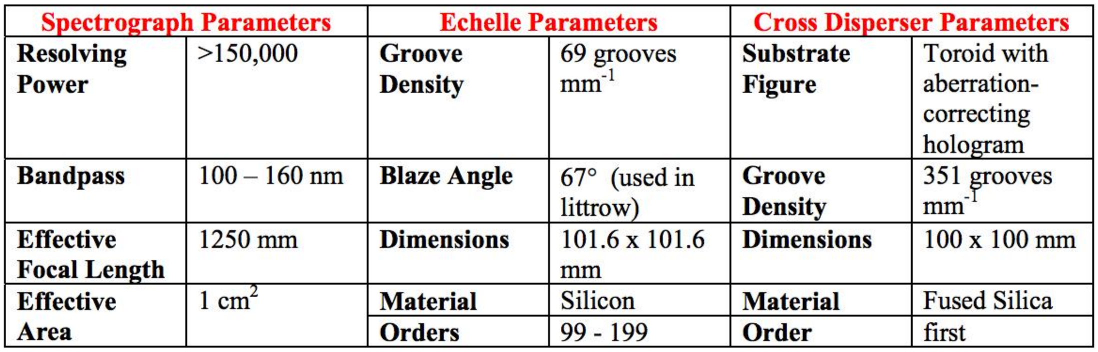

Spectrograph Parameters		Echelle Parameters		Cross Disperser Parameters	
Resolving Power	>150,000	**Groove Density**	69 grooves mm^{-1}	**Substrate Figure**	Toroid with aberration-correcting hologram
Bandpass	100 – 160 nm	**Blaze Angle**	67° (used in littrow)	**Groove Density**	351 grooves mm^{-1}
Effective Focal Length	1250 mm	**Dimensions**	101.6 x 101.6 mm	**Dimensions**	100 x 100 mm
Effective Area	1 cm^2	**Material**	Silicon	**Material**	Fused Silica
		Orders	99 - 199	**Order**	first

The CHESS echelle combines excellent resolving power with low scattering to provide photon limited sensitivity across the 100-160 nm bandpass.

Table 9. CHESS High Level Requirements

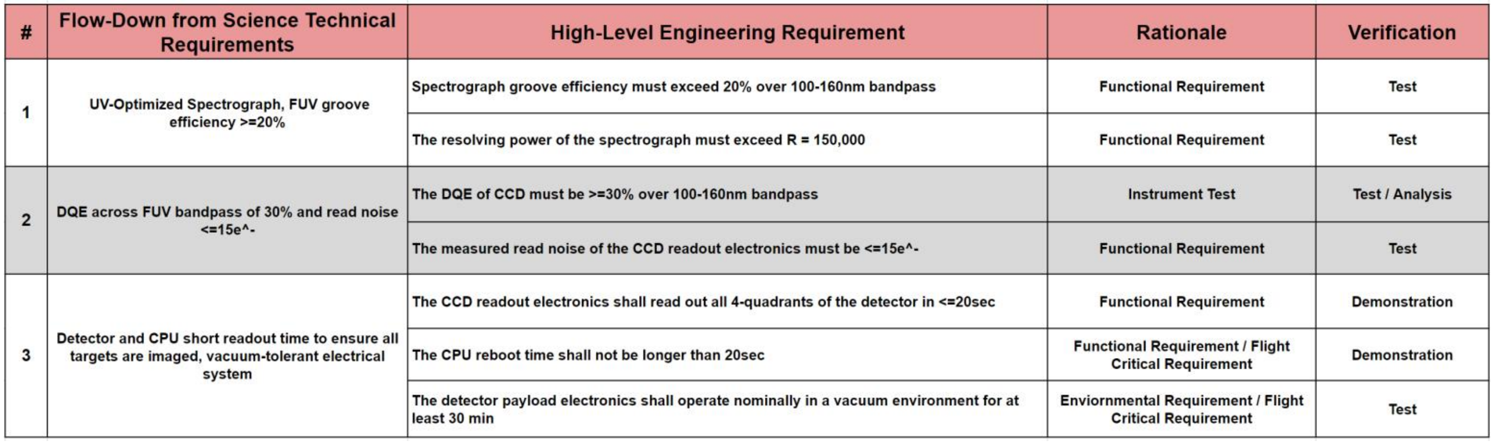

#	Flow-Down from Science Technical Requirements	High-Level Engineering Requirement	Rationale	Verification
1	UV-Optimized Spectrograph, FUV groove efficiency >=20%	Spectrograph groove efficiency must exceed 20% over 100-160nm bandpass	Functional Requirement	Test
		The resolving power of the spectrograph must exceed R = 150,000	Functional Requirement	Test
2	DQE across FUV bandpass of 30% and read noise <=15e^-	The DQE of CCD must be >=30% over 100-160nm bandpass	Instrument Test	Test / Analysis
		The measured read noise of the CCD readout electronics must be <=15e^-	Functional Requirement	Test
3	Detector and CPU short readout time to ensure all targets are imaged, vacuum-tolerant electrical system	The CCD readout electronics shall read out all 4-quadrants of the detector in <=20sec	Functional Requirement	Demonstration
		The CPU reboot time shall not be longer than 20sec	Functional Requirement / Flight Critical Requirement	Demonstration
		The detector payload electronics shall operate nominally in a vacuum environment for at least 30 min	Enviornmental Requirement / Flight Critical Requirement	Test

These instrument requirements flow down from the science requirements of the CHESS FUV spectral targets, but also flow down from the necessity for the focal plane payload to survive the harsh launch a vacuum environment experienced on sounding rocket flights

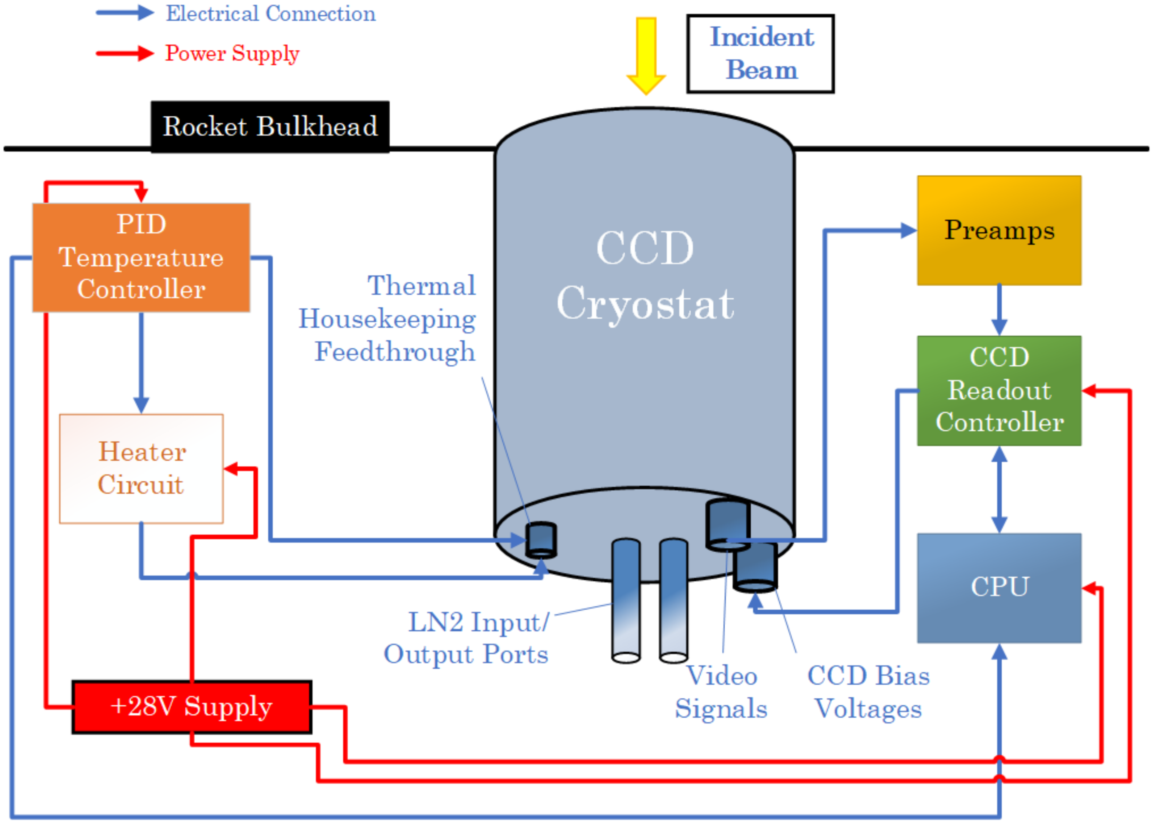

Figure 31. CHESS CCD Payload Block Diagram

The focal plane payload design is its own self-contained CCD imaging system that only requires a +28V input from the rocket power system. The CPU interfaces via ethernet to the rocket flight computer to command images and downlink data in flight.

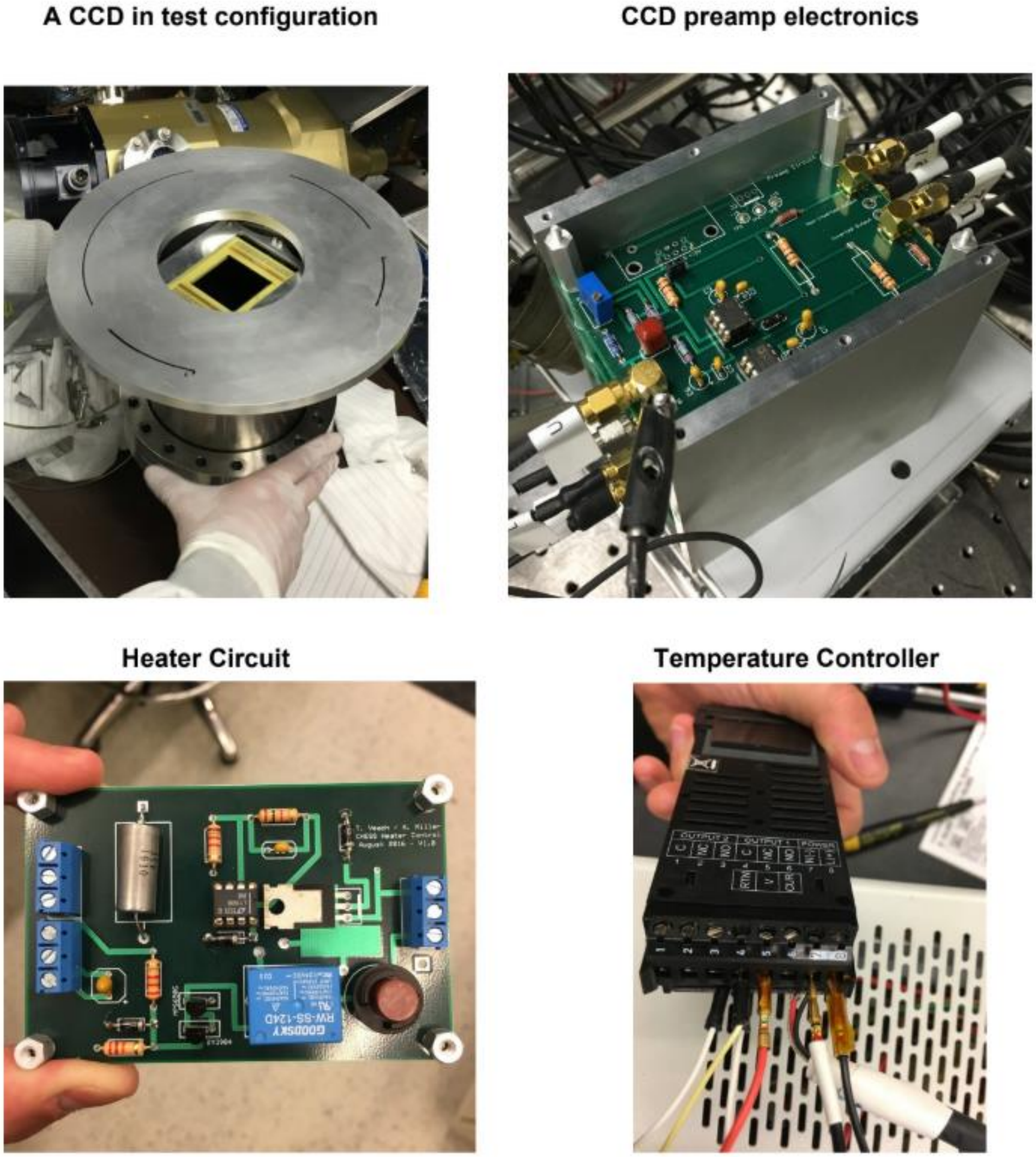

A CCD in test configuration

CCD preamp electronics

Heater Circuit

Temperature Controller

Figure 32. Detector Payload Components, cont.

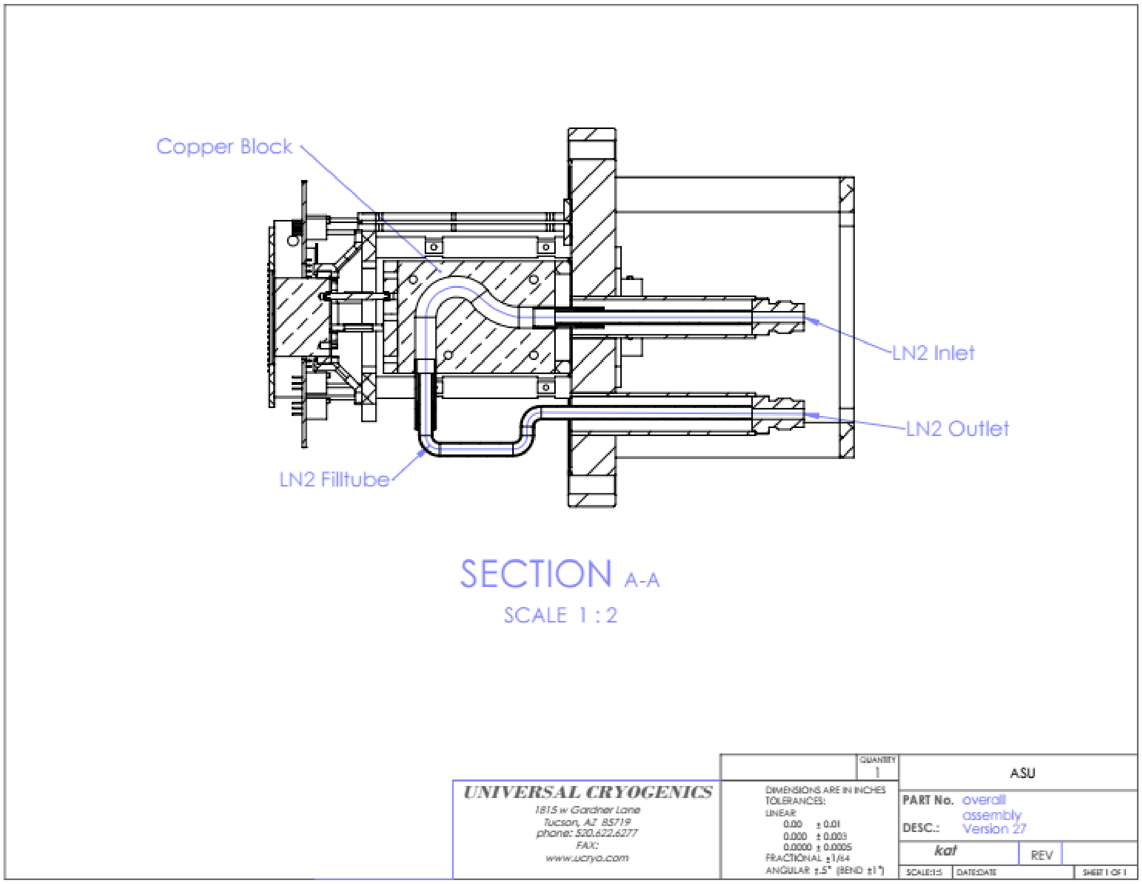

Figure 33. Thermal Cooling Loop Design

In this design an umbilical is attached to the rocket that circulates liquid nitrogen through the ‘LN2 Filltube.’ This circulation cools down a copper structure coupled to the CCD so that the CCD can reach its operating temperature. After launch the umbilical pulls away thereby ending the liquid nitrogen cooling circulation. However, since the rocket flight is so short, tests show the detector will only warm up a couple of degrees which has a negligible impact on performance.

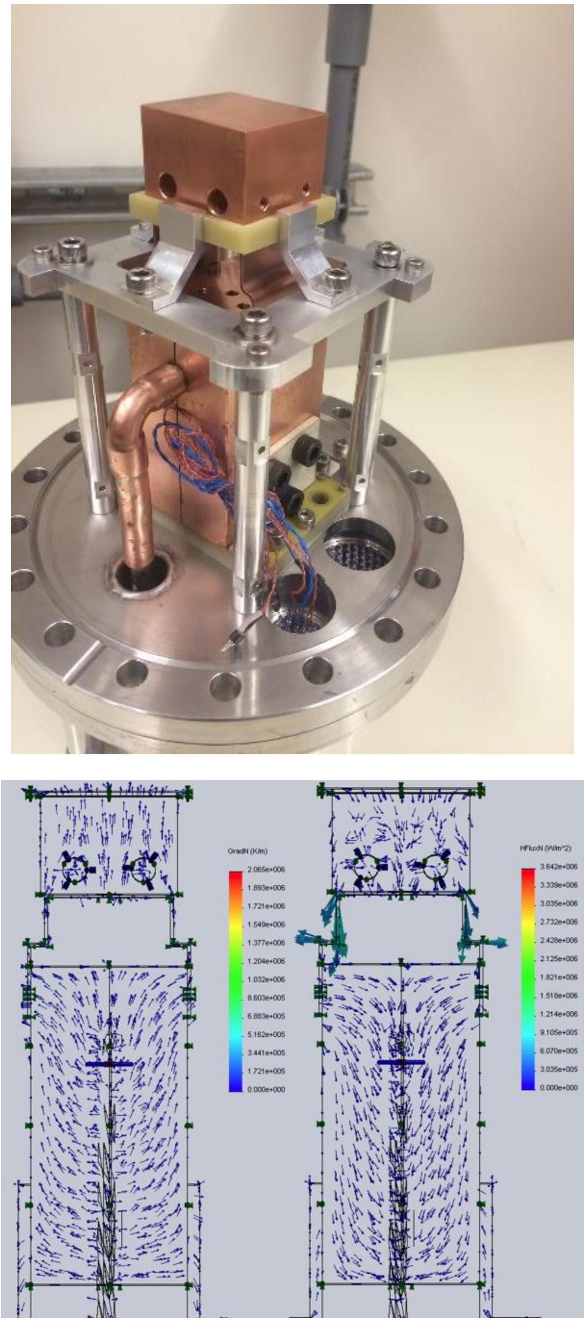

Figure 34. Cold Structure Thermal Analysis (Veach, 2012)

The mechanical structure is essentially a support structure to ensure that the CCD copper cooling structure remains stable during the high G loading of rocket launch.

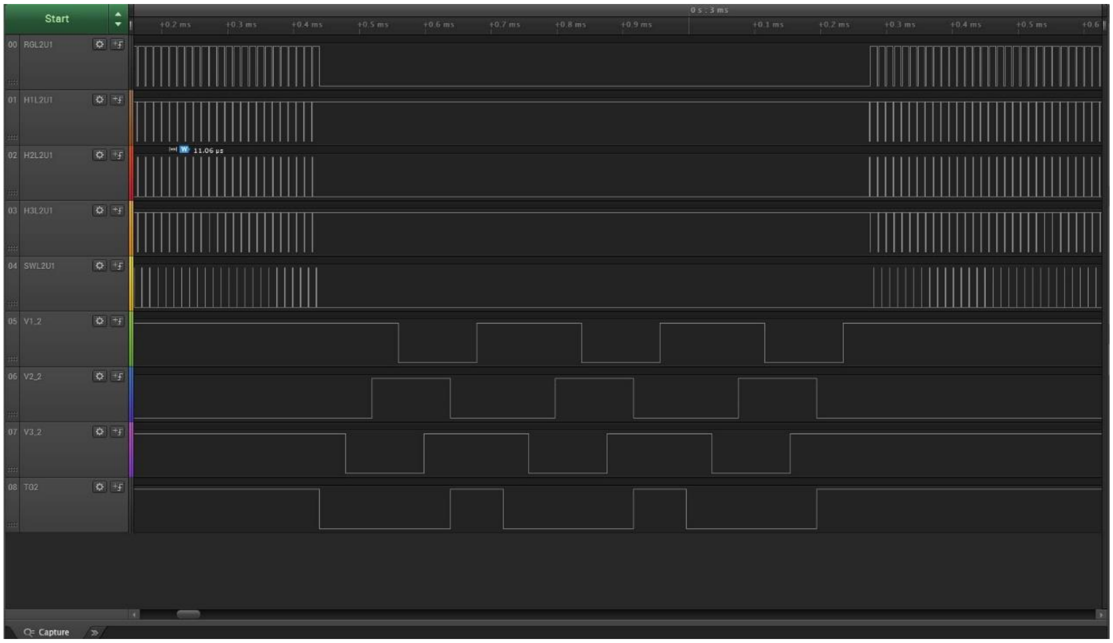

Figure 35. Logic Analyzer Characterization of CCD Clocks

The first five channels from the top show reset pulse, three-phase serial clocks, and summing well. The lower four channels which have longer periods, show three-phase vertical clocks and the transfer gate.

Small-Cam

RTD CPU

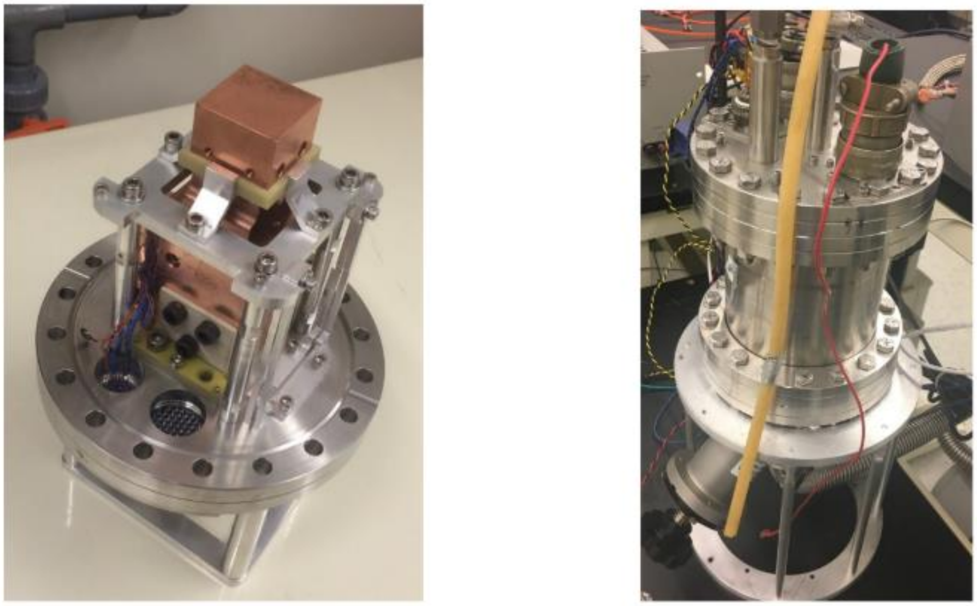

Thermomechanical structure

Payload 'tube' with vacuum valve attached

Figure 36. Detector Payload Components

Table 10. RTD Computer Specifications

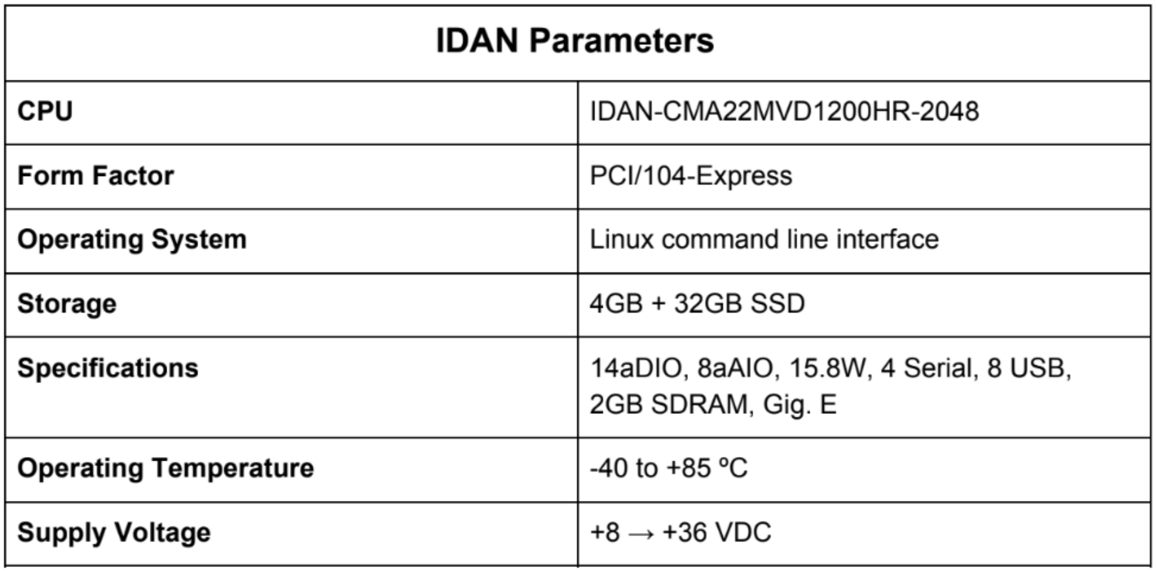

IDAN Parameters	
CPU	IDAN-CMA22MVD1200HR-2048
Form Factor	PCI/104-Express
Operating System	Linux command line interface
Storage	4GB + 32GB SSD
Specifications	14aDIO, 8aAIO, 15.8W, 4 Serial, 8 USB, 2GB SDRAM, Gig. E
Operating Temperature	-40 to +85 ºC
Supply Voltage	+8 → +36 VDC

The RTD IDAN stack was chosen as it is ruggedized by the manufacturer, comes with vibration dampening mounts to lessen launch loading, has an excellent thermal range, can operate on a variety of input voltages (rocket battery voltage varies over the flight), and has enough on-board storage to save all of the CCD raw science frames.

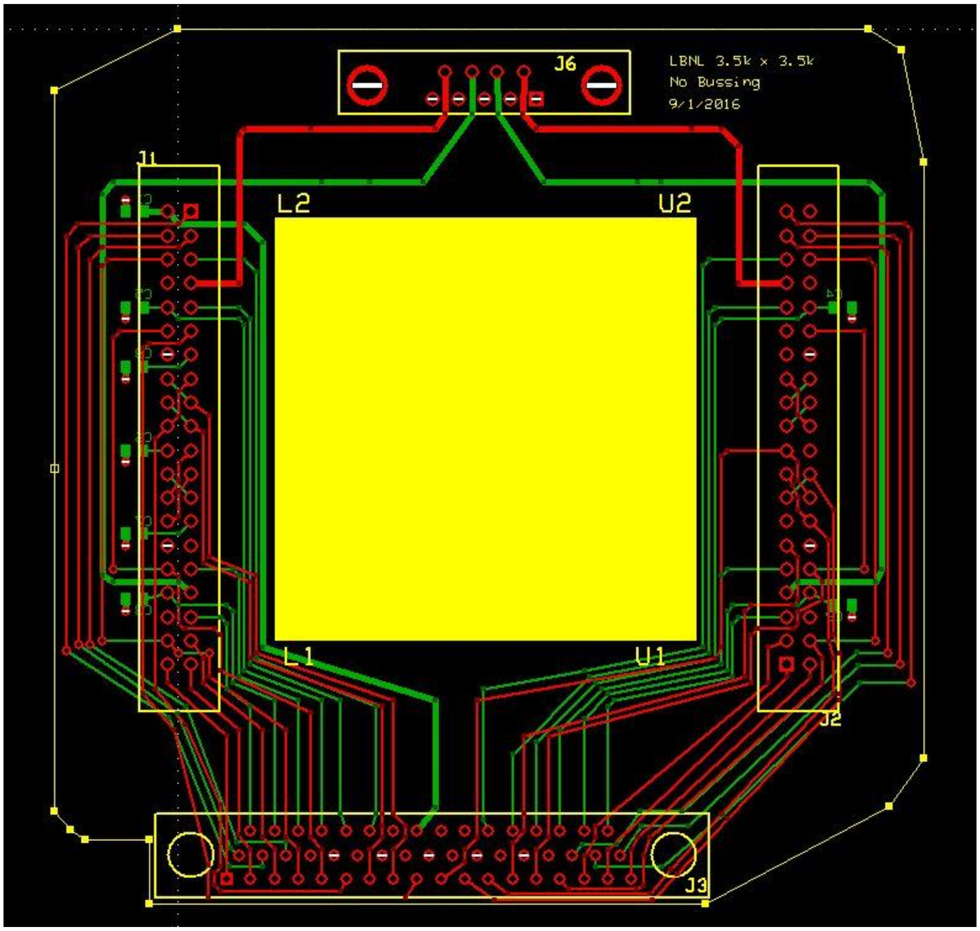

Figure 37. Custom PCB Design

This was a PCB designed to interface the JPL CCD with the interior electronics of the payload. The large yellow square shows a cutout region of the PCB where the copper cold head pushes through to contact the back of the CCD for cooling.

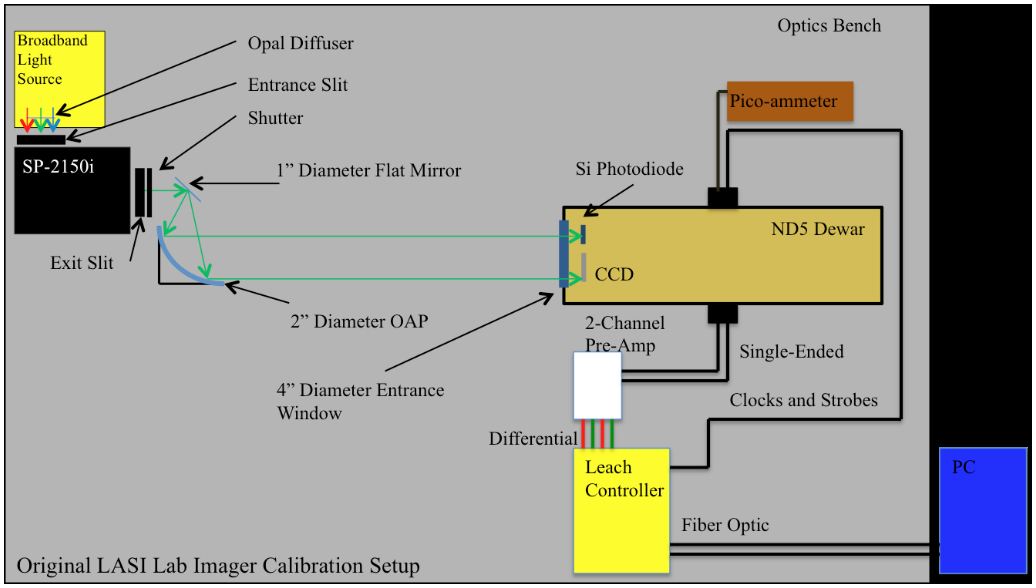

Figure 38. LASI Detector QE Measurement Diagram (Veach, 2012)

The detector of interest and a NIST calibrated diode are illuminated by the output of a monochromator light source. A reading of the NIST diode and an exposure with the detector are taken in steps across the bandpass of interest. For final QE calculation, the NIST diode is used to remove the uneven response functions of the monochromator light source to understand the true photon collection efficiency of the detector per wavelength.

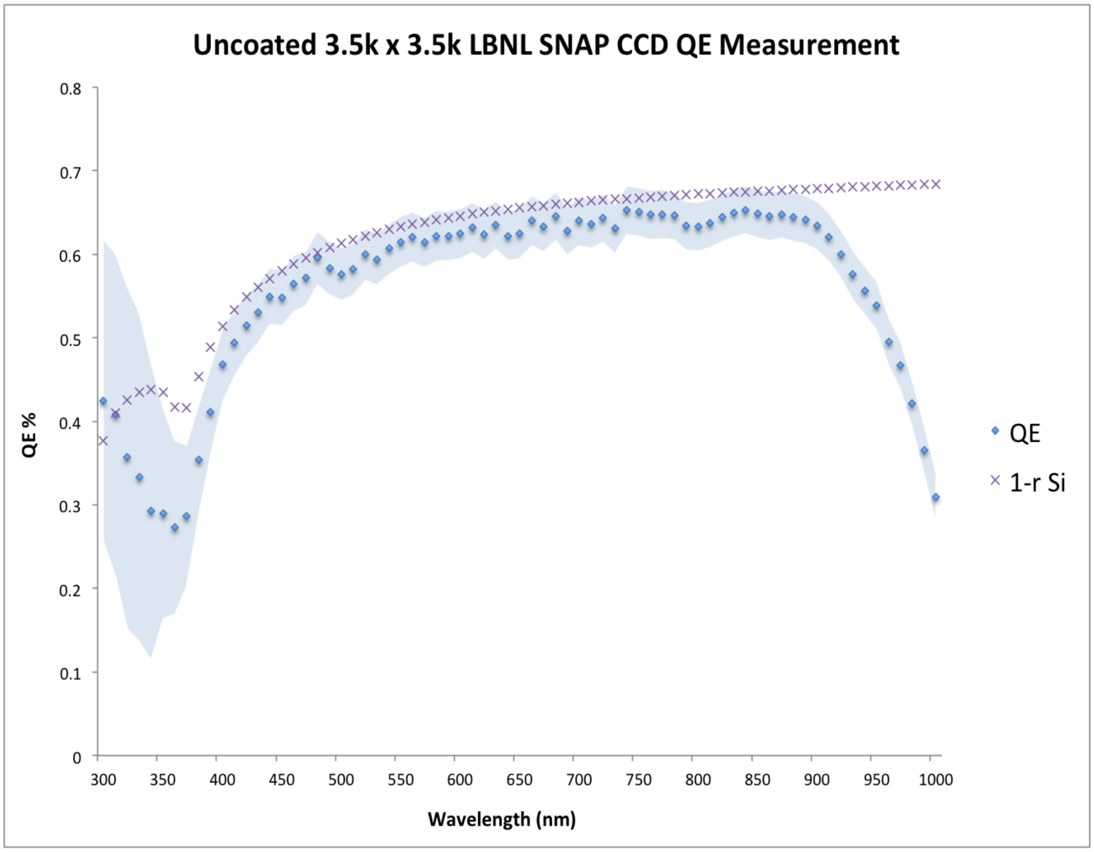

Figure 39. Flight CCD QE Measurement

The CCD provided by JPL for the CHESS mission was uncoated (no anti-reflection, AR, coating) since AR coatings tend to absorb FUV wavelengths. The QE curve nicely lines up with the maximum QE due to the reflective limits of bare silicon.

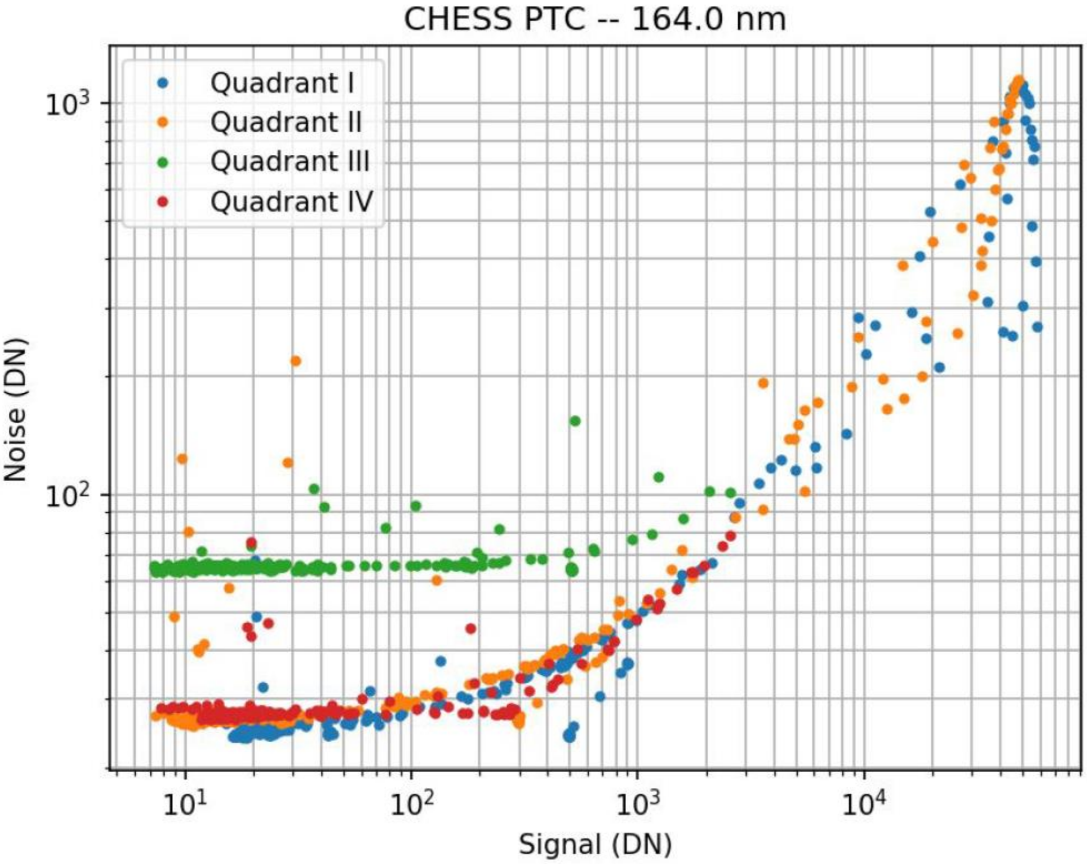

Figure 40. Flight CCD PTC Measurement

This plot correlates to a full pixel well of ~130,000 e^-/pixel and a read noise of <15 e^- per quadrant. Notice that quadrant III (green) was known to be noisier than the other three readout quadrants. The cause of this extra read noise was unknown but within limits.

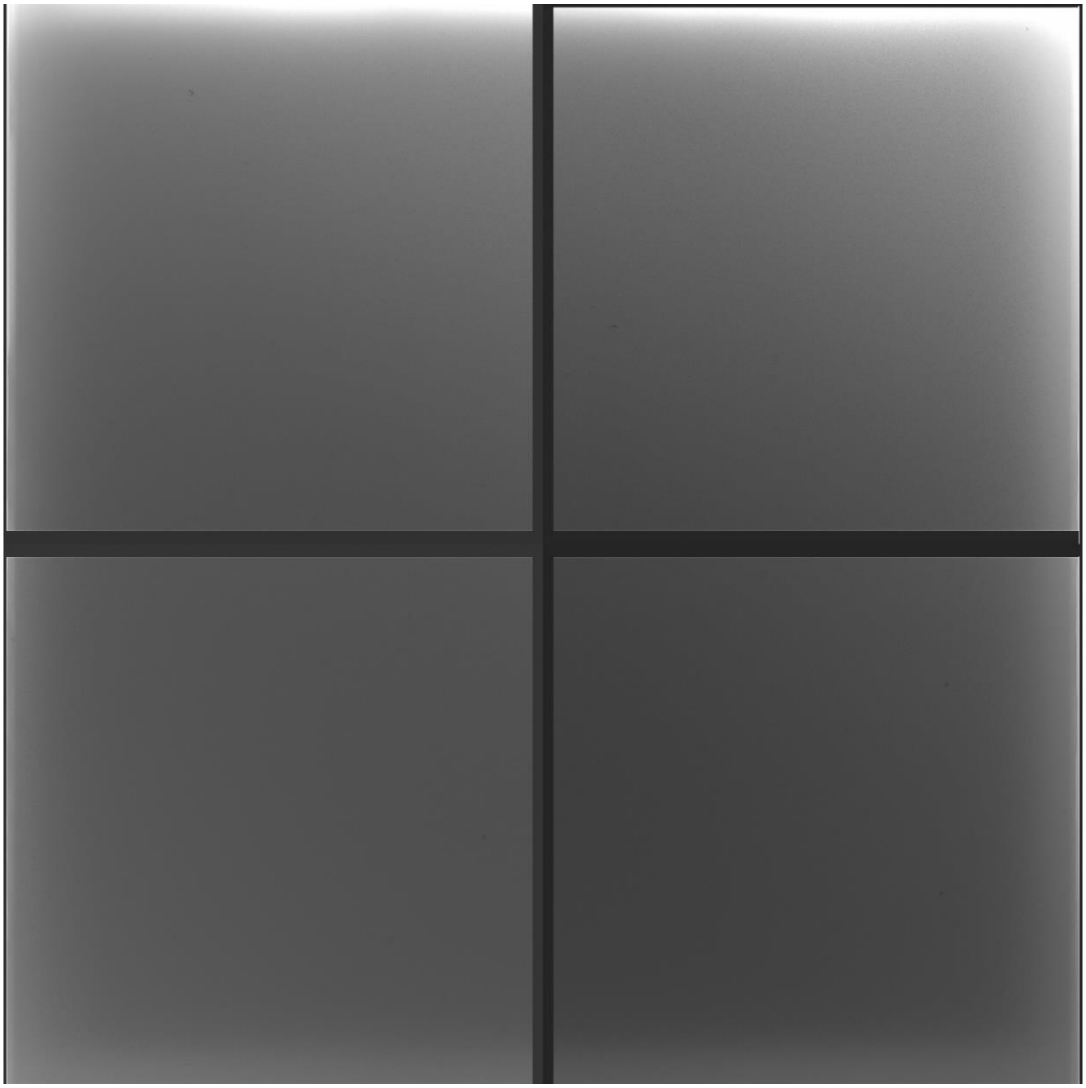

Figure 41. Flat-Field LBNL SNAP 4-Quandrant CCD

The dark regions in the middle and along the edges of each quadrant are overscan regions pre-programmed into the readout scheme of the image formation. These flats were used to measure read noise.

Figure 42. JPL AR-Coated CCD and associated electronics on the Kuiper 61” Telescope

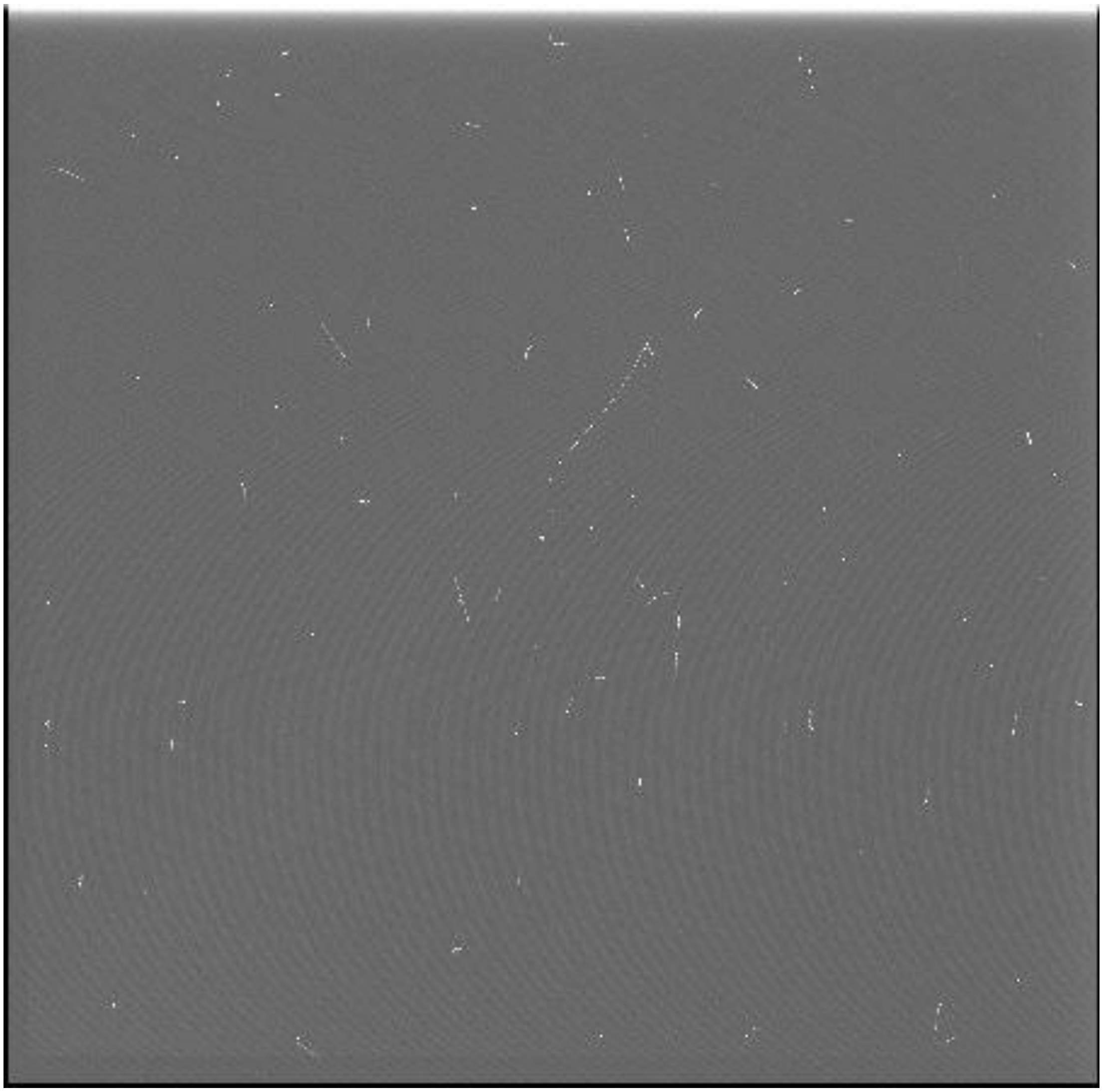

Figure 43. 300 Second Dark Frame Showing Several Cosmic Ray Interactions

LBNL devices are known to be susceptible to cosmic rays and extra steps were taken to subtract these from imaging frames.

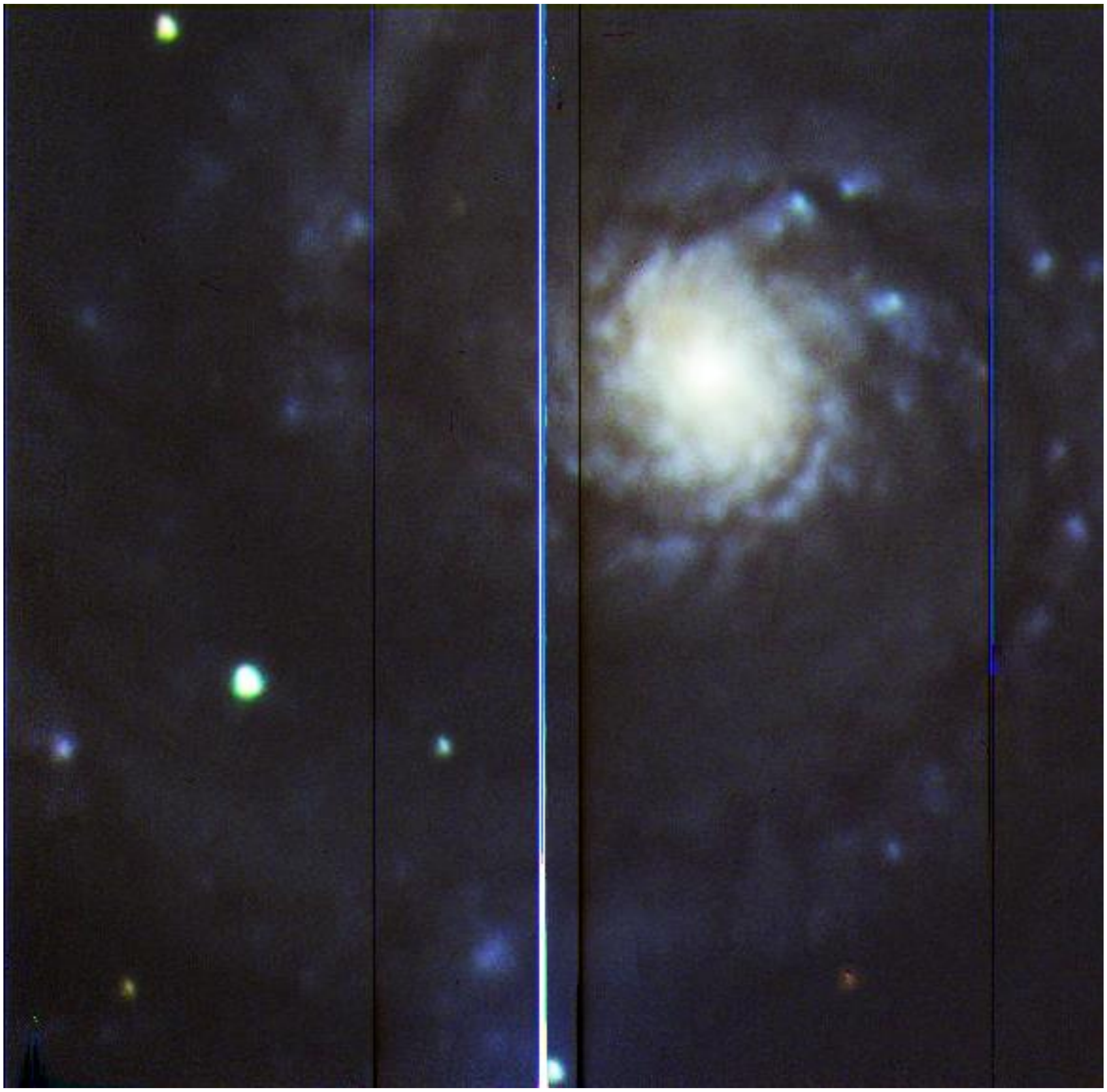

Figure 44. M51 Whirlpool Galaxy

The JPL device tested at the observatory was engineering-grade and suffered from several large cosmetic defects that show up as light and dark bands in the final RGB combined images.

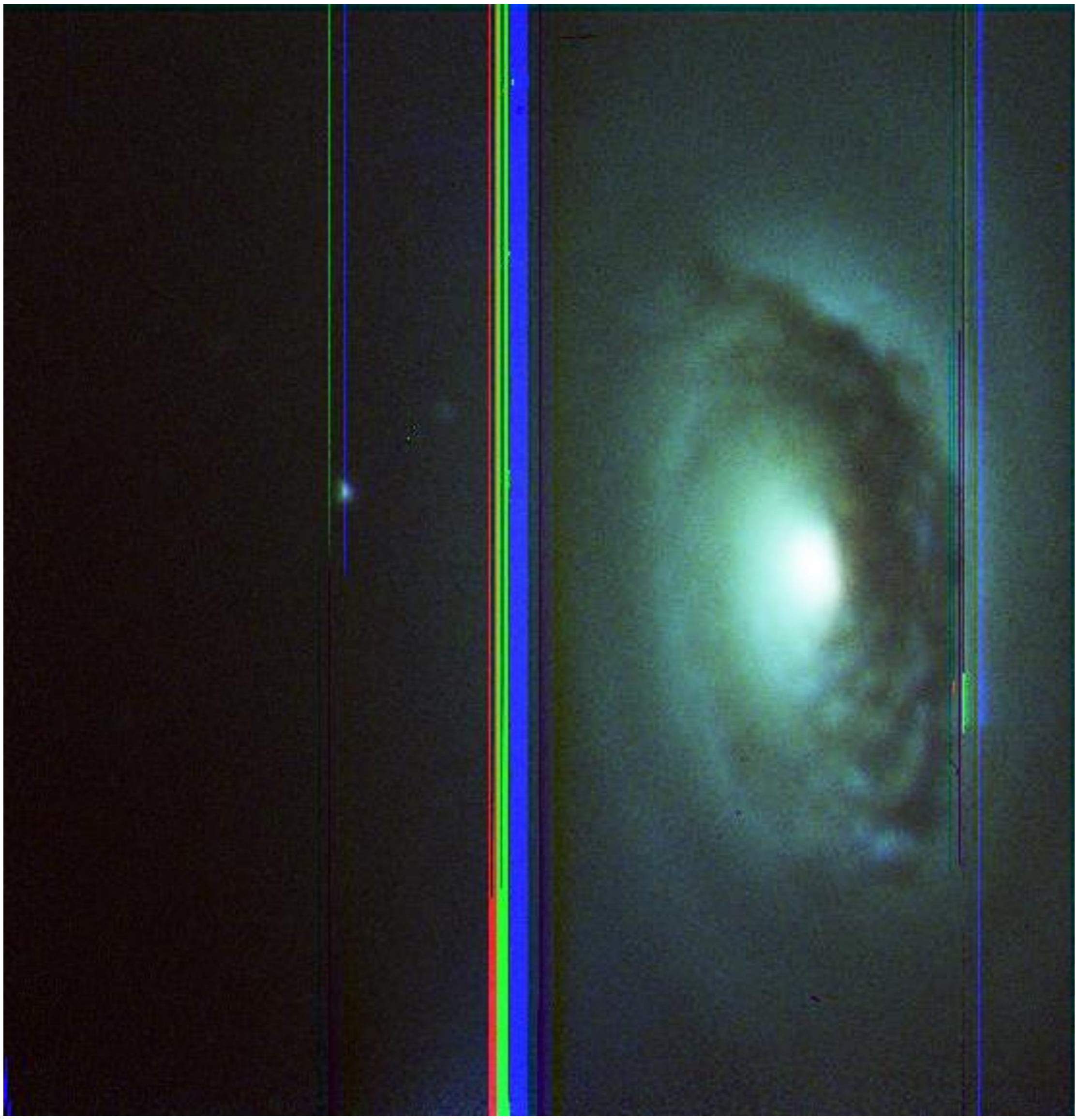

Figure 45. M64 Black Eye Galaxy

The JPL device tested at the observatory was engineering-grade and suffered from several large cosmetic defects that show up as light and dark bands in the final RGB combined images.

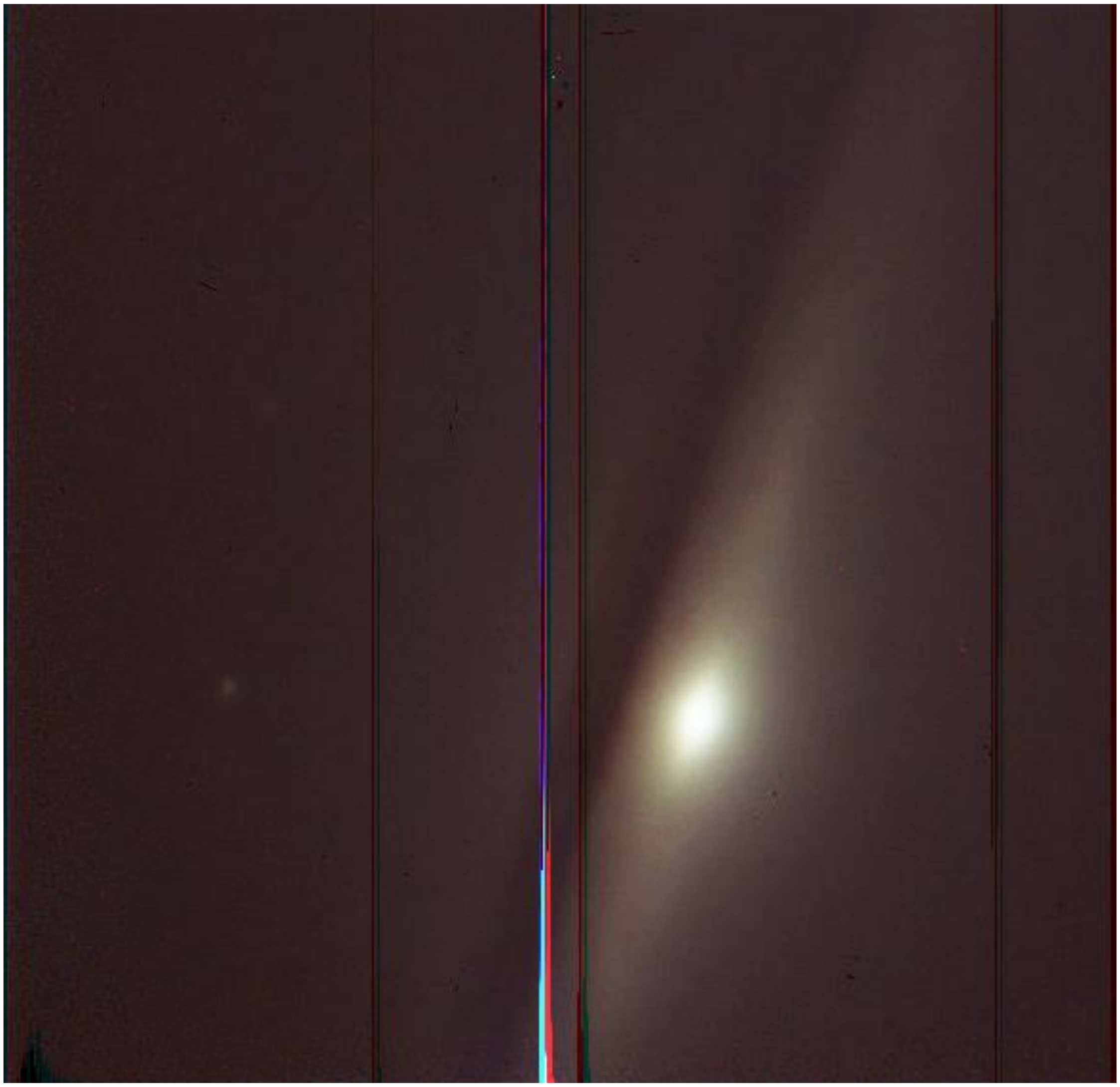

Figure 46. M104 Sombrero Galaxy

The JPL device tested at the observatory was engineering-grade and suffered from several large cosmetic defects that show up as light and dark bands in the final RGB combined images.

Table 11. NSROC Component-Level Vibe Parameters

NSROC Component-Level Vibe Parameters	
47. **Random Vibration – Duration: 20sec/axis – Spectrum: 20.4 grms**	
0.115 g^2/Hz	20 Hz
0.225 g^2/Hz	1000 Hz
0.225 g^2/Hz	1000-2000 Hz
2. Sine Vibration – Sweep Rate: 4 oct./min.	
7.30 in./s	5-89 Hz
10.5 g	89-800 Hz
15.0 g	800-2000 Hz
3. Mechanical Shock – 60g square wave (half-sine) – Duration: 6 milliseconds	
4. Acceleration – 60g's each axis	

Component-level vibration parameters for testing instrumentation outside of the final integrated rocket. Random vibrations, a sinusoidal sweep, and high-G mechanical shocks are all imparted onto the payload to ensure it will survive the rigors of launch.

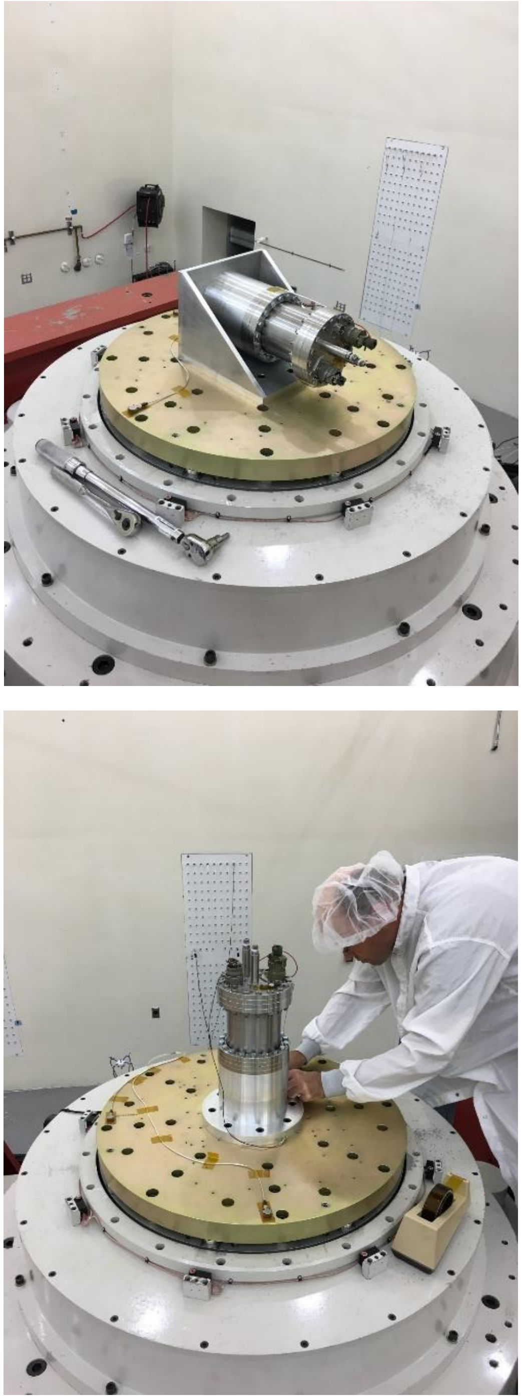

Figure 47. Payload Vibration Testing at Orbital ATK Facility

A test fixture was designed and implemented to allow the payload to be mounted in an axial and coaxial orientation.

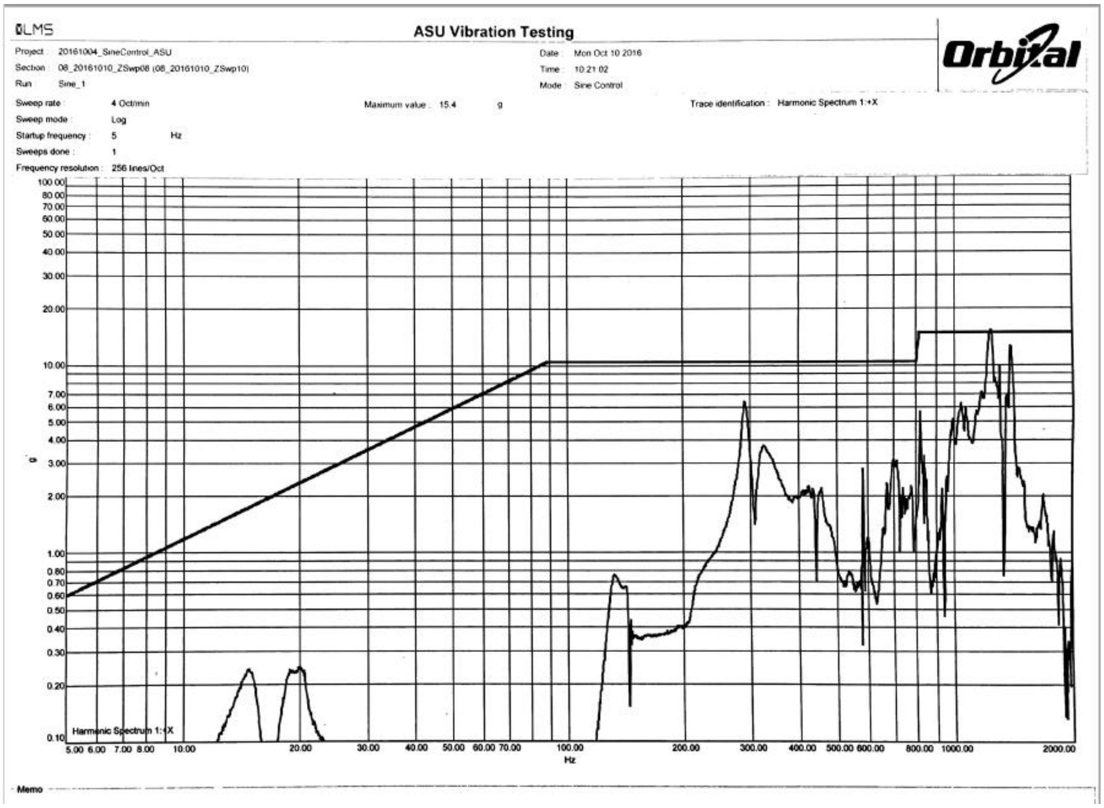

ASU Vibration Testing

Project : 20161004_SineControl_ASU
Section : 08_20161010_ZSwp08 (08_20161010_ZSwp10)
Run : Sine_1
Date : Mon Oct 10 2016
Time : 10 21 02
Mode : Sine Control
Sweep rate : 4 Oct/min
Sweep mode : Log
Startup frequency : 5 Hz
Sweeps done : 1
Frequency resolution : 256 lines/Oct
Maximum value : 15.4 g
Trace identification : Harmonic Spectrum 1:+X

Memo

Figure 48. Accelerometer Data from Orbital ATK Vibe Test

This plot is an example data product from Orbital ATK's vibe facility. As designed, payload resonances were constrained to higher frequencies.

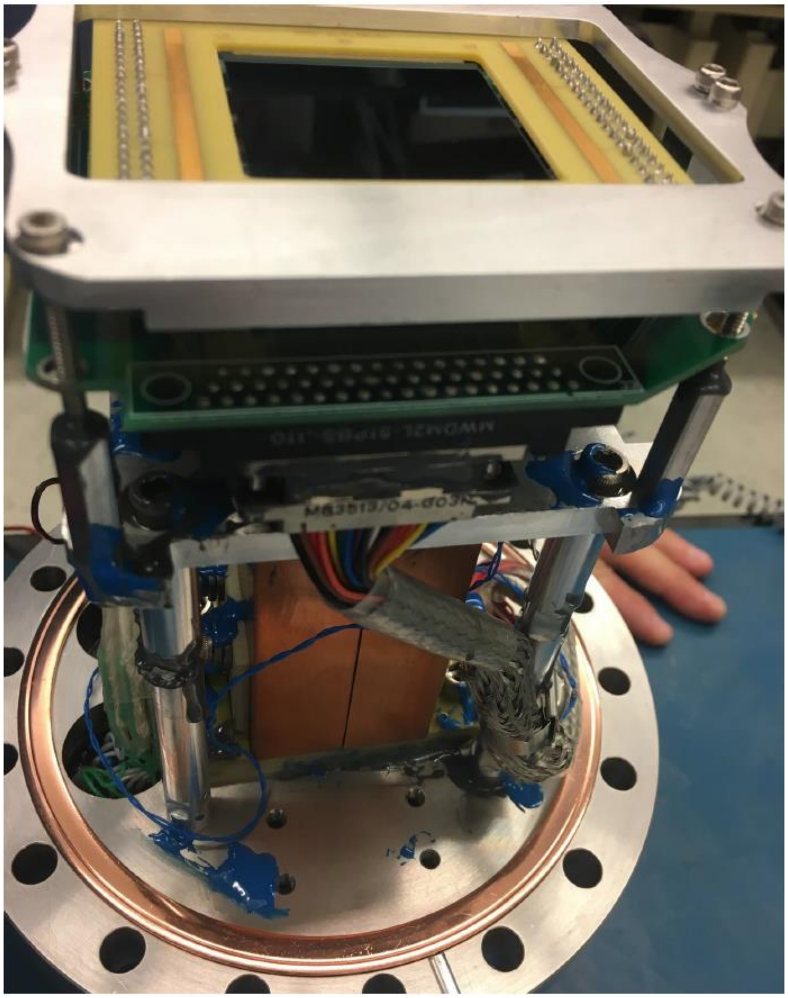

Figure 49. Post Vibration Test Detector Assembly

This was one of the pictures taken after the Orbital ATK vibration testing showing that the focal plane structure or detector suffered any damage. The blue substance seen in the image is low-outgassing epoxy used to stake parts of the structure.

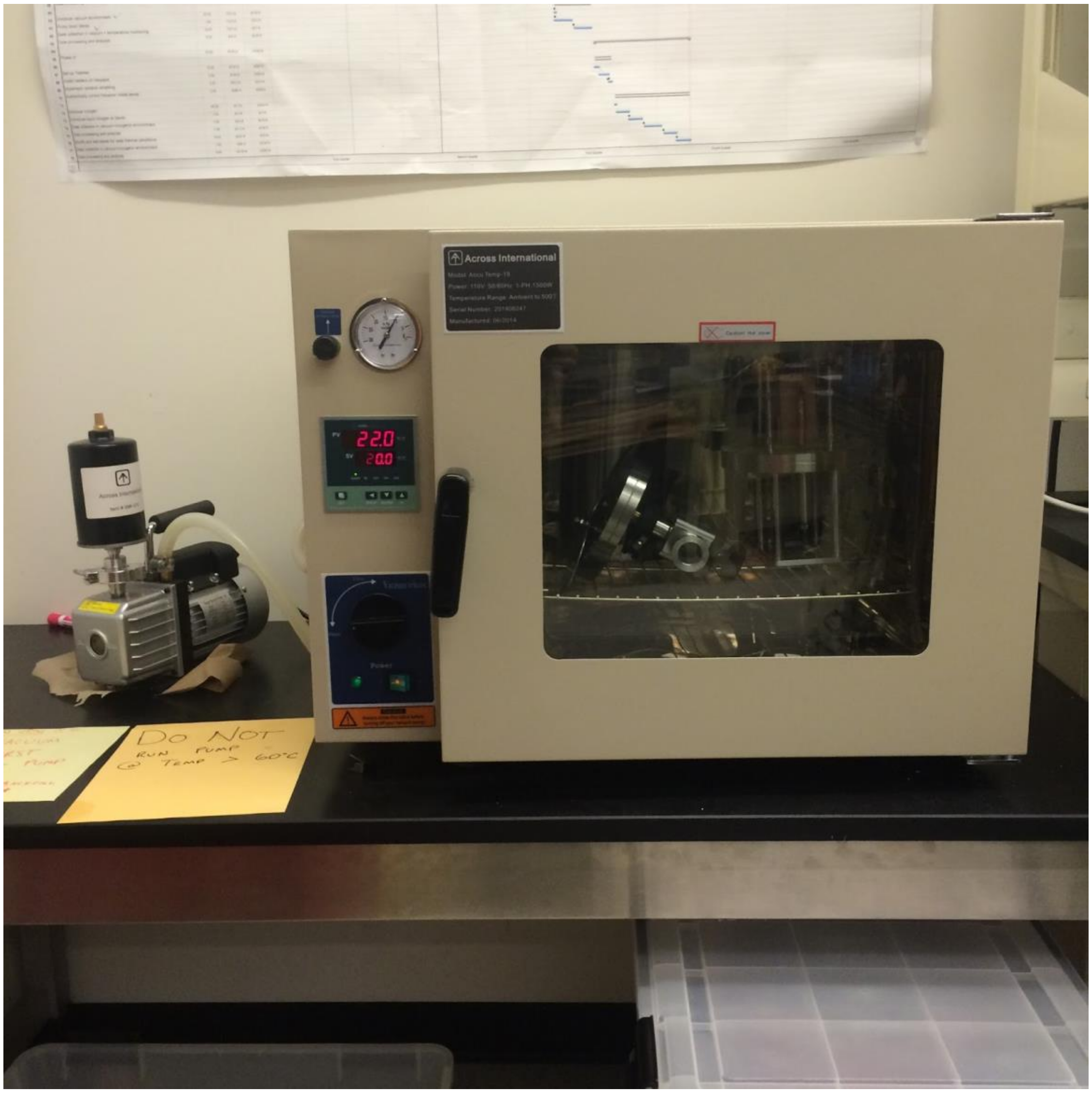

Figure 50. Vacuum Oven

After deep cleaning and sonication with ultra-pure isopropyl alcohol and acetone, the payload cryostat was baked in a vacuum oven to remove additional volatiles.

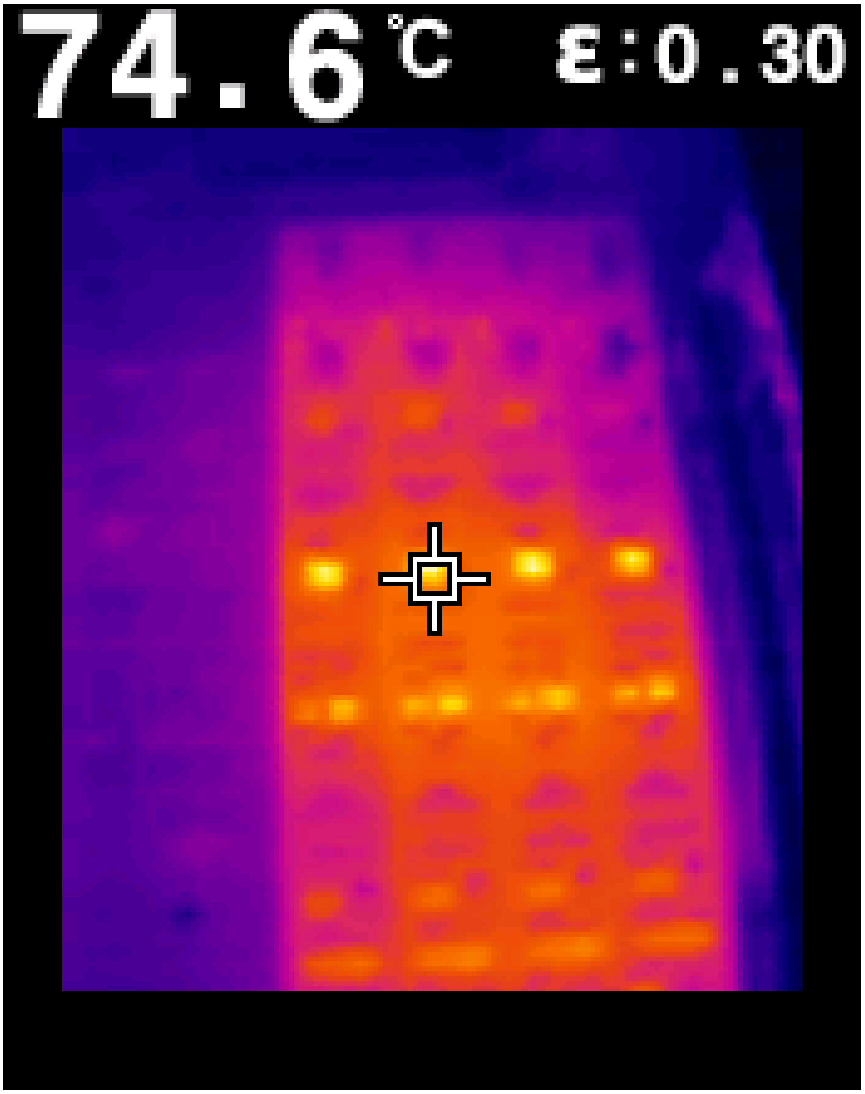

Figure 51. Hot-Spot Characterization of Payload Electronics

A far-infrared sensor was used to identify hot spots on flight electronics to assist with designing the heat-sinking scheme.

Figure 52. Vacuum Chamber Testing of Payload Electronics

A custom feedthrough was designed to operate the payload electronics in a flight configuration. The chamber interior was used to dissipate heat from the instrumentation. In flight the rocket interior structure would be used for dissipation.

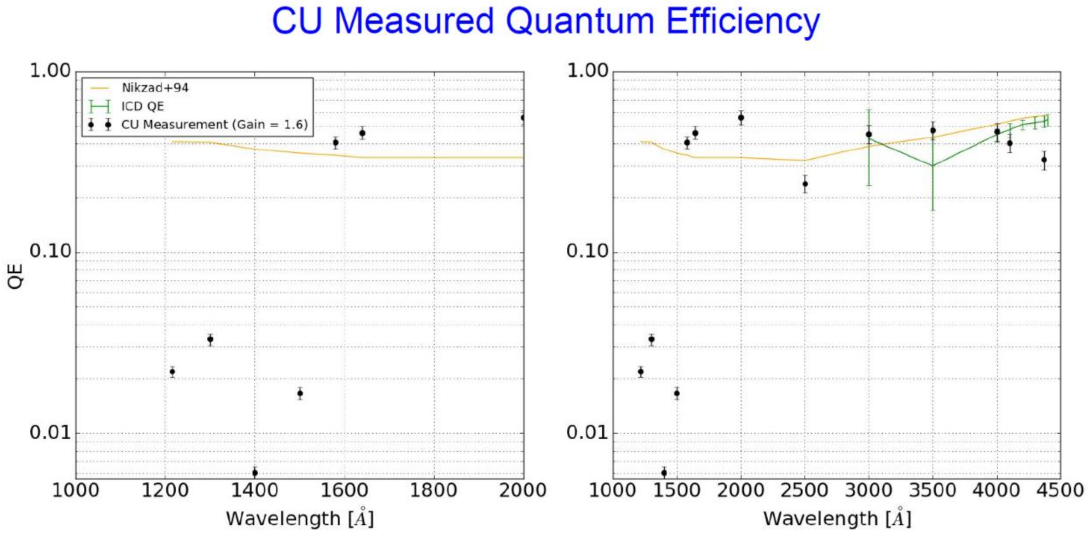

Figure 53. CU – Boulder Measured QE of Flight CCD Showing Decreased FUV Response

Characterization of the flight detector in Boulder showed QE response that matched well with measurements taken at ASU. However, response across the FUV bandpass was an order of magnitude lower than what was required for flight (~3% instead of the expected ~30%).

4 HEXAPOD RESOLUTION ENHANCEMENT SYSTEM (HERESY) – OBSERVATORY CONFIGURATION

4.1 Background

Light emitted from distant astronomical targets toward Earth travels many millions of miles in pure form until the final several miles upon encountering the upper layers of Earth's atmosphere where it is scattered, distorted, and/or absorbed. The challenges that atmospheric distortion presents to ground-based astronomy has been well characterized for over a century and, as a result, almost every major observatory around the world now employs some form of adaptive optics (AO) or image stabilization system. The most advanced observatories eliminate nearly all atmospheric distortion through the high-speed imaging of natural guidestars artificial laser points reflected in the atmosphere, mapping the incoming wavefront, and then deforming a mirror in the beam path to precisely cancel out waveform imperfections. The final image captured at the telescope focal point is then a complete reconstructed image of the original wavefront that restores much of the detail and resolution that would typically be lost without an advanced AO system.

Many AO systems also have a first order fast-steering mirror (FSM) or tip-tilt optic which does not correct for wavefront distortion but rather corrects for a pointing error signal caused by light being refracted by the atmosphere. This method does not restore the clarity of resolution accomplished by deformable mirrors, but in this case as the incoming wavefront is 'bounced' around by a turbulent atmosphere, the tip-tilt correction at least keeps the peak response of the light from smearing across less pixels of the imaging detector. This leads to an increase in signal that brightens a targets signal through stabilization before it reaches the deformable mirror.

Observatories that do not have any advanced AO systems generally still have the ability to maintain sub-arcsecond pointing with alt-az or equatorial mount tracking alone. These observatories typically also have an additional guidestar tracking ability which is usually a camera that is fed with light from the focal point via a pickoff mirror. If a bright star is in the FOV of the guidestar tracking camera, then the telescope can hone in its tracking during long exposures to reduce pointing error even further. This chapter will explore the modification of the HERESY instrument from a balloon payload to a system that can be plugged into the focal point of nearly any observatory and accomplish the same corrective image stabilization as a tip-tilt system.

4.2 Science Objectives

For every professional observatory that has advanced AO, there are several that do not. Therefore, the ability for HERESY to be seamlessly interchanged between a variety of ground-based telescopes and provide instant tip-tilt ability make it a versatile instrument to be used for any number of imaging campaigns. Observatories that employ tip-tilt optics for low-order image stabilization also require an extra reflection in the beam path, lowering throughput. There are also numerous smaller class observatories that do not have *any* adaptive optics or image stabilization systems.

The idea that adaptive element, in this case the hexapod, is entrenched in the instrument itself means that it can be attached to nearly any telescope focal plane and instantly improve imaging efficiency. The imaging of hard-to-resolve astronomical structures seen in nebulae, protostellar systems, and in our own solar system becomes finer and brighter as atmospherically scattered photons are ‘caught’ by the actively tracking hexapod focal plane to minimize light being smeared across pixels and strengthening signal. The active correction improves not only the data quality, but the signal-to-noise boost also increases the efficiency of the overall observing campaign by lowering required exposure times.

4.3 Engineering Drivers

Over the past decade there has been a sharp rise in the use of hexapods for nanometer-level positioning solutions. This has ranged from precision hexapods utilized in the robotics community, the medical community (robo-surgical applications), and in astrophysics – most notably on the ground-based Atacama Large Millimeter Array (ALMA) and on the James Webb Space Telescope’s (JWST) primary mirrors. However, no one has yet corrected positioning errors by mounting a cryogenic observatory focal plane directly to a hexapod.

In HERESY’s balloon configuration, the focal plane mounted on top of the hexapod included a copper cold structure that rigidly clamps the science detector in place while cooling it. In its observatory configuration, the focal plane was modified to have an OTS fast-read CMOS detector co-mounted with the science detector. The concept is that the CMOS and CCD are pointed at the approximate same swath of sky where the CCD is centered on the imaging target and the CMOS has a bright object in its FOV. While the CCD takes a long exposure of its target, the CMOS fast samples a bright star (100-300Hz) to determine pointing error. This pointing error is then transmitted to the hexapod for correction. In the balloon implementation of HERESY, all atmospheric turbulence is removed by being above >99% of the atmosphere itself, however from ground-based observatories there is still refractive turbulence resulting in uneven wavefronts.

As previously mentioned, HERESY cannot account for wavefront correction like a deformable mirror but rather tracks the linear displacement of the peak of the guidestar's PSF across the sky. This accomplishes image correction much like a tip-tilt system, where the bulk of incoming photons are now prevented from smearing across multiple pixels, leading to shorter exposure times and enhanced resolution.

4.4 Instrumentation

For its observatory implementation, the setup of the HERESY instrument remained similar as its balloon camera implementation except for a few additions. The cryostat form factor remained unchanged, the science CCD remained on the central face of the hexapod focal plane, the thermal cold plate with copper cold straps remained in use, etc. The validation and verification equipment (XY stages, vibration isolation optics bench, laser/retroreflector/PSM, etc.) also were all reused.

The major modification for the observatory implementation was the selection of a fast-read CMOS and slight re-designs to accommodate it being co-mounted as close as possible to the science CCD. The addition of the CMOS introduced new thermal challenges as the CMOS and readout electronics needed to be isolated from the CCD cold structure as its specifications called for operation no lower than 0 ^{o}C. A vacuum USB feedthrough was also added to the cryostat for the power and readout of the CMOS.

4.4.1 XIMEA CMOS

The CMOS selected for HERESY's ground-based implementation was required to be OTS, affordable, compact, and have the capability of at least 300fps imaging. The best fit that came out of a trade study was a CMOSIS CMV2000 board-mounted sensor with XIMEA's preprogrammed readout, image processing software, and C++ API (seen in Figure 54). As an added benefit, the CMOS also can window and only readout a specific pixel region which can grant readout rates as high as 800fps.

These capabilities were great for flexibility during laboratory testing and made it very easy to tell if an intended illumination source (star, light bulb, etc.) was in the frame of reference of the CMOS or not. To power and read out the CMOS, USB vacuum feedthrough was added to the cryostat to make it a truly plug-and-play interface.

4.4.2 Modification of Focal Plane

In order to produce a working prototype of HERESY in its observatory configuration, a low-cost quick-turnaround approach was employed. The first challenge was to co-mount the CMOS as close as possible to the science CCD on the hexapod. Ideally the two detectors would be buttable so that there would be as little of an imaging void between the two detectors. However, the e2v CCD already came in its own protective packaging that cannot not be removed or customized and is mounted on a custom interface PCB (which allows for power and clocks to travel to the CCD from the external Leach controller). The CMOS had its readout electronics attached to the back of the detector itself, which increased its footprint significantly. In addition to the footprints of both the CCD and CMOS packaging, the CCD is cooled while the CMOS readout/detector was not specified to operate below 0 °C, so the CCD and CMOS needed to be sufficiently thermally isolated from each other – both to keep the CCD from heating up and to keep the CMOS from freezing.

The CMOS detector almost certainly could have been cooled beyond its 0 ºC manufacturer specification, but there was concern that the readout electronics could be damaged, and since XIMEA would not give any numbers outside of their released consumer specs, the difficult thermal requirements were stuck to for ensuring the safety of the equipment. Therefore, with these limitations, the best that could be done was to mount the CCD and CMOS with an approximately ¾" gap from one edge of a detector to the edge of the other. To achieve the ¾" separation between detector edges, the CCD interface PCB was redesigned so that the CCD was as close to the PCB edge as possible, which required some tricky re-routing of signal traces in the PCB design and testing to confirm that traces were not too close to be capacitively coupled.

The CMOS and associated readout electronics were also mounted on G10 fiberglass to mitigate conductive heat flow into back into the CCD, and a copper strap from the back packaging of the CMOS readout electronics to the top of the hexapod to account for the lack of convective cooling in the cryostat. The mounting scheme can be seen in Figure 55 and Figure 56 and the change of layout to the CCD PCB interface board can be found in Figure 57.

4.4.3 Cryostat Thermal Performance with Addition of CMOS

The interior of the cryostat and hexapod focal plane is held under high vacuum and the cold plate is then cooled to liquid nitrogen's boiling point of -196 ºC. The CCD is then cooled via copper straps that are conductively linked to the cold plate. The addition of the CMOS added a major new heat source to the system. First, thermal shielding had to be removed to account for new USB cabling for the CMOS and then the CMOS and associated readout electronics were co-mounted next to the CCD on a G10 fiberglass interface. A copper strap heat sunk the CMOS electronics to the top of the hexapod to prevent overheating. Temperature sensors internal to the CMOS showed its temperature stabilize to ~+50 ºC during peak operation, which is the upper specified limit of the CMV2000 detector. While the CMOS mounting interface was as conductively insulative as possible, enough heat flow transferred to the CCD to cause it to operate approximately 25 degrees higher than it did without the CMOS at -45 °C, leading to an acceptable but not ideal increase in dark current.

Without the CMOS in place, the hexapod's top also got cold enough that it needed a supplemental heater to keep it within the manufacturer's temperature specification. However, since the CMOS was now heat sunk directly to the hexapod top and some radiation shielding was removed, the hexapod top never fell below +20 °C, removing the need for supplemental heat. As a result of the extra heat and reduction in radiation shielding, the cold tank hold time was reduced from ~13 hours to ~8 hours. A graph of the HERESY thermal performance with the CMOS and hexapod in operation can be seen in Figure 58. It is worth noting that the CCD temperature fluctuated +/- 2 °C based on heat production due to CMOS operation.

4.4.4 Telescope Mounting

HERESY's engineering checkouts were performed on Steward Observatory's 61" Kuiper telescope. Observers who use the Kuiper telescope typically use the resident cryogenically cooled camera system known as the Mont4k. However, for HERESY's testing, the Mont4k was removed from the telescope focal point and the HERESY cryostat was attached in its place. To ensure the flexible nature of the HERESY prototype, it was purposely designed with a lot of available space between the hexapod's mounting surface and the window of the cryostat. This allows a wide range of equipment to be mounted to the hexapod without the danger of interfering with the chamber's interior walls. However, it is worth noting that at the observatory where HERESY was tested, the focal point of the telescope's beam required the focal plane to be lifted approximately 6" higher toward the cryostat window. In future implementations, the extra space in the cryostat can be eliminated (handled instead by external spacers and baffling) and the focal plane can be brought much closer to the window. Figure 59 and Figure 60 show the CAD assembly of the custom telescope mount added to the top of the red cryostat.

Figure 61 shows the custom telescope adapter plate that rigidly mounted the HERESY cryostat at the Cassegrain focus on the back plane of the telescope. The cryostat to telescope mounting structure is more complex than it appears at first glance and is actually made up of three distinct components: 1) focal point spacer tube, 2) circular mounting interface, and 3) electrical insulator. While the focus of the Kuiper telescope can be adjusted, the intent was to make sure the hexapod focal plane matched the focal point of the Mont4k detector as closely as possible. Therefore, the required vertical displacement of the cryostat to telescope mount was carefully machined to place the hexapod focal plane at the same Mont4k focus. The focal point spacer tube, which is the same radius as the cryostat, mounted to the cryostat top face via already existing ¼-20 thru-holes. This included an s-slot (to prevent light leak) that allowed the shutter power cable to snake out from the interior window to the exterior. Above the focal point spacer was then a ¼" thick circular mounting interface with a much larger radius than the cryostat that had thru-holes which matched the Kuiper back plane mounting pattern.

To keep this interface flush with the telescope back plane, the through holes to attach the focal point spacer tube to the circular mounting interface were counterbored. Finally, since the entire Kuiper telescope was decoupled from the observatory structure (which is common to prevent observatory structure vibrations from propagating to the telescope), the Steward observatory team advised that the cryostat shell be electrically isolated from the telescope to prevent unwanted static discharge that could damage sensitive electronics. To accomplish this, a layer of 1/8" black rubber (with holes for screws to pass through) along with nylon screw pass throughs were used to completely insulate the cryostat from the telescope.

After the cryostat was successfully mounted to the back plane of the telescope with a shutter in front of the viewing window, the rest of the HERESY control equipment needed to be mounted. Since the Kuiper telescope slews across the sky on an equatorial mount, the cryostat often is over 10 feet above the observatory floor. Therefore, any equipment with cables attaching to the cryostat from the ground floor must be 20+ ft (see Figure 62).

Since this exceeded many of the instrumentation cable length requirements and since a series of long cables dangling around the observatory can easily lead to both tripping and tangling hazards, an OTS steel box was employed (traditionally used to mount servers) and modified to interface with the filter box structure on the back of the Kuiper telescope. Custom shelves were machined to accommodate instrumentation and welded slotted steel mounting bars were used to rigidly fix the box to the telescope to ensure minimal flexure even if the telescope was commanded to an extreme angle. Mounted in the box was a Trip-Lite conditioned power supply (to protect HERESY instrumentation from surges from the unreliable mountain power), the shutter control box and its power supply, the Leach controller for CCD readout and the controller power supply, a Lakeshore temperature controller (for temperature sensor readings and heater control), and the hexapod controller. Inside of the box, the control instrumentation was locked into place via custom cut ratchet straps which wrapped around slots in the shelving. The interior and exterior mounting interfaces of the steel box were also lined in black 1/8" rubber for insulation from the telescope, and the mounting screws in direct contact with the telescope were also fit through nylon sleeves for electrical isolation. After all of the mechanical interfaces were complete, a multimeter was then used to check that there was no continuity between any part of the HERESY cryostat or instrumentation to the telescope structure.

On the observatory floor, a long USB cable from a control computer hooked up to the cryostat USB feedthrough to control the CMOS. The CCD readout and clocking by the Leach controller was linked via an existing fiber optics connection (same one the Mont4k uses) that leads down to a control room below the telescope. The CMOS control computer was then remoted into via TeamViewer freeware for CMOS control from the control room. The rest of the necessary connections were linked to the cryostat from the steel box by being fed out of cut-out ports in the rear of the box, which enabled the use of short cabling (2 ft or less).

4.5 Guidestar Tracking

The purpose of the tracking code is to fast-sample a guidestar (100-200Hz), determine the peak of the star PSF, and then track the center point peak between successive frames. The software was written in C++ with a focus on maximum computing speed. A conceptual version of the code can be seen in Figure 63, and the pseudo-code is as follows:

1. Hold shutter open
2. Bright guidestar 'windowed' by CMOS and sampled at 200fps
3. The guidestar centroid in each successive frame is compared to the centroid in the previous frame to determine X-Y displacement in units of millimeters across the plate scale of the CMOS
4. Each X-Y displacement (micron-level) is then recorded as an error signal and sent to the hexapod
5. The hexapod performs an absolute move from its calibrated zero position to correct the error signal
6. Loop steps 2-5 until program is exited
7. Science CCD takes long exposure while hexapod is performing corrective motion
8. Close shutter at completion of exposure and exit code.

4.5.1 Tracking Code

The tracking code handles the setup and operation of both the Ximea CMOS (guidestar tracking) and the hexapod. During the initialization phase both the CMOS and hexapod connections are established. The CMOS reads out its temperature to confirm it is within its operating range and then turns off several LEDs attached to its readout circuitry. When the Ximea camera was delivered the CMOS and readout electronics were packaged in a protective housing, and LEDs from the CMOS electronics could be seen exterior to the camera housing to indicate power on and nominal operation. Since the CMOS and electronics were removed from their original housing to be mounted onto the hexapod, the LEDs shone into the cryostat interior and threatened to saturate science CCD images – thereby requiring they be turned off in code. If required, the hexapod also performs a reference of its six axes to establish its positional origin. The hexapod velocity was also manually set to its max of 10 mm/s since its default velocity at boot up is 5 mm/s.

With the correct on-sky telescope alignment, a bright natural guidestar is placed in the FOV of the CMOS. Before any tracking can be started, this guidestar needs to be 'windowed' by establishing a region of interest (ROI) around the star PSF. Once this ROI is established, the rest of the CMOS pixels are programmed to be deactivated so that only ROI pixels are read out. Lab measurements showed that a 200 × 200 pixel ROI allowed for successive images to be read out at ~800 fps. For the purposes of the tracking code, the exposure and readout time of the CMOS is configured to ~0.01 ms (100 Hz) otherwise the exposure frequency is too quick for the both the rest of the tracking code and the hexapod to catch up to.

After the guidestar is windowed in an ROI, a snapshot image is taken of the star PSF. For speed, the code collapses the two-dimensional image array into two 1D arrays. This initial image is used to establish a reject criterion before running the tracking algorithm. The mean and standard deviation are calculated for the pixel values and then the pixels are scanned through to eliminate any data that is more than 10 standard deviations from the mean.

After the reject criterion is in place, images are then continually collected at 200 Hz. To locate the PSF centroid from image to image, a nonlinear least squares fit approach is used. Nonlinear least square methods find the minimum or maximum of a gradient by decreasing the sum of the squares of the errors between a fit function and actual data points. This is done via a successive update of fit function values until the fit is near perfect. Two common fit methods are the Gauss-Newton and gradient descent methods. The Gauss-Newton involves reducing the sum of the squared errors by treating the local data as quadratic and then finding the minimum of that quadratic. The gradient descent method reduces the sum of errors by updating the fit function values in the direction of the gradient's steepest descent. However, in the case of locating a star's centroid it should be noted that the gradient terminology is flipped and the gradient's steepest *ascent* is actually being found.

To maximize accuracy and computing speed, a method known as the Levenberg-Marquardt algorithm is used. The Levenberg-Marquardt algorithm is a well-known approach that is a combination of the aforementioned Gauss-Newton and gradient ascent methods. To maximize efficiency and accuracy, Levenberg-Marquardt acts as a combination of the Gauss-Newton and gradient ascent methods where a 'damping parameter' is introduced. This damping parameter is initialized as a low value which in turn causes the first steps of the algorithm to move toward the direction of steepest ascent. If any step results in a worse estimate of a good fit, then the damping parameter decreases further and the algorithm keeps incrementally searching, but as the iterations move in the correct direction, the damping factor begins to rapidly increase. The increase in damping factor causes the algorithm to then behave as a Gauss-Newton and accelerates it toward the local maximum – the centroid of the PSF. The fundamental Gauss-Newton and Levenberg-Marquardt formulas where the purpose of each iteration is to produce a perturbation 'h' to the parameters 'p' are as follows:

$$\{Gauss-Newton\}: [\boldsymbol{J^T W J}]\boldsymbol{h_{gauss-newton}} = [\boldsymbol{J^T W}](\boldsymbol{y}-\boldsymbol{\hat{y}})$$

$$\{\text{Levenberg-Marquardt}\}: [\boldsymbol{J^T W J}+\boldsymbol{\lambda I}]\boldsymbol{h_{levenberg-marquardt}} = [\boldsymbol{J^T W}](\boldsymbol{y}-\boldsymbol{\hat{y}})$$

where, for simplicity, $\boldsymbol{J}$ is a Jacobian $[\frac{\partial \hat{y}}{\partial p}]$ (representing sensitivity of function 'y' to varying parameters 'p') W is a weighing matrix, h is the parameter update between iterations that moves the fit in the 'steepest' direction toward the star centroid, I is an identity matrix, and λ is the 'damping parameter.' If lambda is near zero it can be cancelled out and one can quickly see that the Levenberg-Marquardt equation essentially *is* the Gauss-Newton method. Therefore, when initialized with a large lambda value, this implementation is designed to for the fit model to take small steps toward the steepest descent on a plane, and as lambda becomes insignificant, turn into the Newton-Gauss method and rapidly converge on a fit (Gavin, 2013).

Regarding computing speed, Figure 64 shows a plot from Chernov, 2008 in which various least squares fitting methods were used and their computing requirements measured. In the chart 'LAN' stands for Landau, 'SPA' for Späth, and 'LMC'/'LMA' stand for two slightly different types of the Levenberg-Marquardt method. In the chart, the Y-axis is in FLOPS (floating point operations per second), and the X-axis is in number of data points included in the simulation. It is clear to see that the Levenberg-Marquardt is a more computing efficient algorithm, particularly if there are fewer data points to work with when forming the fit.

It should also be noted that to initiate the Levenberg-Marquardt requires a ‘best guess’ for a starting position within the ROI before the algorithm can begin working its way across the plane toward the data’s maximum. This is accomplished by calculating a center-of-mass within the array given by this formula:

$$C_x = \frac{\sum C_{ix} A_i}{\sum A_i}, C_y = \frac{\sum C_{iy} A_i}{\sum A_i}$$

where C_x C_y are the x,y center-of-mass coordinates, C_i is the ith pixel value, and A_i is the area. While a starting point is required to begin the algorithm fitting iterations, it was found that the center of mass equation itself was typically able to ‘guess’ the centroid within a mere tens of pixels.

The Levenberg-Marquardt algorithm was adapted for C++ using guidance from *Numerical Recipes* (Press et al., 2007).

4.6 Observatory Testing

To test HERESY in the field two separate engineering runs on Steward Observatory’s 61” Kuiper telescope were granted. The effort from moving the cryostat and all associated hardware from the lab environment to the field should not be understated, and the first observing run was almost entirely dedicated to mounting and performing engineering checkouts while HERESY was interfaced at the focal point of the telescope. Several bulky pieces of hardware such as the Leach controller, hexapod controller, temperature controller, etc. must interface with the cryostat and have strict cable-length requirements. This is an obvious issue since the telescope moves across the hemisphere of the sky, sometimes placing the cryostat as far as 10-15 feet above the observatory dome floor. The range of motion of the telescope with HERESY fully integrated to the telescope can clearly be seen in Figure 62.

To solve this, a steel box was modified (originally designed for server stack mounting, so it had plenty of existing attach points for shelving and good ventilation) and mounted of the HERESY external hardware inside. To ensure no equipment shifted around due to telescope operations, ratchet straps were used. To account for cable lengths, the box was mounted on the side of the telescope near the cryostat to the same structure that holds the filter wheel assembly for the 61" scope. After mounting, the observatory staff then had to rebalance the telescope to accommodate new mass and CG-shift due to HERESY's attachment.

Another challenge we faced is that while the 61" Kuiper reflector is able to change its focus by moving its secondary mirror via motor, the observatory's associated guiding camera focus was fixed. Typically, an instrument called the Mont4k is attached to the back of the Kuiper telescope, and while HERESY's focal plane was attached very close to where the Mont4K's focal plane was positioned, the telescope still had to be slightly refocused. What this meant was that while the CCD and CMOS on the hexapod were brought into focus, the observatory guide camera was put out of focus and could not be corrected. Despite being out of focus, we were still able to track on 'fuzzy' guidestars, but this meant that the telescope could not be pointed as ideally as was hoped.

Once setup on the telescope was finished, a full engineering checkout of HERESY was performed. Unfortunately, during this checkout it was discovered that half of the CCD, which is a two-channel readout, was lost. The root cause of the anomaly could not be determined, but it may have been due to electro-static discharge while setting up HERESY on the low-humidity observatory floor. Ideally, the pixel clocking could have been modified to be serially shifted to the one remaining healthy readout amplifier, but the PCB wiring scheme prevented such an on-the-fly modification. Regardless, the observing run continued through this issue and a series of calibrations were taken.

HERESY was cooled and then bias and flat fields were taken, but before the instrument was tested on targets, we wanted to do an on-sky verification of the geometry of our imagers. As a ‘first-light’ test an image of Saturn was taken in multiple bands which was later converted into an RGB image seen in Figure 65. For detector geometry a creative solution was to point the telescope at the lunar surface and then match our imager frames to the Lunar Reconnaissance Orbiter Camera (LROC) survey map. Figure 66 shows the results of this geometry exercise and we confirmed that the center of the working half of the CCD was 3.85 arcminutes from the center of the CMOS. Using this positional truth, imaging targets were chosen that had a bright star centered in the CMOS and a target of interest in the FOV of the CCD.

4.6.1 Data Collection Setup

In the observatory command room, the telescope had its own target catalog and pointing infrastructure which resided on a standalone computer. This software was also used to select filters by driving filter wheel motors and selecting guidestar tracker settings for improved telescope pointing.

The main HERESY control computer was on the observatory floor and was controlled remotely via TeamViewer from the command center. This computer was essential as it commanded the CMOS exposures, ran the centroid tracking algorithm, and commanded the hexapods corrective movements. The user interface can be seen in Figure 67. Finally, an additional computer was setup in the command center that leveraged an existing fiber optic cable setup for commanding a Leach controller. This computer was used to configure the Leach controller, start CCD exposures, and save CCD video data to file in FITS format.

4.6.2 Data Collection Methods

Typically, the science detector is coupled to the center of the target FOV of the telescope. For example, if the Andromeda Galaxy (M31) was selected as the target programmed for the telescope to point to then one would expect that a corresponding exposure with the science detector would be centered on Andromeda's galactic nucleus. Any guidestars would then be located on the periphery of the central FOV of the telescope.

However, in HERESY's prototype design, only one CMOS is co-mounted with the science detector and only provides a limited FOV. Due to this limitation, no matter what target was navigated to in the FOV of the CCD, it was extremely challenging to also fortuitously line up a bright star in the FOV of the CMOS. Therefore, the telescope was re-programed to have telescope targets centered in the FOV of the CMOS and guarantee access to a bright star for tracking (minimum magnitude ~3 was required for 200fps imaging before the PSF became too hard to track – see Figure 68).

After a bright star was successfully windowed in the field of view of the CMOS, a long exposure (up to 600 seconds) was taken with the CCD to determine if any stars would appear in the image. In a maximum of 600 seconds exposure time, if stars appeared in the CCD image and were at least ~2 times higher intensity (ADU) than the sky background signal, then an image stabilization/data collection could be attempted.

During a system test, first the guidestar was windowed in the CMOS FOV in software. It was then confirmed that the star was bright enough for the CMOS to accurately report fluctuations in the X-Y position of the star's centroid. This was done by running a custom script that printed current X-Y positions of the star's centroid from an initial starting point. If the star was too dim, the centroid was either impossible to track or could only be intermittently tracked, which would show up as large X-Y position outliers in the print statements.

After a CMOS guidestar was successfully established, an exposure was taken by the CCD with the hexapod stationary to establish a baseline. This baseline image was used to provide a metric for the atmospheric seeing at the time before any image stabilization attempt. Finally, an additional CCD exposure was taken, but this time with the CMOS tracking and hexapod corrective movements taking place. The baseline images and corresponding corrective images were then used to judge the performance of the system.

4.6.3 Strehl Ratio Calculation

The Strehl ratio is the usual metric for characterizing astronomical imaging quality. The equation for the Strehl ratio is simply:

$$S = \frac{I_{target\ PSF}}{I_{diff-limited\ PSF}}$$

Where $I_{target\ PSF}$ is the peak intensity of a target star's PSF and $I_{diff\text{-}limited\ PSF}$ is the peak intensity of a 'perfect' diffraction-limited point-source produced by a Fourier transform of the shape of the telescope optical path (Lewis, 2004 and Roberts, 2002).

First, the on-sky science images are bias, flat-field, and sky background corrected, to make sure that detector calibration does not skew the Strehl ratio. Then the flux of the target PSF intensity is calculated by placing an aperture around the PSF with a 2" radius (~15 pixels). After this is obtained a theoretical diffraction pattern for a Cassegrain reflector is calculated. Care is taken to carefully match the detector plate scale of the original science target PSF and the theoretical PSF for consistency. To account for the fact that the science target images were taken of stars of varying magnitudes and at different exposure times, the diffraction-limited PSF flux (also a 2" radius aperture) was normalized to equal the flux of the science target PSF.

To accomplish these calculations, the DAOPHOT astronomy library in IDL (Landsman, 1993) was used to measure the target PSF against the theoretical diffraction-limited PSF to find the Strehl ratio. The purpose was to establish a metric to measure if the tracking code and resultant hexapod stabilization improved the quality of the image.

The series of dome flats (for observatory flats a screen on the interior of the dome was used and can be seen in Figure 69) and bias frames taken for calibration were used to produce a super bias frame (median combine of ten biases) and a super flat for each filter wheel filter (super bias subtracted from each frame, ten flats per filter median combined, and then all the pixels divided by the average of a 100 × 100 square of pixels to normalize the values). Each science CCD image was then bias subtracted and flat normalized based on the telescope filter selected. Dark current was negligible for the length of the exposures and temperature of the CCD, so it was ignored. For each HERESY test run, an image was taken with the hexapod stationary and then with the hexapod actively correcting with the tracking code.

In science images, DAOPHOT CNTRD function was used to locate the centroid of the target star PSF. This X-Y pixel coordinate was then fed into the APER function which takes a centroid, creates an aperture around it (in this case radius of 2”), and then returns the magnitude of the star. MAG2FLUX was then used to convert this value into a flux.

The theoretical diffraction-limited PSF for the Kuiper 61” telescope was also modeled. This was done by projecting the telescope pupil into an image, in this case a circular aperture with a circular obscuration seen in Figure 70. Using an FFT, this was transformed into an ideal point source PSF (also seen in Figure 70). From the flux found in the star from the science image, the ideal PSF was then multiplied by a constant to match its flux to the science image. With both the science image and the theoretical image normalized to the same flux, the max intensity was then found for each image. These two max intensities then formed the numerator and denominator in the division that forms the Strehl ratio (side-by-side PSFs ideal and target are seen in Figure 71).

4.6.4 Results

Since this engineering test required pointing the telescope to make sure a bright star was in the FOV of the CMOS, the stars that were used in the science CCD images are unknown since all that was needed was to characterize the before and after Strehl ratios of their PSFs. Figure 72 displays the data collection runs and the associated target star Strehl ratios before and after HERESY corrective movements. Error bars for each measurement were calculated from uncertainties introduced during image processing (bias subtraction and flat-fielding) and from the aperture photometry steps performed in IDL that were described in the preceding section.

4.6.5 Discussion

The data in Figure 72 for the five data runs does not display a significant improvement in image quality (increase in Strehl ratio). However, while the error bars admittedly overlap for each set of measurements, there appears to be a positive trend of increased image quality (higher Strehl ratio) for three of the five runs. Runs three and five clearly show little to no change between a seeing limited exposure and when HERESY was actively correcting. This lack of change may have been due to local atmospheric seeing degrading when HERESY was exercised after taking the initial 'control' image. Conversely, it could be claimed that local seeing might have improved between taking the control and corrective image to give a 'false positive' of HERESY improving the Strehl ratio. This seems an unlikely coincidence to occur on three separate runs, especially since the ‘active correction’ image was taken immediately after the ‘seeing limited’ image, meaning that in a period of <5 minutes, the turbulence qualities of the airmass being observed through would have improved each time.

4.6.6 Conclusion

This project demonstrated the versatility of HERESY in that different focal planes can be swapped onto the hexapod’s face to change the purpose of the instrument. In this configuration, HERESY was also proven to be able to interface and take on-sky images at a meter-class observatory.

The limitations of HERESY in its ground-based configuration were clear in that it is extremely challenging to simultaneously align a science target in the CCD FOV and a natural guidestar (mag 3 or greater) in the CMOS FOV. To solve this, future iterations should include three additional CMOS trackers positioned orthogonally around the CCD on the hexapod focal plane to increase the odds of locating a guidestar. Then, before an imaging run is initiated, only one of the CMOS would be selected, which had the best guidestar for tracking available. While the Ximea CMOS was sufficient for engineering tests, future iterations might select a far more sensitive, higher-grade detector so that guidestars dimmer than magnitude 3 could be selected for tracking, thereby increasing the catalog of available guidestars across the sky.

Another idea is to remove the need for natural guidestars altogether by bringing a laser along with HERESY to mount to the telescope and produce an artificial guidestar in the upper atmosphere. However, this would likely add complexity since high altitude lasers are high powered and require permitting for use.

Also, each observatory structure is different, therefore a different laser mounting scheme would have to be determined each time.

The equipment required to operate HERESY on the back of the telescope is very bulky in its prototype form. The cryostat requires an entire steel box of instruments for operation that includes everything from CCD readout electronics, a temperature controller, a shutter controller, the hexapod controller, etc. There were far too many large and heavy HERESY support instruments that necessitated the need for the steel box, but a future iteration should decrease the electronics footprint into a single unit that can mount directly to the HERESY cryostat. This could be accomplished by working with vendors to de-integrate electronics from their COTS packaging to consolidate everything into a singular 'avionics box.' Therefore, the instrument would be compact enough to only have to bolt the cryostat structure itself to the back of the telescope for data collection.

Finally, Windows OS is a limitation on the computing speed for software that commands hexapod corrective movements and processes the CMOS star tracker algorithm. Using Linux and real-time software could greatly improve speed of the instrumentation and produce better corrective results than what were gathered in Figure 72.

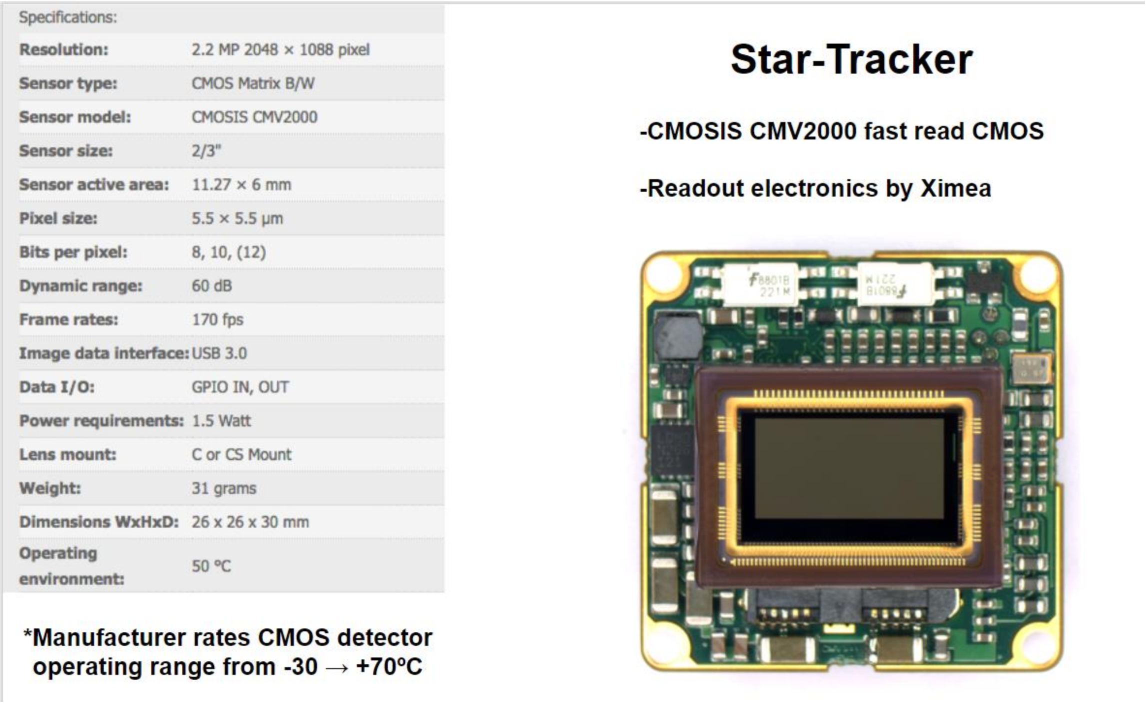

Specifications:	
Resolution:	2.2 MP 2048 × 1088 pixel
Sensor type:	CMOS Matrix B/W
Sensor model:	CMOSIS CMV2000
Sensor size:	2/3"
Sensor active area:	11.27 × 6 mm
Pixel size:	5.5 × 5.5 µm
Bits per pixel:	8, 10, (12)
Dynamic range:	60 dB
Frame rates:	170 fps
Image data interface:	USB 3.0
Data I/O:	GPIO IN, OUT
Power requirements:	1.5 Watt
Lens mount:	C or CS Mount
Weight:	31 grams
Dimensions WxHxD:	26 x 26 x 30 mm
Operating environment:	50 °C

***Manufacturer rates CMOS detector operating range from -30 → +70ºC**

Star-Tracker

-CMOSIS CMV2000 fast read CMOS

-Readout electronics by Ximea

Figure 54. Packaged CMOS from XIMEA (https://www.ximea.com/)

Specs of the CMOS chosen for star tracking on the modified HERESY focal plane. Full frame readout rate is 170 fps, but after windowing a target of interest, readout rates were tested up to 800 fps.

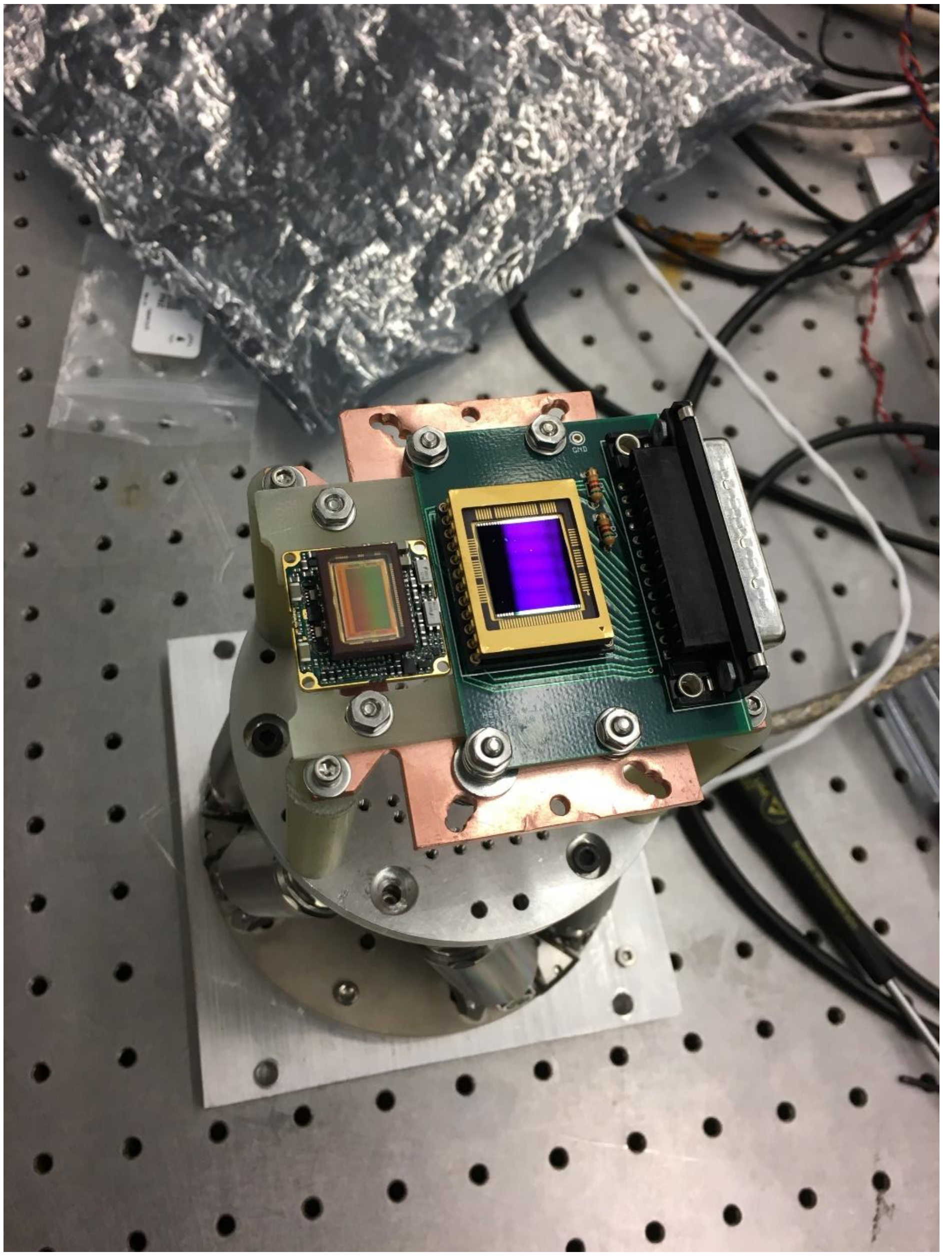

Figure 55. Focal Plane Mounting

Mounting of the CMOS as close to the CCD as possible. Due to packaging of detectors, they were not able to be co-mounted more than 0.75” from each other.

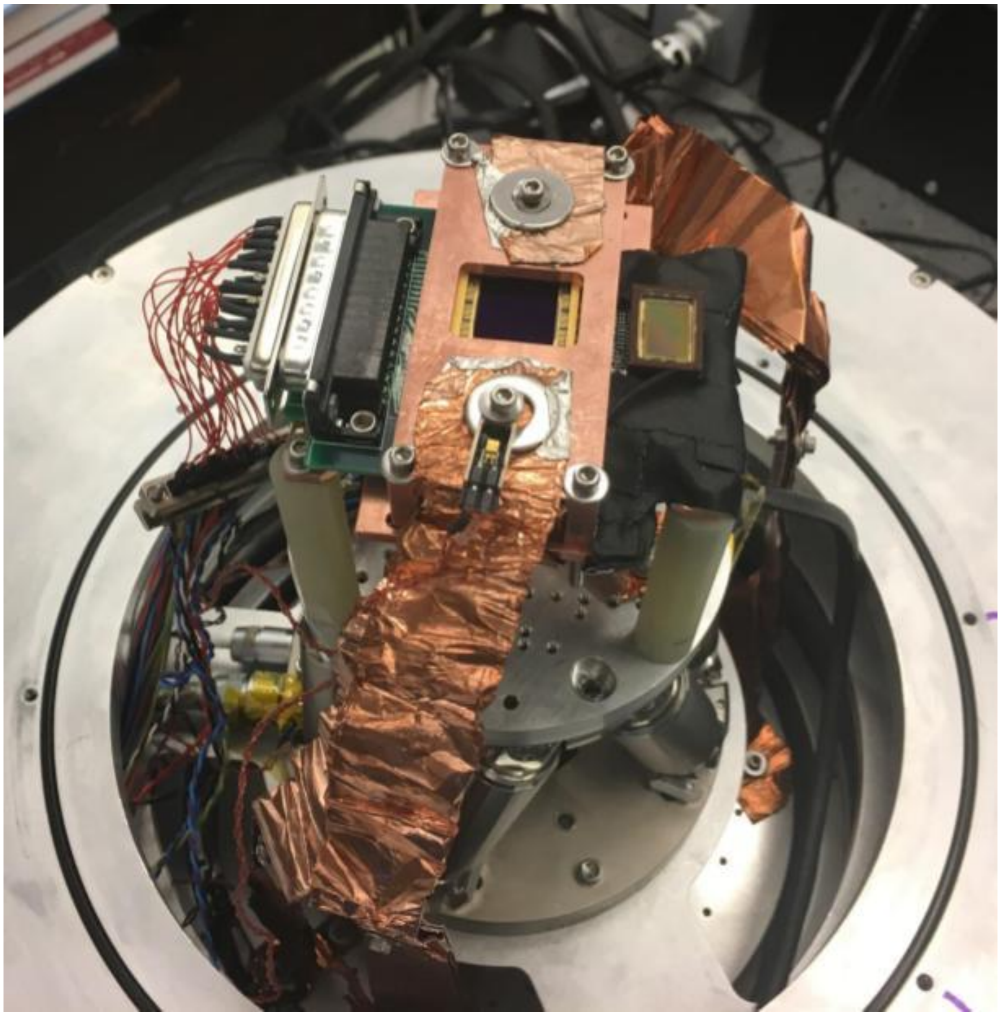

Figure 56. HERESY Focal Plane Fully Built Up with CMOS

The fully built up HERESY focal plane with CMOS installed, ready to be sealed and taken to the observatory. The CCD is cryogenically cooled, while the CMOS is thermally insulated to operate at ambient cryostat temperature. The CMOS detector was heat sunk to the top of the hexapod to prevent overheating.

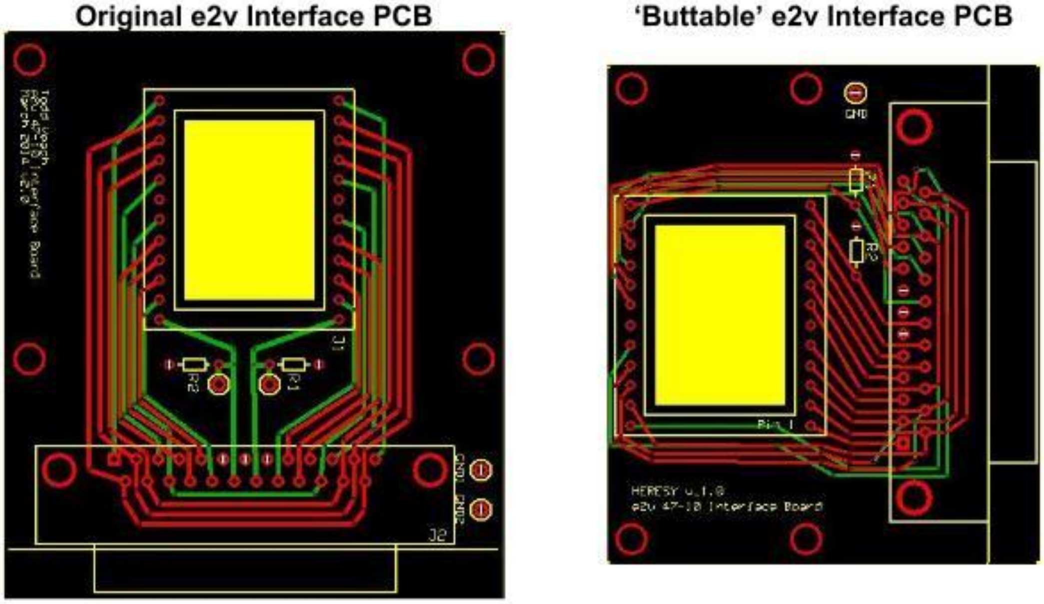

Original e2v Interface PCB

'Buttable' e2v Interface PCB

Figure 57. CCD Interface Board Modification

The CCD interface board, how the CCD receives power and clocking signals, was redesigned in an attempt to mount it as close as possible to the new CMOS detector as possible.

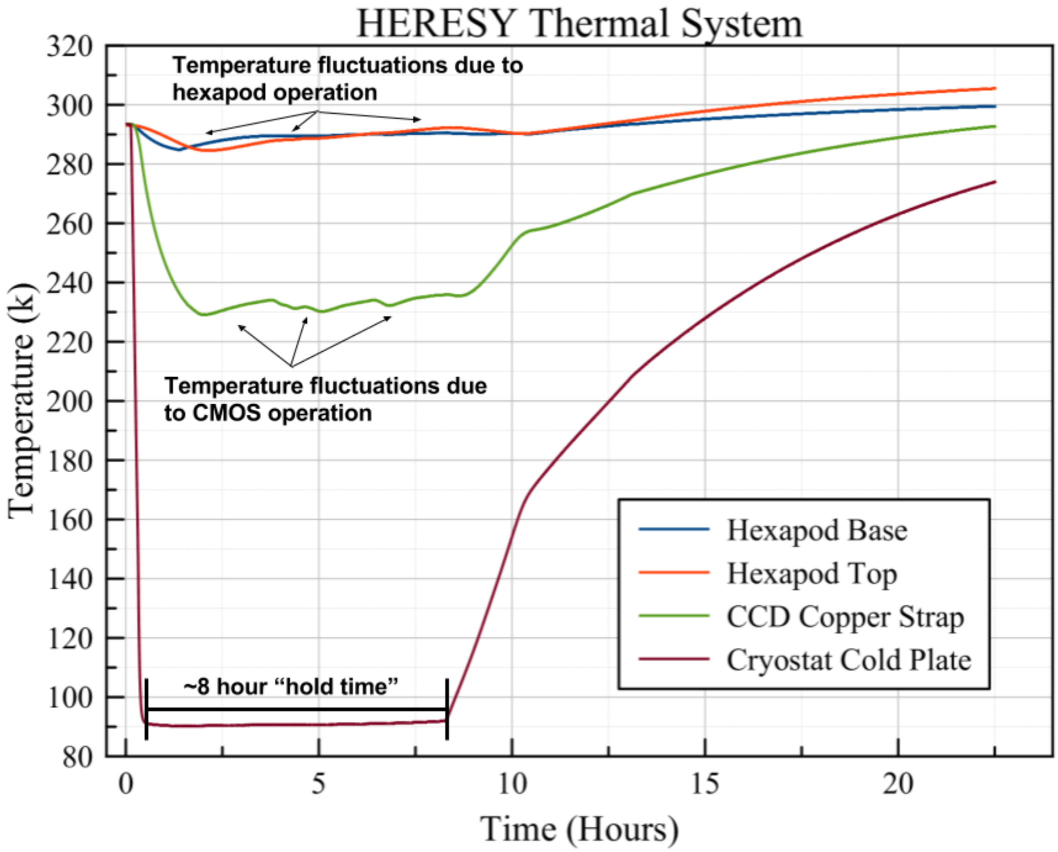

Figure 58. HERESY Modification Thermal Performance

Thermal performance of the instrumentation in the cryostat after the introduction of the CMOS and necessary reduction in radiation shielding to accommodate new equipment.

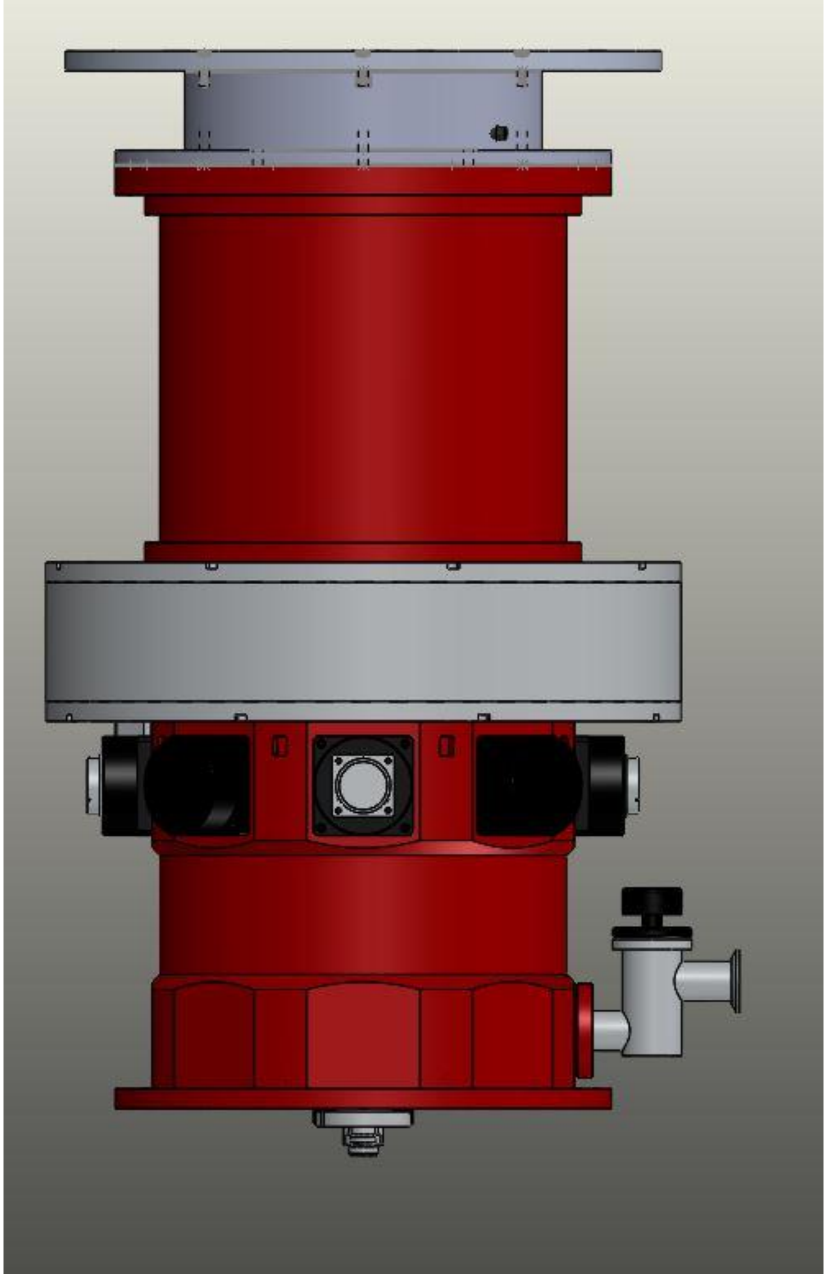

Figure 59. HERESY with Kuiper Telescope Mount (Side View)

This figure shows a side view of the mounting structure designed and fabricated to attach the HERESY instrument at the focal point of the Kuiper telescope. The shutter power connector can be seen emerging from the mounting cylinder in the model near the top of the assembly.

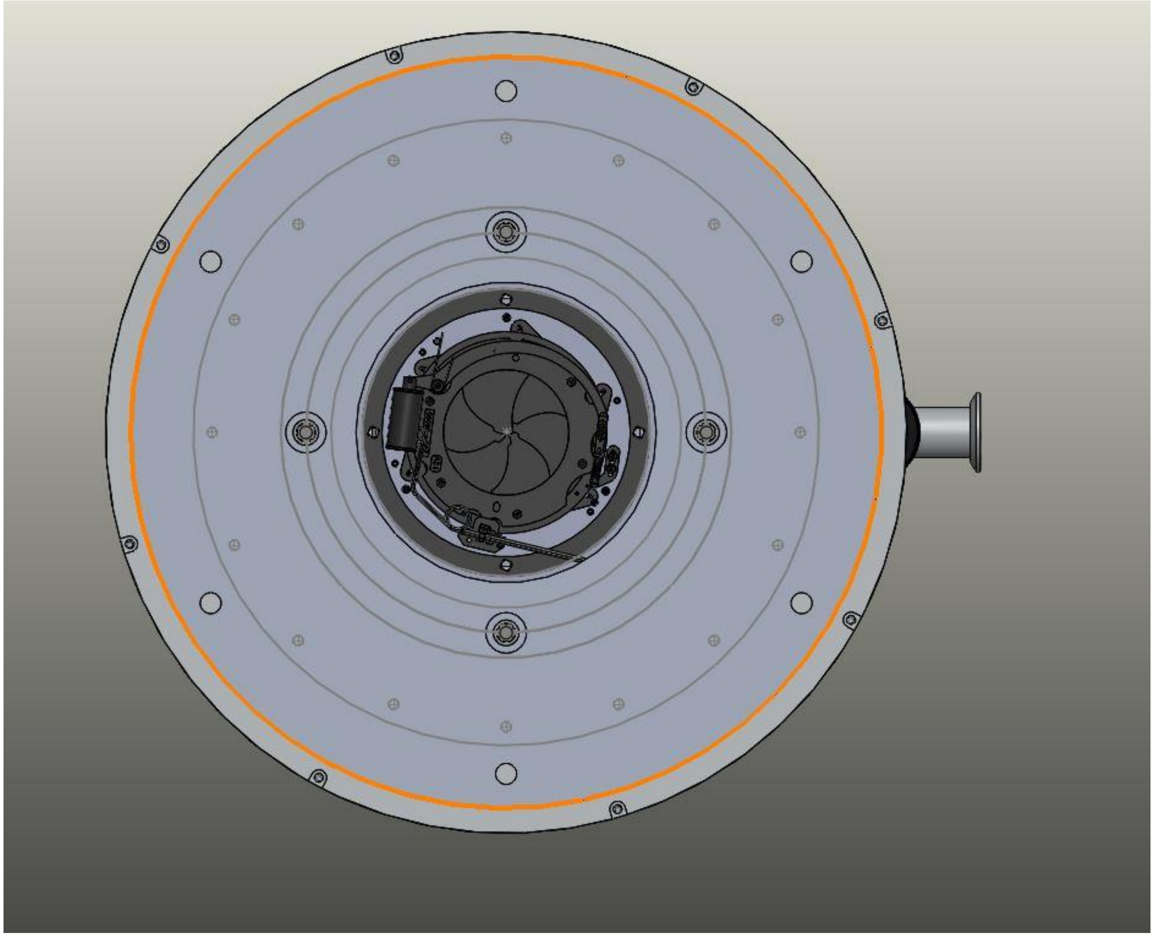

Figure 60. HERESY with Kuiper Telescope Mount (Top View)

The top view of the flange designed to mount to the circular hole pattern on the backplane of the Kuiper telescope. Not pictured in this model is the insulating rubber that electrically isolated the cryostat structure from the telescope.

Figure 61. HERESY and Steel Instrumentation Box Mounted on Kuiper Telescope

The HERESY instrumentation mounted onto the back plane of the Kuiper 61" telescope while in the 'stowed' position.

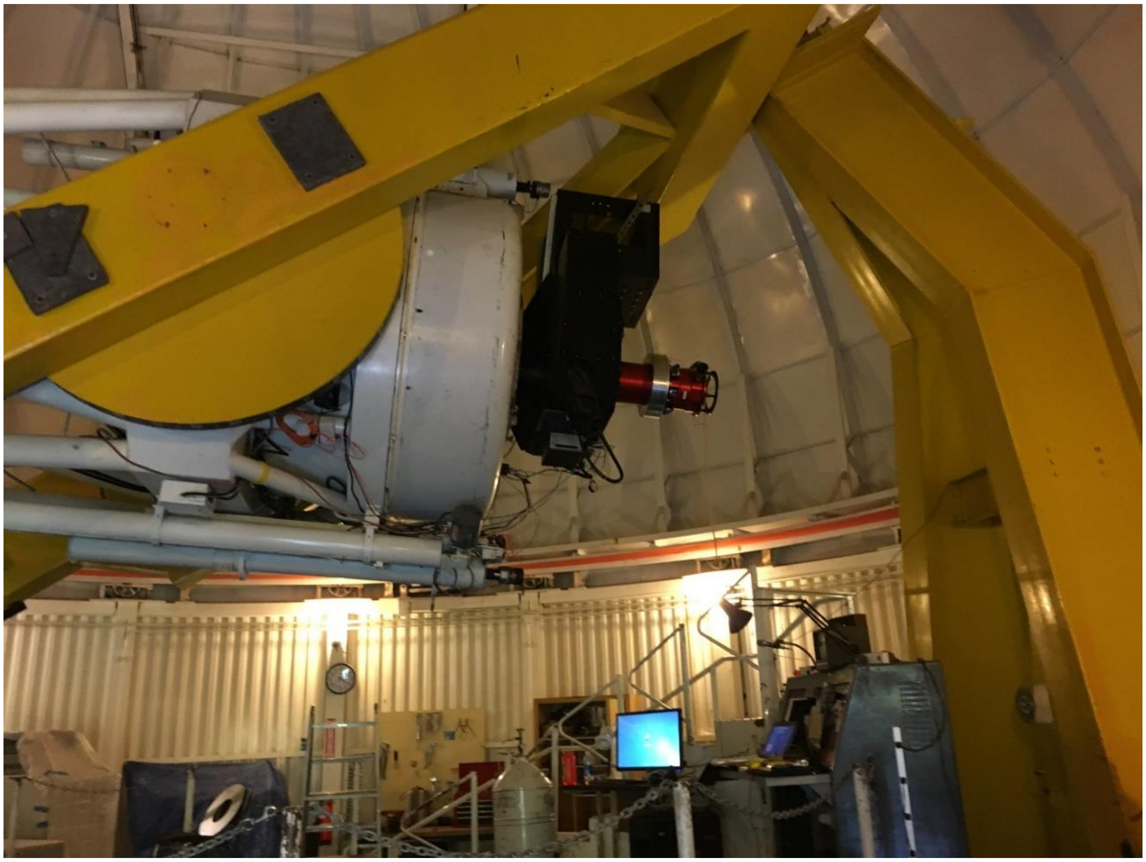

Figure 62. HERESY and Steel Box Being Lifted High Above Observatory Floor

A demonstration of the reason almost all of HERESY's external instruments and cabling had to be mounted in a steel box on the side of the telescope to 'ride-along' with the cryostat.

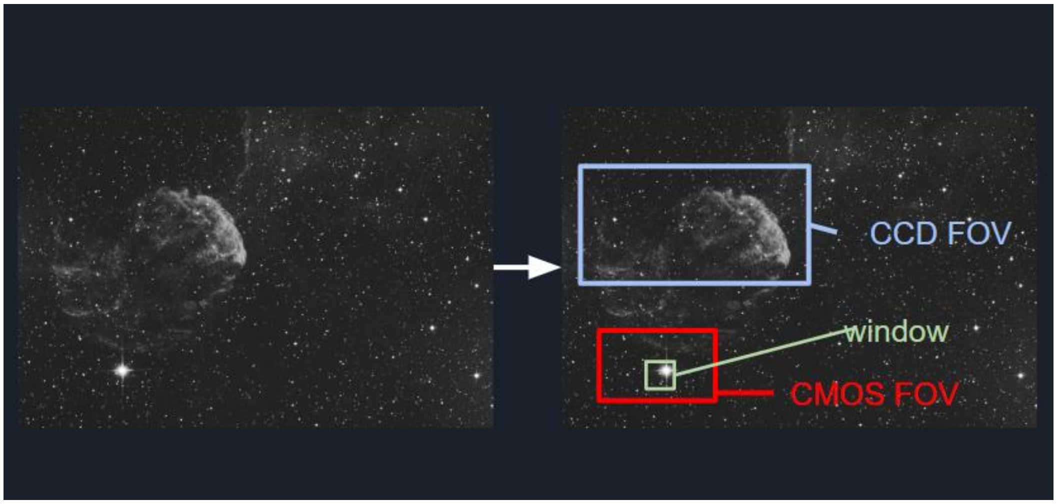

Figure 63. Visualization of simultaneous science imaging and natural guidestar tracking

Limitation of the design was that a bright guidestar needs to be in the CMOS FOV while the science target of interest is in the CCD FOV. Future work proposes mounting multiple CMOS trackers to the focal plane to increase the odds of a bright guidestar being available.

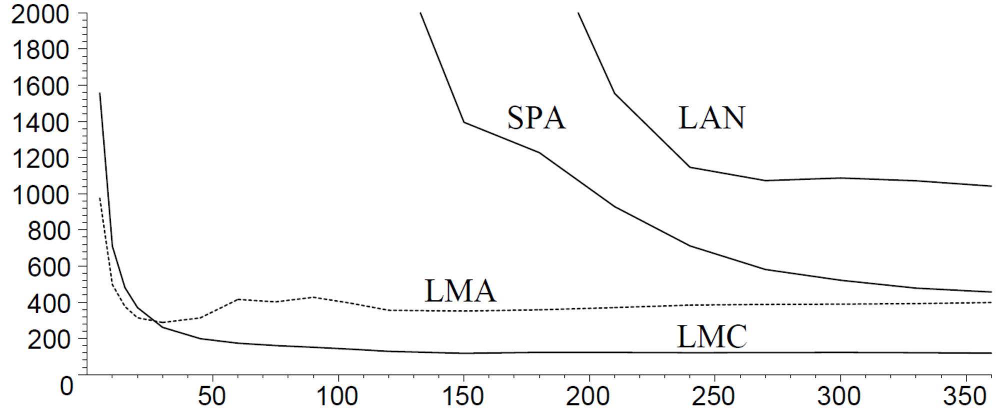

Figure 64. Computing cost in FLOPS vs. amount of data points in data set (Chernov, 2008)

The Levenberg-Marquardt (LMA and LMC) algorithms show excellent low computing cost stability with as few as only ten data points available for least squares fit computations.

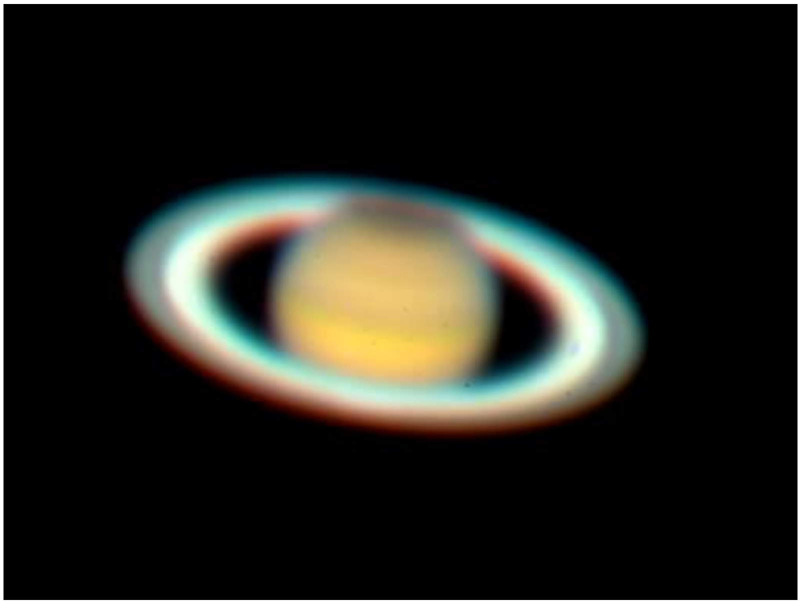

Figure 65. RGB image taken by HERESY w/ U, B, I filters

This image was ‘first light’ of the HERESY instrument after it was successfully mounted and calibrated on the Kuiper 61” telescope.

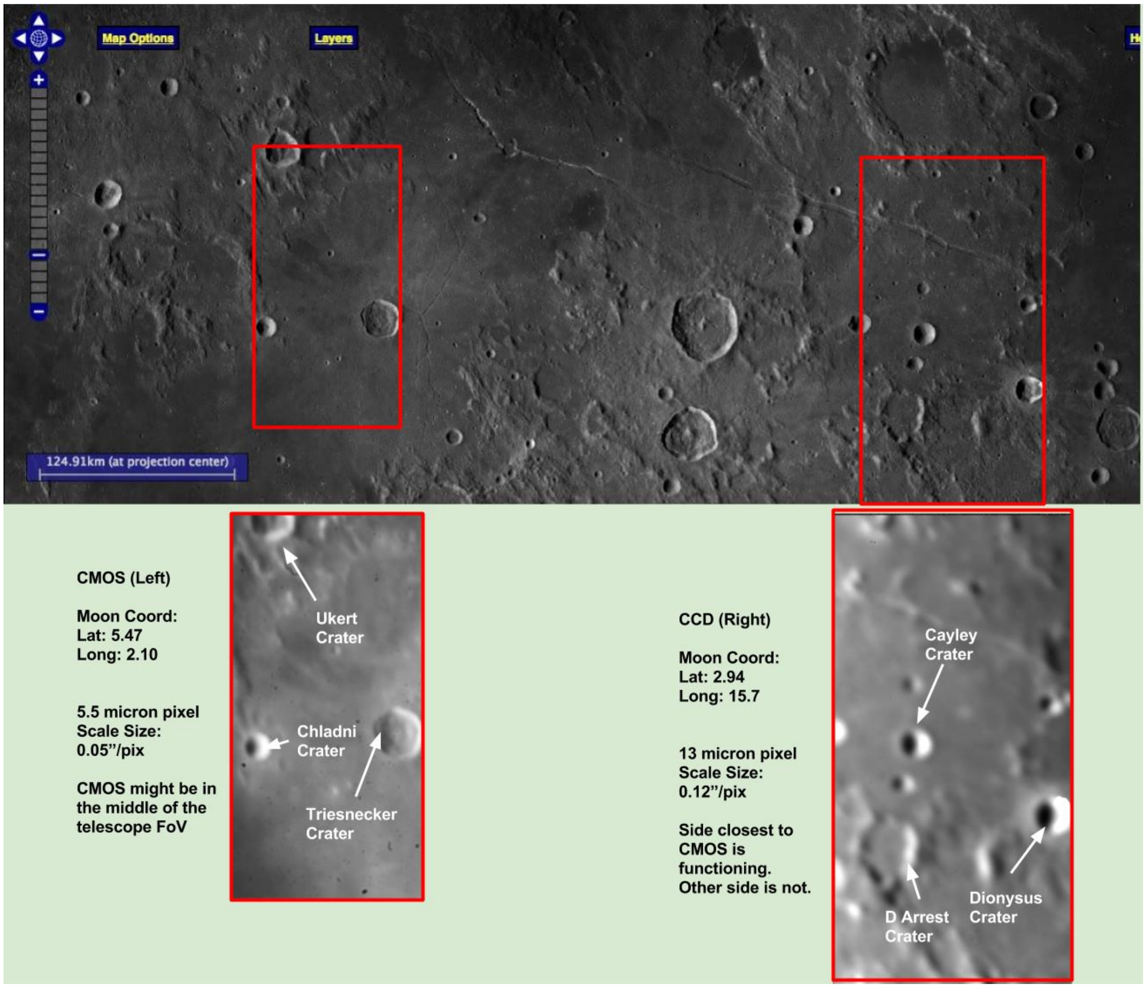

Figure 66. Lunar Surface -- Focal Plane Test and Angular Distance Measurements

As part of the on-sky engineering testing of HERESY, the Moon was imaged by the CCD and CMOS focal plan to get a better grasp on the detector geometry and to demonstrate the system was working at the focal point of the telescope.

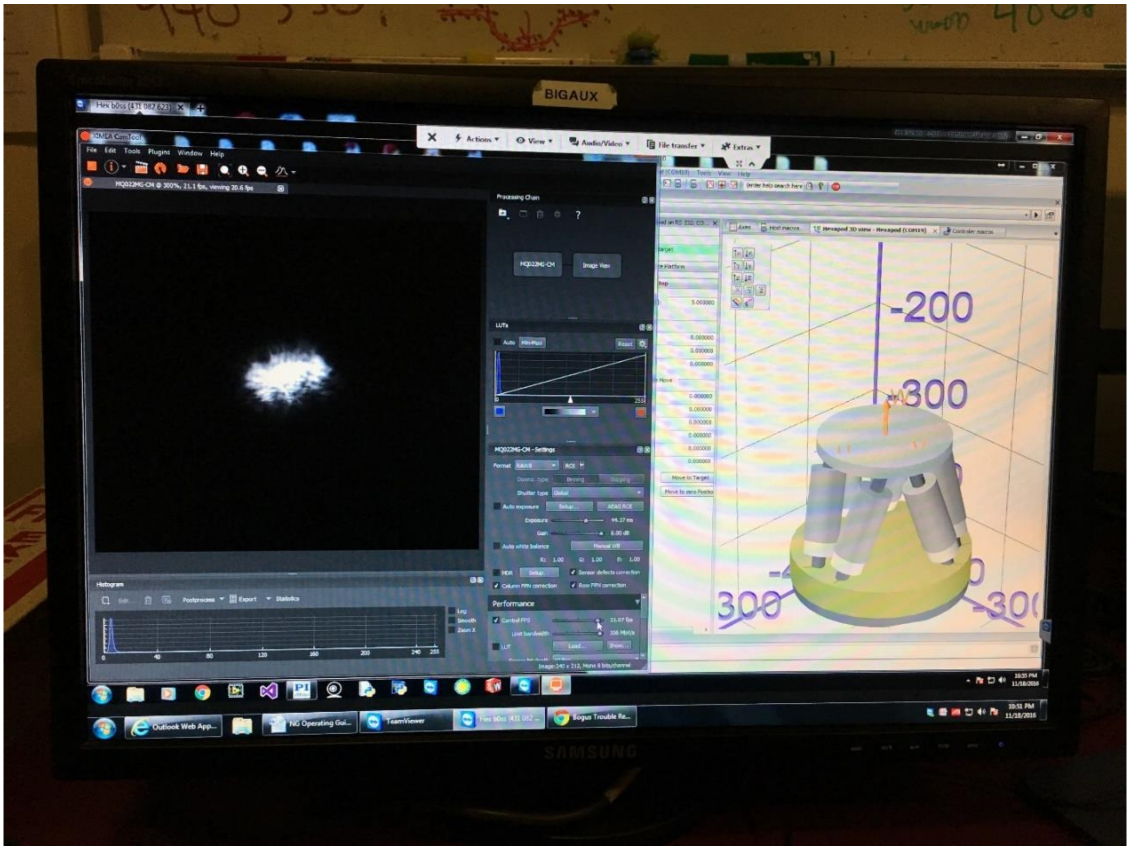

Figure 67. CMOS and Hexapod GUI Interface

A bright guidestar is shown as it is being sampled in the center of the CMOS FOV as the hexapod software visually displays current orientation of the hexapod.

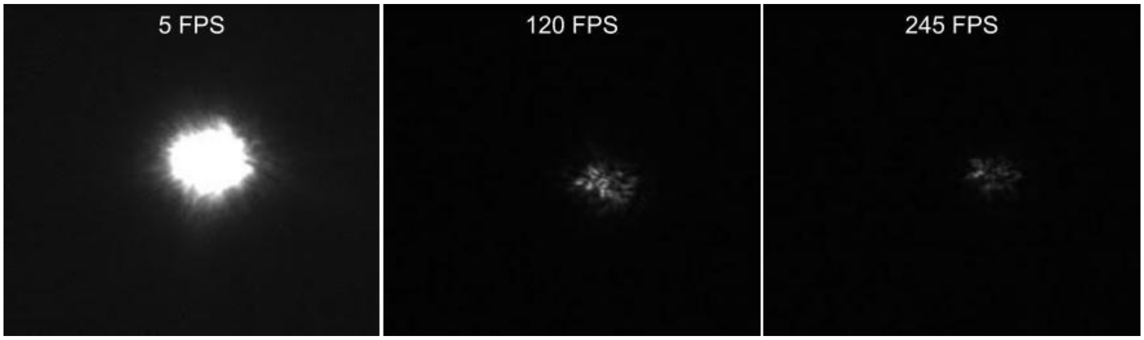

Figure 68. Natural Guidestars at Various CMOS Sampling Rates

A major challenge with the HERESY design and CMOS detector chosen for the observatory testing was that it was very difficult to line up a bright guidestar with any bright astronomical targets imaged. In addition, when a guidestar was located, the detector was often not sensitive enough to effectively track the star centerpoint (minimum magnitude for tracking was ~magnitude 3).

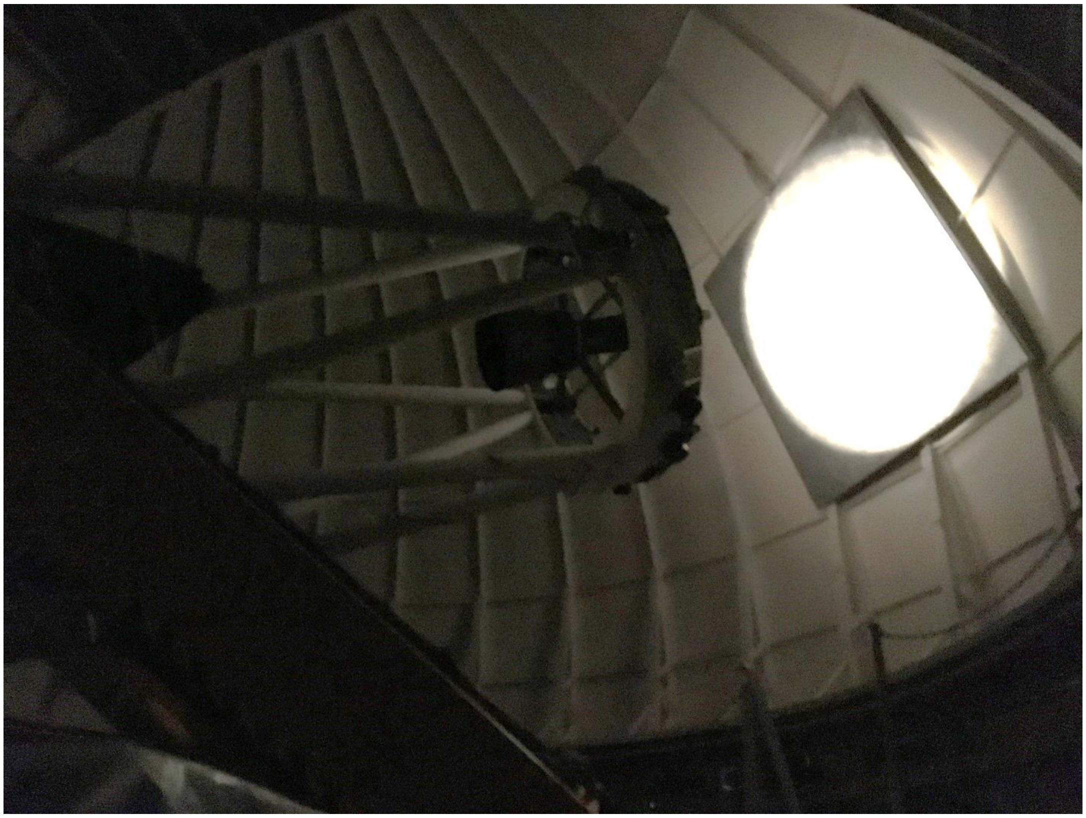

Figure 69. Taking Observatory Calibration Images

An out-of-focus flat-fielding screen on the dome interior used to evenly illuminate the science detector. Flat-fields were taken with each telescope filter so that later pixel-to-pixel variations could be corrected when performing photometry.

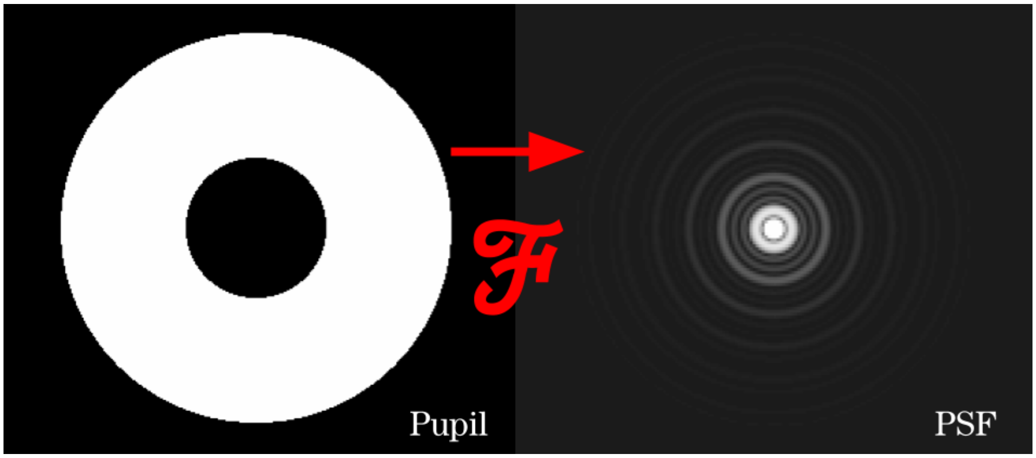

Figure 70. Fourier Transform of Telescope Pupil to Theoretical Airy Function

Transformation of the optical shape of the Kuiper 61” Cassegrain reflector into a perfect Airy PSF. The PSF was projected across an identical pixel plate scale as the HERESY detector in preparation for Strehl analysis.

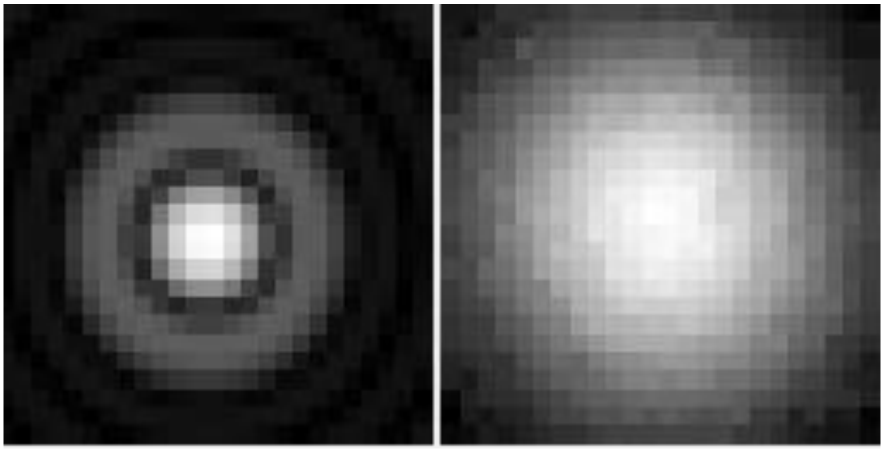

Figure 71. Ideal PSF and Star Science Target

Perfect Airy PSF compared to a seeing-limited star PSF imaged by HERESY. The perfect PSF peak pixel intensity was boosted to equal the centroided flux of the seeing-limited PSF. Finally, a Strehl ratio was calculated from the peak pixel intensity of the seeing-limited PSF divided by the peak pixel intensity of the perfect PSF.

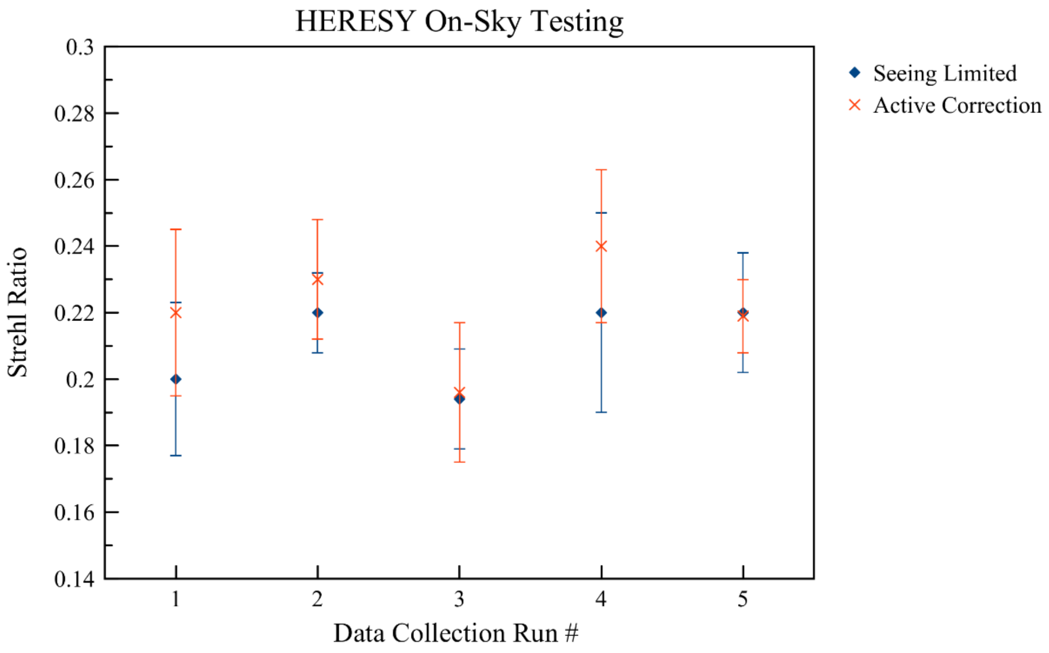

Figure 72. HERESY On-Sky Testing Results

This plot shows the differences between HERESY control images (seeing-limited, no correction) and with active correction with the hexapod. There was only a maximum improvement of ~3% in Strehl ratio from image-to-image, but improvement with active correction on was consistent. Error bars come from the photometry data reduction process such ass flat fielding, read noise subtraction, sky background subtraction, flux measurement, etc.

5 CONCLUSION

5.1 Research Objectives

5.1.1 HERESY Balloon Implementation

The goal of HERESY's balloon implementation was to develop a focal plane that was responsive and agile enough to eliminate gondola jitter pointing error. Its objectives were to cryogenically cool a focal plane, receive an error signal and perform corrective movements with at least a 60 Hz frequency (Nyquist sampling of the STO jitter), and eliminate all <20 micron. Through lab verification, it was shown that degradation to the PSF across pixels was minimized by hexapod actuation to within a residual plate scale blur of ~2 pixels. Therefore, this indicates HERESY would be successful at eliminating jitter aboard an STO-like balloon gondola that could achieve 1" sustained pointing.

5.1.2 CHESS Detector Payload

The CHESS detector payload was an effort to receive a FUV-optimized CCD from JPL and electrically and mechanically package it for a sounding rocket flight. On top of implementing a detector payload that could survive the rigors of launch, the rocket integration and science team, CU—Boulder, had a hard requirement that the CCD demonstrated QE of >30% across the FUV bandpass (100-160nm) to enable data collection of their echelle spectrograph over the short data collection period of the flight (~15 minutes).

The CCD was received and characterized at ASU demonstrating a standard 1-r silicon QE curve from 300-1200nm (no FUV equipment was accessible at ASU to measure UV response). The grounding scheme of the CCD electronics was optimized to control the detector noise own to 15e$^-$, and an AR-coated version of the flight CCD was on-sky characterized at the Kuiper 61" observatory, which helped with the payload development. The mechanical payload was then built up and final modifications made for flight, and finally the detector was integrated into the flight payload and tested successfully.

Code was written to facilitate communication between the rocket computer and the CCD controller, and an Interface Control Document was produced for CU—Boulder for safe integration onto their vehicle. Finally, the completed detector payload successfully survived rigorous component-level vibration testing at Orbital ATK's Phoenix facility and a vacuum chamber test at ASU to make sure the payload electronics could survive the space-environment for the duration of the flight.

Unfortunately, while this project met the long list of objectives for delivery to CU—Boulder, testing of the CCD FUV response showed numbers that were an order of magnitude lower than needed to produce the required SNR for flight (QE = 3% vs. 30%). While the payload was carefully handled, cleaned, and baked at ASU before delivery, the root cause of this issue was thought to be an unused threaded screw hole inside the payload that had a small amount of machine grease inside of it. This grease in turn coated itself onto the surface of the cold CCD pixel area which did not affect its QE performance across the visible range, but devastated QE across the FUV.

5.1.3 HERESY Observatory Implementation

HERESY's focal plane from its original balloon design was also modified to repurpose it for ground-based observatory use. A fast-read CMOS was co-mounted with the existing CCD to act as a star tracker with the idea of using bright natural guidestars to produce an error signal from tracking the centroid of their PSF as their light passes through the atmosphere. A nonlinear least-squares fit approach was used through the implementation of a Levenberg-Marquardt centroid-tracking algorithm in C++. Each successive frame from the CMOS was then used to produce a delta-position across the focal plane that was communicated to the hexapod for corrective motion.

In the lab, the developed algorithm was shown to be able to track the centroid of a light source mounted to X-Y stages. However, the proper lab equipment to fully simulate signal error due to atmospheric turbulence was lacking, so the mountain became the 'laboratory.' After successfully integrating HERESY onto the Kuiper 61" telescope, the instrument showed great promise as a prototype engineering unit. A Strehl analysis of before and after on-sky corrections showed minimal image improvements of target star PSFs. However, the limitations of HERESY's observatory implementation are now well known with a path forward to improve its design in the future.

5.2 Recommendations

5.2.1 HERESY Balloon Implementation

Using the systems engineering process, the HERESY concept was developed, and NASA funding was secured to purchase the instrumentation. The project was split into a phased approach, requirements were made for each phase, and PDR and CDRs along with trade studies were held before finalizing instrument purchases. While the detector, CCD, and cryostat – the main instrument – proved to all be effective, the validation equipment acquired was plagued with issues early in the project.

An important lesson was learned that even though the instrument specifications claimed a certain performance, certain uses of these instruments caused them to underperform. The first X-Y stages could not adequately recreate the STO jitter signal due to hysteresis when commanded to move through a series of micron-level motions, so these needed to be returned and improved stages (more costly) had to be procured. Also, despite the company claiming otherwise, the original PSM acquired could only output the laser's positional information at ~50 Hz. This did not fulfill a Nyquist sampling of the X-Y or hexapod stage movements (the desire was to sample at least three times movement frequency to preserve data quality), so the initial movement profile measurements suffered aliasing and clipping features.

In the future it would be wise to acquire instrumentation that can exceed the requirements by a safety factor rather than obtaining instruments that are believed to simply meet the requirements.

5.2.2 CHESS Focal Plane

One of the biggest challenges of this project was successfully wiring the JPL CCD electronics correctly and understanding the clocking scheme to ensure that charge could move from pixels to the readout amplifier on each quadrant of the detector. Since these devices are of an experimental nature and are far from being 'off-the-shelf', the documentation was essentially in rough draft form, and each detector used in the buildup of this project had its own bias voltage levels, and a slightly different clocking scheme, so it took a long period of time to optimize a detector.

While a lot was learned from getting the detector to work at LASI with the JPL team's help via email, it was very time consuming. Near the end of the project I ended up having to pay a visit to JPL anyway to work alongside the Advanced Detector team to make sure the flight CCD was operational and optimized. JPL also was able to provide supplemental code late in the game that ended up being essential for programming the interface between the detector payload and the sounding rocket computer. Therefore, in retrospect, there should have been a plan to work alongside JPL earlier in the project to make sure the CCD was up and running since it would have saved a lot of time.

Finally, the most important lesson learned from this project was that with the correct precautions, the contamination that ultimately killed the FUV sensitivity of the CCD may have been prevented. While many precautions were taken to protect this from happening, use low-outgassing materials, clean all mechanical components and bake them, and then hold everything under a guard vacuum after integration, the CCD still ended up being contaminated.

In hindsight, an additional step was needed to make sure the lab environment itself was a rated clean room – at least during the opening and closing of the cryostat, or when handling the CCD. In addition, if LASI had had the capability to perform FUV QE characterization, this issue may have been caught early enough for JPL to package a new uncontaminated detector, or to attempt to clean the contaminated one.

5.2.3 HERESY Observatory Implementation

This project was heavily time and budget constrained. Therefore, only one CMOS could be purchased and had a limited cost, which narrowed the selection. To improve the design, the following recommendations are: 1) Design and build a new structure to co-mount the CMOS with the CCD, 2) run the tracking code on a Linux machine to escape the limitations of Windows OS, 3) improve the thermal design for CCD cooling, 4) improve the lab test setup, 5) add more co-mounted CMOS trackers to the focal plane to increase the probability of locating a natural guidestar.

For 1), a custom fiberglass part was cut in the student machine shop for co-mounting the CMOS with the CCD, however, this design could have been much easier to integrate and help the thermal design if it was machined by a professional. 2) addresses the issue that atmospheric scintillation creates an error signal at a higher frequency than balloon jitter, so the effects of slow computer processing speeds were beginning to become a factor with the hexapod's ability to correct. The thermal design addressed in 3) is like 1) in that the flexible copper thermal strapping was cut out and implemented in the student shop and might have benefited from a professional building it. The thermal strapping worked well for the HERESY balloon implementation, but with the addition of the CMOS into the focal plane, more heat was dissipated, resulting in higher CCD operating temperatures. 4) points out that a test setup was not in place in the lab to properly model atmospheric turbulence type image fluctuations, so the code was only vetted on a light source moving on X-Y stages. Finally, 5) is an acknowledgement that it was very difficult to line up both a bright star in the CMOS FOV and a target in the CCD FOV simultaneously, therefore, more CMOS would increase odds of success. In a future iteration, rather than increasing the amount of CMOS, a laser guidestar setup that it brought to the telescope with HERESY might be considered to mitigate this issue.

5.2.4 HERESY Thermal Redesign

After a discussion with my graduate committee, a thermal system design improvement was developed for use with the HERESY cryostat. Although the original system was modeled to cool the science CCD on the hexapod down to -123 °C, in practice, the custom thermal straps were only able to cool the CCD to -70 °C. The likely root cause of this discrepancy is due to poor thermal conductive contact between the copper strap surfaces between the CCD interface and the liquid nitrogen cooled plate. Even without improving the design of how the thermal straps contact cooling surfaces, one solution is to simply increase the number of thermal straps from the cold plate to the CCD, thereby increasing the cooling capacity of the system. However, the issue with this approach is that it increases the complexity of the design and the risk that some of the flexible straps could contact cryostat or hexapod surfaces thereby creating a 'thermal short' and risking damaging components.

A best-of-all-worlds solution would involve building a rigid ¼" thick copper structure that matches the circular area of the liquid nitrogen cold plate that also has a matching cold plate hole pattern (~twenty 4-40 tapped holes) to provide solid and even conductive contact with the cold structure. This copper cold structure would then have four rigid 1" diameter copper posts that screw onto the cold plate copper structure that rise along the sides of the hexapod to a height of 8.5" to be level with the top of the CCD focal plane copper structure. This rigid design will replace the need for flexible copper straps to rise nearly a foot from the cold plate to the top of the hexapod which introduced the risk of a thermal short within the cryostat.

Finally, to complete the thermal link, high-quality custom clamped flexible copper thermal braiding would be attached between the copper posts to the CCD focal plane. This design can be procured inexpensively OTS from several companies to ensure the high quality and proper manufacturing of the material (www.techapps.com/copper-thermal-strap-assemblies is a great example). Between the posts, the flexible copper straps, and the CCD copper interface, thin indium sheets are used that have a high thermal conductivity and when squeezed between surfaces are soft enough to flatten and fill in any remaining air gaps to provide the best thermal interfacing possible.

In this design, the copper posts would stand approximately 120mm away from the edge of the hexapod in its zero position. Since the hexapod's XY throw is 17mm, there is no risk of the hexapod inadvertently impacting the new copper structure.

5.3 Future Work

The next iteration of HERESY has a bright future in both its balloon and ground-based implementation. Beyond the improvements that were discussed in the recommendations section above, funding should be sought to continue the development of HERESY for an actual balloon mission. Now that its prototype version has been verified a mission is justified.

One issue with HERESY is that it relies upon an existing pointing gondola, so perhaps a pointing structure like WASP could be developed specific to HERESY and could be offered as a complete unit to simply be hooked on to a balloon for flight. This is a type of ready-to-go payload that NASA's Flight Opportunities Program would likely fund for a maiden flight and then potentially a long-duration Antarctic flight after that.

For HERESY's observatory implementation, further testing could benefit from a telescope to be acquired for use at ASU, so that HERESY can continue to improve its star tracker technology. For a setup such as this, HERESY might need to be attached to the back of the telescope structure, so ways could be explored to produce a ‘mini’ version of HERESY. This mini version could be produced by removing the large liquid nitrogen tank, that makes up about half of the cryostat, thereby drastically reducing mass. In the liquid nitrogen tanks place, a compact thermoelectric cooling system could be installed for CCD temperature control. The instrument also could be designed to have a constant nitrogen gas flow, so that it would only need to live in a housing rather than require to be under vacuum.

5.4 Self-Reflections

After looking back on seven years of graduate school it is tempting to have the mindset of “if I only knew then what I know now.” Almost all aspects of my general knowledge and experimental design ability have greatly improved, so if I could go back in time, I could carry out my research projects quicker and more effectively. Of course, in the end, this type of training and growth *is* the overall purpose of graduate school, so in that regards, my time was well spent.

Over the course of my studies I have grown as a researcher by publishing manuscripts and presenting my research at several conferences (SPIE, AAS, APS and NSRC). I also had the opportunity to work at JPL during my first two summers, which involved conducting hands on work with advanced CCD characterization in the Micro-Devices Laboratory. My time spent at JPL was essential to my growth as a lab worker, as it taught me proper lab practices, techniques for cleaning and operating cryogenic systems, and how to safely interact with extremely ESD-sensitive detectors.

Working in the LASI helped me to develop and hone several abilities that will be very useful in my career, but maybe none more important than becoming an effective programmer. I had very minimal programming knowledge coming into this program, but over the years I now can interpret and write comfortably in LabView, MATLAB, Python, C++, IDL, and assembly code. This has been essential as I have had to set up lab automation for data collection, write code to operate the hexapod and X-Y stages, perform image processing, and edit CCD readout parameters. I also had to write a Python interface for to enable an ethernet communication protocol between the detector payload and the sounding rocket flight computer for the CHESS program.

In addition to my main research projects, I also had the opportunity to fill the role of camera lead on a conceptual cubesat project known as the Space Weather and Meteor Impact Monitoring Satellite, or SWIMSat, funded by the Navy's University Nanosat Program (UNP). This 6U cubesat would live in a Geosynchronous Transfer Orbit and have two imagers, one a coronagraph to detect solar flares or coronal mass ejections from the Sun, and the other an optical camera that repeatedly images the disc of the Earth to detect bolides (for instance, the Chelyabinsk event would have been a prime detection candidate).

From this SWIMSat I learned a wealth of practical knowledge about systems engineering process through the development of mission Concept of Operations and formulating conceptual instrumentation that conformed to our vehicle's size, weight, and power (SWaP) requirements. As a team we presented SWIMSat at the Small-Sat Conference, where we conducted a PDR before a panel of Navy engineers and other university teams.

At the time of writing this dissertation, I currently am employed in a job in the aerospace industry, and the skills learned over the years during my tenure as a graduate student have been essential for succeeding in my current position.

WORKS CITED

Albert, J., G. Aldering, S. Allam, W. Althouse, R. Amanullah, J. Annis, P. Astier, M. Aumeunier, S. Bailey, C. Baltay, E. Barrelet, S. Basa, C. Bebek, L. Bergstom, G. Bernstein, M. Bester, B. Besuner, B. Bigelow, R. Blandford, R. Bohlin, and A. Bonissent. "Supernova Acceleration Probe: Studying Dark Energy with Type Ia Supernovae." *Department of Energy Contract* (2005)

Asay-Davis, Xylar S., Philip S. Marcus, Michael H. Wong, and Imke De Pater. "Jupiter's Shrinking Great Red Spot and Steady Oval BA: Velocity Measurements with the 'Advection Corrected Correlation Image Velocimetry' Automated Cloud-tracking Method." *Icarus*203, no. 1 (2009): 164-88. doi:10.1016/j.icarus.2009.05.001.

Asay-Davis, Xylar S., Philip S. Marcus, Michael H. Wong, and Imke De Pater. "Changes in Jupiter's Zonal Velocity between 1979 and 2008." *Icarus*211, no. 2 (2011): 1215-232. doi:10.1016/j.icarus.2010.11.018.

Barthol, P., A. Gandorfer, S. K. Solanki, M. Schüssler, B. Chares, W. Curdt, W. Deutsch, A. Feller, D. Germerott, B. Grauf, K. Heerlein, J. Hirzberger, M. Kolleck, R. Meller, R. Müller, T. L. Riethmüller, G. Tomasch, M. Knölker, B. W. Lites, G. Card, D. Elmore, J. Fox, A. Lecinski, P. Nelson, R. Summers, A. Watt, V. Martínez Pillet, J. A. Bonet, W. Schmidt, T. Berkefeld, A. M. Title, V. Domingo, J. L. Gasent Blesa, J. C. Del Toro Iniesta, A. López Jiménez, A. Álvarez-Herrero, L. Sabau-Graziati, C. Widani, P. Haberler, K. Härtel, D. Kampf, T. Levin, I. Pérez Grande, A. Sanz-Andrés, and E. Schmidt. "The Sunrise Mission." *Solar Physics*268, no. 1 (2010): 1-34. doi:10.1007/s11207-010-9662-9.

Beasley, Matthew. "The Colorado High-Resolution Echelle Stellar Spectrograph (CHESS) Design and Status." *Physics Procedia 37* (2012): 1435-444. doi:10.1016/j.phpro.2012.03.746.

Bebek, C. 2006, *SNAP Imager CCD Technical Manual*, Lawrence Berkeley National Laboratory, 1 Cyclotron Road Berkeley, CA 94720

Bernasconi, Pietro. *STO Mission Highlights and GUSSTO Mission Concept*. 2011. JHU/APL Presentation.

Blacksberg, J., S. Nikzad, M.E Hoenk, S.E Holland, and W.F Kolbe. "Near-100% Quantum Efficiency of Delta Doped Large-Format UV-NIR Silicon Imagers." *IEEE Transactions on Electron Devices* 55, no. 12 (2008): 3402-406.

Burke, Barry E., John Tonry, Michael Cooper, Gerard Luppino, George Jacoby, Richard Bredthauer, Kasey Boggs, Michael Lesser, Peter Onaka, Douglas Young, Peter Doherty, and David Craig. "The Orthogonal-transfer Array: A New CCD Architecture for Astronomy." *Optical and Infrared Detectors for Astronomy*, 2004. doi:10.1117/12.562490.

Chernov, N., and C. Lesort. "Least Squares Fitting of Circles." Journal of Mathematical Imaging and Vision 23, no. 3 (2005): 239-52.

Dankanich, J.W., Kremic, T., Hibbits, K., Young, E.F., Landis, R., "Planetary Balloon-Based Science Platform Evaluation and Program Implementation," *NASA/TM –2016-218870, Final Report*, 2016.

Diller, Jed, Kevin Dinkel, Zach Dischner, and Eliot Young. "Design and Performance of the BOPPS UVVis Fine Pointing System." *2015 IEEE Aerospace Conference*, 2015. doi:10.1109/aero.2015.7119125.

Dunbar, Brian. "Technology Readiness Level." NASA. October 28, 2012. https://www.nasa.gov/directorates/heo/scan/engineering/technology/txt_accordion1.html.

Fitzpatrick, Patrick J., Imke De Pater, Statia Luszcz-Cook, Michael H. Wong, and Heidi B. Hammel. "Dispersion in Neptune's Zonal Wind Velocities from NIR Keck AO Observations in July 2009." *Astrophysics and Space Science*350, no. 1 (2013): 65-88. doi:10.1007/s10509-013-1737-2.

France, Kevin, Matthew Beasley, Robert Kane, Nicholas Nell, Eric B. Burgh, and James C. Green. "Development of the Colorado High-resolution Echelle Stellar Spectrograph (CHESS)." *Space Telescopes and Instrumentation 2012: Ultraviolet to Gamma Ray* (2012).

France, Kevin, Keri Hoadley, Brian T. Fleming, Robert Kane, Nicholas Nell, Matthew Beasley, and James C. Green. "The SLICE, CHESS, and SISTINE Ultraviolet Spectrographs: Rocket-Borne Instrumentation Supporting Future Astrophysics Missions." *Journal of Astronomical Instrumentation*05, no. 01 (2016): 1640001. doi:10.1142/s2251171716400018.

Frisch, Priscilla C., Seth Redfield, and Jonathan D. Slavin. "The Interstellar Medium Surrounding the Sun." *Annual Review of Astronomy and Astrophysics*49, no. 1 (2011): 237-79. doi:10.1146/annurev-astro-081710-102613.

Gavin, Henri P.. "The Levenberg-Marquardt method for nonlinear least squares curve-fitting problems." Duke Univ. Press, 2013.

Gierasch, P. J., A. P. Ingersoll, D. Banfield, S. P. Ewald, P. Helfenstein, A. Simon-Miller, A. Vasavada, H. H. Breneman, D. A. Senske, and Galileo Imaging Team. "Observation of Moist Convection in Jupiters Atmosphere." *Nature*403, no. 6770 (2000): 628-30. doi:10.1038/35001017.

Green, Martin A., and Mark J. Keevers. "Optical Properties of Intrinsic Silicon at 300 K." *Progress in Photovoltaics: Research and Applications*3, no. 3 (1995): 189-92. doi:10.1002/pip.4670030303.

Groppi, Chris. *Private Conversation*. 2013.

H-811 Vacuum-Compatible Miniature Hexapod 6-Axis Positioner. 2013. Manual Physik Instrumente

Hibbitts, C. A., E. Young, T. Kremic, and R. Landis. "Science Measurements and Instruments for a Planetary Science Stratospheric Balloon Platform." *2013 IEEE Aerospace Conference*, 2013. doi:10.1109/aero.2013.6497132.

Hoadley, Keri. "Experimental and Observational Studies of Molecular Hydrogen in Interstellar and Circumstellar Environments." ProQuest Dissertations Publishing, 2017.

Hoenk, Michael E, Grunthaner; Paula J, Grunthaner; Frank J, Terhune; Robert W, and Hecht; Michael H. "Growth of delta-doped layers on silicon CCD/S for enhanced ultraviolet response." *US Patent*. 1994.

Howell, Steve B. *Handbook of CCD Astronomy*. Cambridge: Cambridge University Press, 2006.

IRLabs. 2004, "Infrared Laboratories ND-5 Series User Manual." Infrared Laboratories, 1808 East 17th St Tucson, AZ 85719-6505 USA

Janesick, James R. 2001. *Scientific Charge-coupled Devices*. Bellingham, WA: SPIE.

Kane, Robert, Matthew Beasley, James Green, Eric Burgh, and Kevin France. "The Opto-mechanical Design of the Colorado High-resolution Echelle Stellar Spectrograph (CHESS)." *UV, X-Ray, and Gamma-Ray Space Instrumentation for Astronomy XVII*, 2011. doi:10.1117/12.892825.

Kitchin, Christopher Robert. *Astrophysical Techniques*. Boca Raton: CRC Press, 2014.

Kraut, Alan, Kevin Swartzlander, Elton Wong, Graham Orr, Tony Wimer, Yusuke Nakaya, Mark Bullock, Eliot Young, and Patrick Little. "Sub-arcsecond Pointing for Balloon-borne Telescopes." *Ground-based and Airborne Telescopes II*, 2008. doi:10.1117/12.789138.

Kremic, T., K. Hibbitts, E. Young, R. Landis, K. Noll, and K. Baines. "Assessing the Potential of Stratospheric Balloons for Planetary Science." *2013 IEEE Aerospace Conference*, 2013. doi:10.1109/aero.2013.6496843.

Landsman, W. B., "DAOPHOT IDL Library." *Astronomical Data Analysis Software and Systems II, A.S.P. Conference Series, Vol. 52, ed., p. 246,* 1993.

Leach, Robert. "Astronomical Research Cameras, Inc." Http://www.astro-cam.com/. Accessed August 28, 2012. http://www.astro-cam.com/.

Legarreta, J., and A. Sanchezlavega. "Vertical Structure of Jupiters Troposphere from Nonlinear Simulations of Long-lived Vortices." *Icarus*196, no. 1 (2008): 184-201. doi:10.1016/j.icarus.2008.02.018.

Lewis C. Roberts, Marshall D. Perrin, Franck Marchis, Anand Sivaramakrishnan, Russell B. Makidon, Julian C. Christou, Bruce A. Macintosh, Lisa A. Poyneer, Marcos A. van Dam, Mitchell Troy, "Is that really your Strehl ratio?," Proc. SPIE 5490, Advancements in Adaptive Optics, 2004.

Miller, Alexander D., Tom Pirrone, Iain Beveridge, and Andrew Antonio. "World View Enterprises Altitude Controlled Balloons: A New Stratospheric Platform for Persistent Earth and Space Imaging Campaigns." *Ground-based and Airborne Telescopes VII*, 2018. doi:10.1117/12.2313446.

Milliard, Bruno, D. Christopher Martin, David Schiminovich, Jean Evrard, Matt Matuszewski, Shahinur Rahman, Sarah Tuttle, Ryan Mclean, Jean-Michel Deharveng, Frederi Mirc, Robert Grange, and Robert Chave. "FIREBALL: The Faint Intergalactic Medium Redshifted Emission Balloon: Overview and First Science Flight Results." *Space Telescopes and Instrumentation 2010: Ultraviolet to Gamma Ray*, 2010. doi:10.1117/12.857850.

NSROC. 2001, "Sounding Rocket Program Handbook." Wallops Flight Facility, Virginia.

"PC/104 Modules, PC/104 Systems, SBCs, Enclosures: RTD." PC/104 Stackable ISA, PCI & PCI Express SBCs and Rugged Embedded System. Accessed February 25, 2013. https://www.rtd.com/.

Rhodes, Jason, Benjamin Dobke, Jeffrey Booth, Richard Massey, Kurt Liewer, Roger Smith, Adam Amara, Jack Aldrich, Joel Berge, Naidu Bezawada, Paul Brugarolas, Paul Clark, Cornelis M. Dubbeldam, Richard Ellis, Carlos Frenk, Angus Gallie, Alan Heavens, David Henry, Eric Jullo, Thomas Kitching, James Lanzi, Simon Lilly, David Lunney, Satoshi Miyazaki, David Morris, Christopher Paine, John Peacock, Sergio Pellegrino, Roger Pittock, Peter Pool, Alexandre Refregier, Michael Seiffert, Ray Sharples, Alexandra Smith, David Stuchlik, Andy Taylor, Harry Teplitz, R. Ali Vanderveld, and James Wu. "Space-quality Data from Balloon-borne Telescopes: The High Altitude Lensing Observatory (HALO)." *Astroparticle Physics*38 (2012): 31-40. doi:10.1016/j.astropartphys.2012.05.015.

Press, William H., and William T. Vetterling. *Numerical Recipes*. Cambridge: Cambridge Univ. Press, 2007.

Redfield, Seth, and Jeffrey L. Linsky. "The Three-dimensional Structure of the Warm Local Interstellar Medium. II. The Colorado Model of the Local Interstellar Cloud." *The Astrophysical Journal*534, no. 2 (2000): 825-37. doi:10.1086/308769.

Roberts, Jr. Lewis C., and Christopher R. Neyman. "Characterization of the AEOS Adaptive Optics System." *Publications of the Astronomical Society of the Pacific*114, no. 801 (2002): 1260-266. doi:10.1086/343221.

Robinson, M.S., Lunar Reconnaissance Orbiter Camera Experimental Data Record, LRO-L-LROC-2-EDR-V1.0, NASA Planetary Data System, 2010.

Sayanagi, Kunio M., Ulyana A. Dyudina, Shawn P. Ewald, Georg Fischer, Andrew P. Ingersoll, William S. Kurth, Gabriel D. Muro, Carolyn C. Porco, and Robert A. West. "Dynamics of Saturn's Great Storm of 2010–2011 from Cassini ISS and RPWS." *Icarus*223, no. 1 (2013): 460-78. doi:10.1016/j.icarus.2012.12.013.

"Scientific Grade or Industrial Cameras with CCD, CMOS or SCMOS That Utilize USB, PCIe, or Thunderbolt Connections." XIMEA. Accessed May 23, 2015. https://www.ximea.com/.

Scowen, Paul A. "The High Resolution Time Domain Explorer (HiTiDE): A High-Resolution Suborbital Telescope for Time Domain Imaging of Outer Planets." NASA Proposal NNH14ZDA001N-SSO, 2014.

Stuchlik, David. "The NASA Wallops Arc-Second Pointer (WASP) System for Precision Pointing of Scientific Balloon Instruments and Telescopes." *AIAA Balloon Systems Conference, AIAA AVIATION Forum, (AIAA 2017-3609)*, 2017.

"Teledyne E2v High Performance RF Power, Semiconductor and Imaging Technologies." https://www.teledyne-e2v.com/.

Tian, Jing, Wenshu Yang, Zhenming Peng, and Tao Tang. "Inertial Sensor-based Multiloop Control of Fast Steering Mirror for Line of Sight Stabilization." *Optical Engineering* 55, no. 11 (2016): 111602. doi:10.1117/1.oe.55.11.111602.

Veach, Todd J., and Paul A. Scowen. "Innovative CCD Readout Technology for Use in Large Focal Plane Array Development." UV/Optical/IR Space Telescopes and Instruments: *Innovative Technologies and Concepts VI*, 2013. doi:10.1117/12.2024118.

Veach, Todd J. 2013, "Investigation of Star Formation: Instrumentation and Methodology." PhD Thesis. Arizona State University

Veach, Todd J., Paul A. Scowen, Matthew Beasley, and Shouleh Nikzad. "Modified Modular Imaging System Designed for a Sounding Rocket Experiment." *Ground-based and Airborne Instrumentation for Astronomy IV*, 2012. doi:10.1117/12.925592.

"Vision and Voyages for Planetary Science in the Decade 2013-2022." 2011. doi:10.17226/13117.

Walker, C., C. Kulesa, P. Bernasconi, H. Eaton, N. Rolander, C. Groppi, J. Kloosterman, T. Cottam, D. Lesser, C. Martin, A. Stark, D. Neufeld, C. Lisse, D. Hollenbach, J. Kawamura, P. Goldsmith, W. Langer, H. Yorke, J. Sterne, A. Skalare, I. Mehdi, S. Weinreb, J. Kooi, J. Stutzki, U. Graf, M. Brasse, C. Honingh, R. Simon, M. Akyilmaz, P. Puetz, and Mark Wolfire. "The Stratospheric THz Observatory (STO)." *Ground-based and Airborne Telescopes III*, 2010. doi:10.1117/12.857765.

Wizinowich, Peter. "Adaptive Optics And Interferometry: Present And Future Systems And The Impact Of Turbulence." *Optical Turbulence*, 2009. doi:10.1142/9781848164864_0032.